



RESEARCH ARTICLE

10.1029/2019MS001766

Special Section:

The Energy Exascale Earth System Model (E3SM)

Key Points:

- Introduces the U.S. DOE's Energy Exascale Earth System Model-Biogeochemistry version, E3SMv1.1-BGC, is introduced
- Ecosystem-climate responses are characterized in a standard set of C4MIP-type simulations
- The impacts of terrestrial nitrogen and phosphorus limitations and their structural uncertainties are explored

Supporting Information:

- Supporting Information S1

Correspondence to:

S. M. Burrows,
susannah.burrows@pnnl.gov

Citation:

Burrows, S. M., Maltrud, M., Yang, X., Zhu, Q., Jeffery, N., Shi, X., et al. (2020). The DOE E3SM v1.1 biogeochemistry configuration: Description and simulated ecosystem-climate responses to historical changes in forcing. *Journal of Advances in Modeling Earth Systems*, 12, e2019MS001766. <https://doi.org/10.1029/2019MS001766>

Received 10 JUN 2019

Accepted 20 AUG 2020

Accepted article online 28 AUG 2020

©2020. The Authors.

This is an open access article under the terms of the Creative Commons Attribution-NonCommercial License, which permits use, distribution and reproduction in any medium, provided the original work is properly cited and is not used for commercial purposes.

The DOE E3SM v1.1 Biogeochemistry Configuration: Description and Simulated Ecosystem-Climate Responses to Historical Changes in Forcing

S. M. Burrows¹ , M. Maltrud², X. Yang³ , Q. Zhu⁴ , N. Jeffery², X. Shi³, D. Ricciuto³ , S. Wang² , G. Bisht¹ , J. Tang⁴ , J. Wolfe² , B. E. Harrop¹ , B. Singh¹ , L. Brent^{1,5} , S. Baldwin² , T. Zhou¹ , P. Cameron-Smith⁶ , N. Keen⁴, N. Collier³ , M. Xu³ , E. C. Hunke² , S. M. Elliott², A. K. Turner² , H. Li⁷, H. Wang¹ , J.-C. Golaz⁶ , B. Bond-Lamberty^{1,8} , F. M. Hoffman^{3,9} , W. J. Riley⁴ , P. E. Thornton³ , K. Calvin^{1,8} , and L. R. Leung¹ 

¹Pacific Northwest National Laboratory, Richland, WA, USA, ²Los Alamos National Laboratory, Los Alamos, NM, USA,

³Oak Ridge National Laboratory, Oak Ridge, TN, USA, ⁴Lawrence Berkeley National Laboratory, Berkeley, CA, USA,

⁵Now at Department of Atmospheric Sciences, Colorado State University, Fort Collins, CO, USA, ⁶Lawrence Livermore National Laboratory, Livermore, CA, USA, ⁷Department of Civil and Environmental Engineering, University of Houston, Houston, TX, USA, ⁸Pacific Northwest National Laboratory, College Park, MD, ⁹Department of Civil &

Environmental Engineering, University of Tennessee, Knoxville, TN, USA

Abstract This paper documents the biogeochemistry configuration of the Energy Exascale Earth System Model (E3SM), E3SMv1.1-BGC. The model simulates historical carbon cycle dynamics, including carbon losses predicted in response to land use and land cover change, and the responses of the carbon cycle to changes in climate. In addition, we introduce several innovations in the treatment of soil nutrient limitation mechanisms, including explicit dependence on phosphorus availability. The suite of simulations described here includes E3SM contributions to the Coupled Climate-Carbon Cycle Model Intercomparison Project and other projects, as well as simulations to explore the impacts of structural uncertainty in representations of nitrogen and phosphorus limitation. We describe the model spin-up and evaluation procedures, provide an overview of results from the simulation campaign, and highlight key features of the simulations. Cumulative warming over the twentieth century is similar to observations, with a midcentury cold bias offset by stronger warming in recent decades. Ocean biomass production and carbon uptake are underpredicted, likely due to biases in ocean transport leading to widespread anoxia and undersupply of nutrients to surface waters. The inclusion of nutrient limitations in the land biogeochemistry results in weaker carbon fertilization and carbon-climate feedbacks than exhibited by other Earth System Models that exclude those limitations. Finally, we compare with an alternative representation of terrestrial biogeochemistry, which differs in structure and in initialization of soil phosphorus. While both configurations agree well with observational benchmarks, they differ significantly in their distribution of carbon among different pools and in the strength of nutrient limitations.

Plain Language Summary A new state-of-the-art Earth System Model has been funded by the United States Department of Energy (DOE) to explore questions relevant to DOE's mission. The Energy Exascale Earth System Model version 1.1 (E3SMv1.1) represents nitrogen and phosphorous controls on the carbon cycle and extends the recently released E3SMv1 to include active biogeochemistry in the land, ocean, and ice components. E3SMv1.1 also includes an alternative representation of terrestrial carbon and nutrient cycles that is used to explore model structural uncertainties. E3SMv1.1's capabilities are demonstrated through a set of experiments described by the Coupled Climate-Carbon Cycle Model Intercomparison Project, aimed at understanding the influence of changes in climate and CO₂ on the carbon cycle. Simulations of the land surface properties and terrestrial carbon cycle compare well with observations, as does the simulated global and regional climate. Nutrient limitations result in less land carbon uptake compared to models that exclude these limitations. However, variations in model structure and initialization influence the magnitude of those limitations and carbon cycle dynamics. The ocean biogeochemistry in E3SMv1.1 simulates less biomass and slightly lower anthropogenic carbon uptake than

is observed. Future efforts will aim to reduce model biases as well as to include additional aspects of global carbon cycle dynamics.

1. Introduction

The Earth's natural and managed ecosystems play a critical role in controlling climate, primarily through their regulation of greenhouse gas concentrations. Atmospheric CO₂ concentrations have increased from 277 ppm around 1750 to 405 ppm in 2017 (Le Quéré et al., 2018), predominantly due to emissions from burning fossil fuels and land use change (Ciais et al., 2013). About one quarter of anthropogenic carbon emitted since 1750 (215 ± 50 PgC) has been stored in terrestrial ecosystems, that is, in vegetation and soils (Le Quéré et al., 2018).

The global ocean also plays a critical role in the carbon-climate system, having stored an estimated total of 165 ± 20 PgC of excess carbon—or about a quarter of anthropogenic CO₂ emissions—since 1750 (Le Quéré et al., 2018).

Despite decades of research, interactions between Earth's carbon cycle and climate remain among the largest uncertainties in predicting future climate response to a given magnitude of CO₂ emissions (Gregory et al., 2009). Improving understanding of ecosystem-climate interactions and their uncertainties has been identified as a critical challenge by the scientific community (Ciais et al., 2013; Tang & Riley, 2018; Thornton et al., 2017; Wuebbles et al., 2017).

The limitation of carbon uptake by nitrogen and phosphorus availability has recently been identified as a major source of uncertainty in the simulated response of Earth system models to CO₂ emissions (Ciais et al., 2013; Zaehle et al., 2014), including in the ELM model (Holm et al., 2020; Riley et al., 2018). Early work suggested, on the basis of ecosystem-level manipulation experiments (Melillo et al., 2002) and theory (Hungate et al., 2003), that nitrogen limitations could reduce the response of ecosystem growth and carbon uptake to increases in atmospheric CO₂ (progressive nutrient limitation hypothesis Luo et al., 2003). Studies have found that models that include nitrogen limitation simulate less carbon uptake in response to rising atmospheric CO₂ concentrations (Arora et al., 2019; Jain et al., 2009; Sokolov et al., 2008; Thornton et al., 2009). Evapotranspiration can also interact with ecosystem nutrient limitation effects (Beer et al., 2010; Gaudio et al., 2015; Yang et al., 2016). Finally, land ecosystems response to disturbances interact with nutrient limitations to affect the land CO₂ sink (Thornton et al., 2002). However, the magnitude of the effect of nutrient limits on carbon uptake is poorly constrained in the literature.

It has been hypothesized that adding nutrient constraints would reduce the uncertainty in terrestrial carbon uptake (Thornton et al., 2009); however, this hypothesis has been difficult to test given all of the other differences across Earth System Models. The E3SM project was in the unusual position of bringing together, at the time of the project's initiation, two previously separate model development efforts: the Converging Trophic Cascade (CTC) and the Equilibrium Chemistry Approximation (ECA) (acronyms are summarized in Table 1). Both of these efforts aimed to build more complete representations of terrestrial carbon-nitrogen-phosphorus coupling but adopted very different approaches. We chose to exploit this unique opportunity to examine two different carbon-nitrogen-phosphorus implementations within an otherwise identical coupled Earth System Model. In doing so, we employ the approach of comparing multiple models with diverse structures to gain insights into some of the sources of structural uncertainty affecting the terrestrial carbon cycle within an Earth System model (Arora et al., 2013).

In this paper, we describe the recently released biogeochemistry version of E3SM (denoted E3SMv1.1-BGC), which introduces several new developments in the treatment of land model biogeochemistry, which primarily focus on nutrient limitation mechanisms in vegetation and soils. Uncertainty in the representation of these mechanisms is addressed through comparison of the land ecosystem responses and carbon sink in historically forced simulations that employ two different representations of the soil and vegetation responses.

We note that considerably less attention is paid to the ocean biogeochemistry than to land biogeochemistry in this paper, despite the well-known importance of the ocean carbon sink. The E3SMv1.1 model, while inheriting many model components from its ancestor model, CESM1, replaced the ocean model component with an entirely new model of ocean physics, the MPAS-Ocean. Because of this major change, we anticipated

Table 1
Overview of Model Versions, Configurations, and Components

Acronym	Description
CTC	Converging Trophic Cascade (section 2.4.1)
ECA	Equilibrium Chemistry Approximation (section 2.4.2)
E3SMv1.0-DECK	E3SM model version and configuration documented by Golaz et al. (2019).
E3SMv1.1	E3SM model version 1.1, which differs from v1.0 through several bug fixes and minor improvements, as documented in the supporting information (Text S8).
E3SMv1.1-BGC	E3SM model version 1.1, in its default biogeochemistry configuration, which utilizes the CTC plant and soil carbon and nutrient mechanisms to represent carbon, nitrogen, and phosphorus limitation. This configuration also includes representation of coupled ocean and sea ice biogeochemistry.
E3SMv1.1-BGC-ECA	Same as E3SMv1.1-BGC, but utilizing the ECA plant and soil carbon and nutrient mechanisms in place of CTC. This configuration excludes coupled ocean and sea ice biogeochemistry.
EAM	land model component of the E3SMv1.1.
EAM	E3SM Atmosphere Model. The numbering of component models follows the numbering of the host model, that is, EAMv1.1 is the land model component of the E3SMv1.1.
ELM	E3SM Land Model. The ELMv1.1 is the land model component of the E3SMv1.1.
MPAS-Ocean	The Model for Prediction Across Scales - Ocean (MPAS-Ocean) is the ocean model component of E3SM.
MPAS-Seaice	The Model for Prediction Across Scales - Seaice (MPAS-Seaice) is the sea ice model component of E3SM.

challenges in achieving a credible ocean carbon sink in this first attempt. In this initial E3SM carbon cycle modeling effort, therefore, our primary aim in simulating the ocean and sea ice biogeochemistry was to assess any major biases and identify prioritized targets for improvement. For the same reason, we did not attempt a full spin-up of the deep ocean and did not attempt prognostic, emission-driven CO₂ simulations in this initial effort. As it represents a key development milestone in the E3SM's carbon cycle, we felt it important to document the major biases in ocean biogeochemistry behavior in this model version, and to discuss the model improvements that will be targeted in future development efforts. We do not recommend the use of the E3SMv1.1-BGC ocean biogeochemistry results for scientific purposes.

The structure of this paper follows from its primary goal: This paper serves as the overall introduction and documentation of the E3SMv1.1-BGC model and its biogeochemical features, as well as the response of its simulated carbon sinks to increasing CO₂, with a particular focus on structural and functional uncertainties in the land model's nutrient cycles. As such, we include a high-level description of the model's features (section 2); documentation of the spin-up procedures used (section 3); a comparison of the model's simulated climate and ecosystem variables with observations (section 4); and a discussion of ecosystem responses to increasing CO₂ coupled biogeochemically or radiatively, and uncertainties in those responses related to model structure and initialization (section 5). Section 6 describes the impacts of ecosystem responses on climate variables and quantifies the carbon-climate feedback parameters and their temporal evolution. Section 7 briefly outlines future development plans to add features and address model biases, and a summary and conclusions are presented in section 8.

We pay special attention to documenting technical details of the simulation in this paper. The E3SM project aims to ensure a high level of confidence and reproducibility for key simulations through provenance tracking and testing processes; in this spirit, we summarize code changes, spin-up procedures, and efforts taken to

ensure reproducibility herein. Several appendices and the online supporting information provide additional technical details and documentation. The DOE has also invested in development of community benchmarking tools for biogeochemistry processes through the ILAMB capability (Collier et al., 2018), which we make use of here for evaluation of simulation results.

Finally, while this paper serves as a general overview of the E3SMv1.1-BGC, several follow-on papers are planned that will describe specific aspects of E3SMv1.1-BGC simulations in greater detail and document additional simulations (e.g., model behavior under future socioeconomic scenarios; O'Neill et al., 2016).

2. Overview of the E3SMv1.1 and the Biogeochemistry Configuration

The E3SMv1.0 has been introduced and described by Golaz et al. (2019) and has been used to conduct the full suite of Diagnosis, Evaluation, and Characterization of Klima (DECK) experiments that comprise the core of the CMIP6 model intercomparison project (Eyring et al., 2016). For clarity, we subsequently refer to that version as E3SMv1.0-DECK. In this section, we document minor differences from the E3SMv1.0-DECK, and give a high-level description of the biogeochemical features of E3SMv1.1-BGC.

The E3SMv1.1-BGC differs from the E3SMv1.0-DECK primarily in that major features of the carbon cycle and related global biogeochemical processes are simulated interactively. In particular, E3SMv1.1-BGC uses a land model with multiple prognostic pools for carbon, nitrogen, and phosphorus in vegetation, litter, and soil organic matter (SOM), and also includes active plant phenology and nutrient controls on photosynthesis, while E3SMv1.0-DECK prescribes seasonal changes in leaf area index (LAI), based on a climatology of satellite observations or “satellite phenology” (Lawrence & Chase, 2007). In addition, the E3SMv1.1-BGC simulates active ocean biogeochemistry, derived from the Biogeochemical Elemental Cycling (BEC) model (Moore et al., 2001, 2004), but with several improvements including two-way coupling to a sea ice biogeochemistry scheme.

All simulations presented in this paper were conducted at the E3SM’s current “standard” resolution, which comprises a 1° atmosphere and land, 0.5° river model, and ocean and sea ice with mesh spacing varying between 60 km in the midlatitudes and 30 km at the equator and poles.

2.1. E3SM Land Model General Description and Overview

ELM is the land model component of the E3SM and has as its starting point for development the Community Land Model Version 4.5 (CLM4.5 Koven et al., 2013; Oleson et al., 2013). The model simulates land processes and their interactions with the near-surface atmosphere.

2.2. Surface Interactions With Radiation, Energy, and Aerosol in ELMv1.1

The ELM’s hydrology retains the same formulations as the CLM4.5, including soil hydrology following the Zeng and Decker (2009) scheme; representation of lakes following lake, ice, snow, and sediment simulator (LISSS) of Subin et al. (2012); and snow parameterizations following primarily (Anderson, 1976; Dai & Zeng, 1997; Jordan, 1991). The E3SMv1.1 configurations described here do not include an active glacier model.

The ELM’s treatment of surface interactions with radiation is largely inherited from CLM4.5; surface albedo is calculated following separate treatments for different land types (e.g., canopies, glaciers, lakes, wetlands, snow, and wet and moist bare soil). The dust mobilization scheme (Mahowald et al., 2006) accounts for the impacts of wind friction speed, vegetation cover, and soil moisture in determining dust mobilization, and is based on the Dust Entrainment and Deposition model of Zender et al. (2003).

Building on these representations inherited from CLM4.5, the E3SMv1.0-DECK introduced an improved integration of atmospheric aerosol representation and deposition to the surface with the treatment of light-absorbing particles (i.e., dust and black carbon) in snow/ice (Flanner et al., 2012; Liu et al., 2016), correction of a bug in the calculation of the snow grain size, and minor modifications of the rate of evaporation from pervious road, calculation of leaf stomatal conductance, and a modification to the handling of nighttime land albedo (Golaz et al., 2019).

The E3SMv1.1-BGC model additionally includes several fixes for model bugs discovered late in the development cycle of the E3SMv1.0-DECK configuration. The fixes in the land model’s physics include (1) correcting an energy imbalance in the land surface, (2) improving the numerical stability in the lake model surface energy budget, (3) preventing excessive snow compaction, and (4) ensuring conservation of water (Zhang et al., 2018). These bug fixes are described in more detail in the supporting information (Text S8).

Table 2
Overview and Definition of Key Acronyms and Terms Related to Coupled Nutrient Cycles in E3SMv1.1-BGC

Key Acronym/Term	Definition
NEE	Net ecosystem exchange, PgC. In this paper, to include the net effect of all land-atmosphere carbon fluxes, including the product pool, that is, GPP, autotrophic, and heterotrophic respiration, fires, harvest flux (land to wood products), and anthropogenic disturbance flux. We note that there is a small discrepancy with the definition of NEE commonly used by terrestrial ecologists (Chapin et al., 2006), which excludes harvested products. In contrast, ELMv1 assumes that harvested products decay in place and are released back to the atmosphere as CO ₂ , thus they are included in the NEE reported from ELM. NEE is positive for a net carbon source (into the atmosphere) and negative for a net carbon sink (into the land or ocean).
LULCC	Land use land cover change
TEC	Total ecosystem carbon, PgC
GPP	Gross primary productivity, PgC
SOC	Soil organic carbon, PgC
SON	Soil organic nitrogen, PgN
Soil mineral P	Total soil mineral P, equivalent to the sum of all mineral phosphorus in soils: solution P, labile P, secondary mineral P, and occluded P.
FPI _{N, CTC} , FPI _{N, ECA} , FPI _{P, CTC} , FPI _{P, ECA}	Fraction of potential immobilization (FPI), for nitrogen or phosphorus, and for CTC or ECA, respectively. See Appendix A1 for details.
FPG _N , FPG _P	Fraction of potential GPP, for nitrogen or phosphorus, respectively. See Appendix A1 for details.
$\beta_{\text{land}}, \beta_{\text{ocean}}$	Land and ocean carbon stock response to changing atmospheric CO ₂ , PgC ppm ⁻¹
$\gamma_{\text{land}}, \gamma_{\text{ocean}}$	Land and ocean carbon stock response to changing global mean near-surface air temperature, PgC K ⁻¹

2.3. Overview of Carbon, Nitrogen, and Phosphorus Cycles in E3SMv1.1-BGC

In this section, we summarize the flow of carbon, nitrogen, and phosphorus in the land, ocean, sea ice, and atmosphere components of the E3SMv1.1 model. As an aid to the reader, certain key acronyms and terminology related to the nutrient cycles are summarized in Table 2 together with the definitions used herein.

Schematic overviews of the carbon, nitrogen, and phosphorus cycles are shown in Figures 1–3, respectively. In these figures, pools are shown as boxes and fluxes are shown as arrows. Each of these figures shows the higher-level structure of the model here, in general displaying the C4MIP Tier-1 requested variables (Jones et al., 2016), which in many cases combine subpools or fluxes. For example, the fire flux shown in Figure 1 is the total flux associated with fires from both vegetation and litter pools.

Within the E3SMv1.1-BGC land, ocean and sea ice components, the carbon, nitrogen, and phosphorus cycles are interactively coupled to each other via the impacts of nutrient limitation on primary production (all components) and soil microbial activity (land component), as described in section 2. Nutrient exchange is partially coupled between ocean and sea ice; nutrient exchanges between ocean, atmosphere, and land components are prescribed. Nutrient fluxes that are either prescribed from input files (e.g., riverine inputs, Appendix C2), or are lost from the model (e.g., leaching from soils) are shown as dashed arrows in the overview figures.

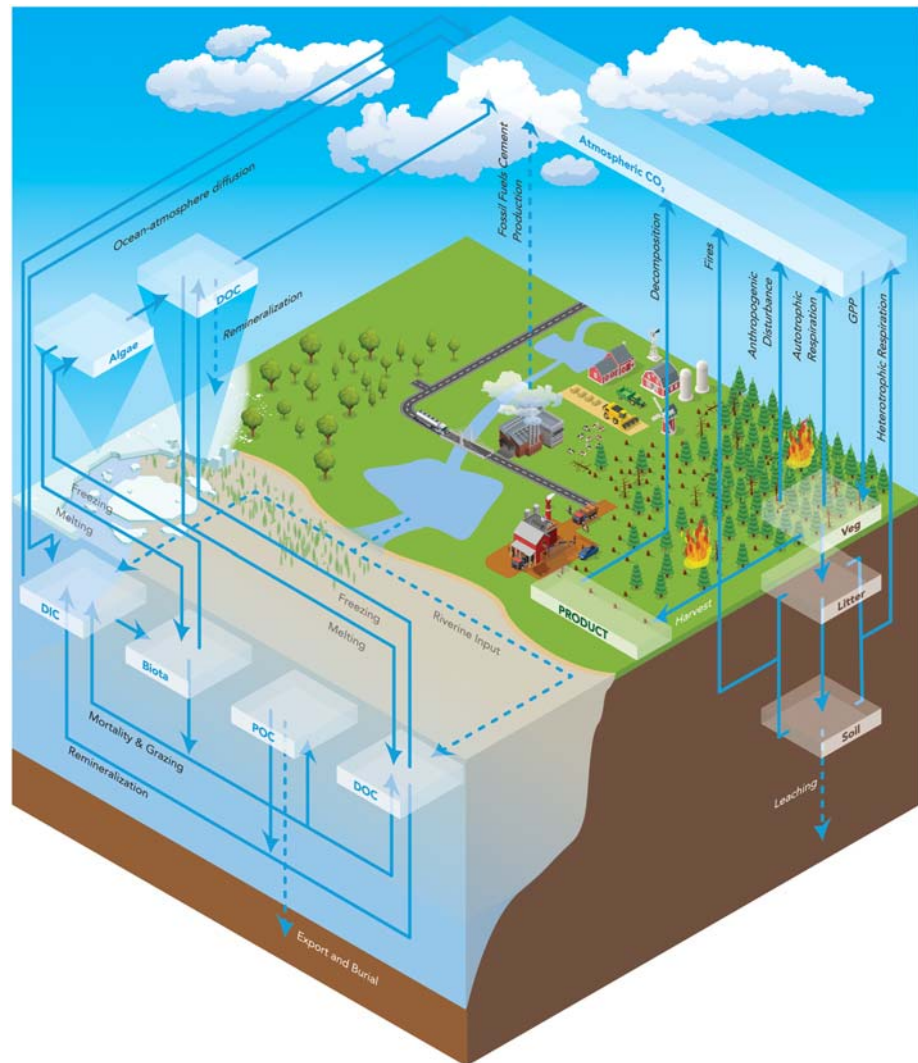


Figure 1. Global carbon cycle in the E3SMv1.1-BGC model, with major carbon pools (boxes) and fluxes (arrows). Dashed lines indicate fluxes that are either prescribed inputs to model carbon pools or losses which are not tracked further in the model.

2.3.1. Carbon Pools and Fluxes in Land, Ocean, and Sea Ice

The E3SMv1.1-BGC carbon pools and fluxes are shown in Figure 1.

The land carbon cycle includes vegetative growth, transfer of plant matter to litter pools via litterfall, and decomposition of litter into SOM. Human-driven land use and land cover change (LULCC) is prescribed; the combination of prescribed LULCC and modeled carbon stock determine the harvest, LULCC (e.g., deforestation), and anthropogenic disturbance fluxes. Vegetation carbon lost to harvest and LULCC is transferred to wood product pools, which subsequently loses carbon to the atmosphere through decomposition.

The net land-atmosphere exchange of carbon comprises the sum of (1) gross primary productivity (GPP), (2) autotrophic respiration, (3) heterotrophic respiration, (4) anthropogenic disturbance, and (5) fire losses from vegetation and litter. In this paper, we define the net ecosystem exchange (NEE) as equivalent to this net flux. This is the definition of NEE that has commonly been used in the Earth System Modeling community including past publications describing the CESM, of which this model is a descendent.

However, we note that this differs from the definition commonly used by terrestrial ecologists. Chapin et al. (2006) defines NEE as “net ecosystem exchange (the net CO₂ flux from the ecosystem to the atmosphere (or net CO₂ uptake [positive sign])). This definition specifically excludes gaseous carbon exchanges in the form of CO, CH₄, and VOC, which E3SMv1 does not treat. It also excludes net dissolved (lateral) inputs and losses

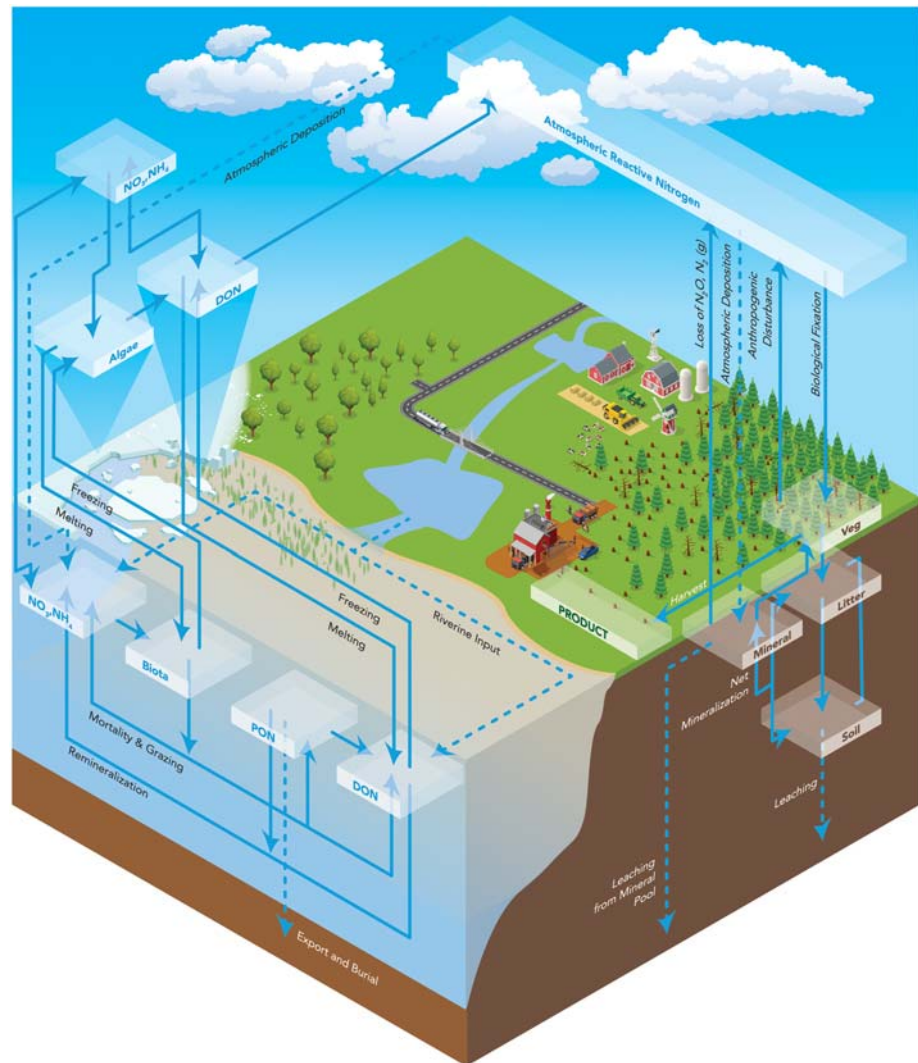


Figure 2. As in Figure 1, but for the E3SMv1.1-BGC global nitrogen cycle.

of DIC and DOC, and lateral transport of particulate carbon (including soot and harvest products); these terms are also not represented in ELMv1.

For harvested products, ELMv1 makes the simplifying assumption that all products decay in place on the harvest gridcell, releasing CO_2 back to the atmosphere from pools with life spans of 1, 10, and 100 years. This assumption has the consequence that the net land-atmosphere CO_2 exchange (i.e., NEE) reported for ELMv1 includes the carbon associated with the harvest and LULCC terms.

Additionally, we note that for fire losses, ELMv1 only accounts for CO_2 emissions, which are also included in the Chapin et al. (2006) definition of NEE. Fire emissions in the form of particulate transport or emissions of non- CO_2 gases are not calculated by ELMv1. Therefore, only CO_2 losses should be included when comparing the model's fire emissions with inventories.

We recognize that these model assumptions, particularly the treatment of harvest and LULCC terms, will produce discrepancies with the definitions used in bottom-up NEE budgets from terrestrial ecologists. However, we retain this usage for consistency with prior ESM publications, including those describing the CESM (the ancestor of E3SM). In the interest of clarity, we also call attention to this difference in Table 2.

The major carbon pools represented in the ocean are dissolved inorganic carbon (DIC), DOC, particulate organic carbon (POC), and marine biota. Carbon is added to the system via river inputs (Appendix C2), and removed due to burial in the deep ocean. In a novel development, E3SMv1.1 has introduced two-way

coupling of sea ice and ocean biogeochemistry: the ocean exchanges carbon with sea ice through freezing and melting of ice. In the sea ice, carbon is assumed to be available as required for algal growth, based on fixed carbon:nitrogen ratios, and this uptake of carbon is not tracked as a loss from other carbon pools. Losses from ice algal mortality and grazing are tracked in the sea ice DOC pool and passed to the ocean during melt for remineralization. As a consequence of this treatment, the sea ice biogeochemistry currently represents a net source of carbon in the E3SMv1.1-BGC model. Since this nonconservation is quite small (0.005–0.009 PgC/yr) relative to total global marine carbon budgets, it was judged acceptable for this initial implementation, but will be addressed in future model versions.

2.3.2. Nitrogen Pools and Fluxes in Land, Ocean, and Sea Ice

An overview of the E3SMv1.1 coupled nitrogen cycle is shown in Figure 2. Nitrogen is a limiting nutrient for both land and ocean biogeochemistry, and the model tracks the exchange of nitrogen in multiple forms (NO_3 , NH_4) throughout the global system.

The land nitrogen cycle includes representation of biological nitrogen fixation (from atmospheric N_2) and uptake by vegetation from the mineral pool (NH_4 and NO_3), the movement of nitrogen from vegetation through the litter pool to the soils, as well as net mineralization, which releases inorganic nitrogen from SOM into the mineral nitrogen pools. Atmospheric deposition are prescribed from files (Appendix C1); fertilizer inputs to agriculture are not represented in these simulations, because they do not include an active crop model. The model also simulates loss of nitrogen to the atmosphere as N_2O and N_2 (Koven et al., 2013), and loss of vegetation nitrogen due to anthropogenic disturbance. Vegetation removed through harvest results in a loss of vegetation nitrogen to the product pool. Leaching of nitrogen from the mineral pool on land is calculated as a diagnostic by the model, but is not yet linked to riverine biogeochemistry or ocean nitrogen inputs.

The ocean biogeochemistry represents transfer of nitrogen in its inorganic forms (NO_3 and NH_4), biota, particulate organic nitrogen and dissolved organic nitrogen (DON). Uptake of nitrogen by biota, as well as losses through mortality and zooplankton grazing, follow a fixed carbon:nitrogen ratio (Redfield ratio, 117:16). The ocean biogeochemistry also prescribes climatological atmospheric nitrogen deposition and river inputs (Appendix C2).

Coupling of the ocean and sea ice nitrogen cycles is a new feature in E3SMv1. Nitrogen is exchanged between ocean, sea ice NO_3 , NH_4 , and biota pools through sea ice melting and freezing. Additionally, sea ice DON, which is generated by mortality of sea ice biota, is returned to the ocean via melting of sea ice. In addition, ocean DON is transferred to the sea ice during freezing. However, as yet there is no implementation of sympagic remineralization for this source of organic nitrogen to allow utilization by ice algae.

2.3.3. Phosphorus Pools and Fluxes in Land, Ocean, and Sea Ice

An overview of the coupled phosphorus cycle is shown in Figure 3.

The addition of phosphorus limitation is a new feature in ELMv1.1 and detailed analyses of its impacts will be the subject of planned follow-on papers. The ELM tracks pools of phosphorus associated with vegetation biomass, litter, and SOM. The ELM also tracks three additional phosphorus pools in soils: solution P (and labile P), secondary mineral P, and occluded P. Carbon:phosphorus ratios in the ELM are predicted prognostically and are allowed to vary.

There are five soil mineral phosphorus pools:

- *Solution P*, which is the phosphorus that is dissolved in solution.
- *Labile P* represents phosphorus that is loosely adsorbed on soil particle surfaces and readily exchanges with soil solution phosphorus.
- *Secondary mineral P* represents phosphorus that is strongly sorbed onto soil minerals.
- *Occluded P*, which is unavailable to plants and microbes due to physical and chemical protection.
- *Parent material P* is phosphorus contained in bedrock.

Soil mineral P is the sum of these five pools.

Key processes by which phosphorus moves between pools include adsorption/desorption, immobilization, mineralization, phosphatase activity, and occlusion. Labile P can become more strongly adsorbed to soil particles and enter the secondary mineral P pool, and secondary mineral P in turn can desorb to return to the labile P pool. Secondary mineral P can be dissolved and enter labile P. Phosphorus can be biologically

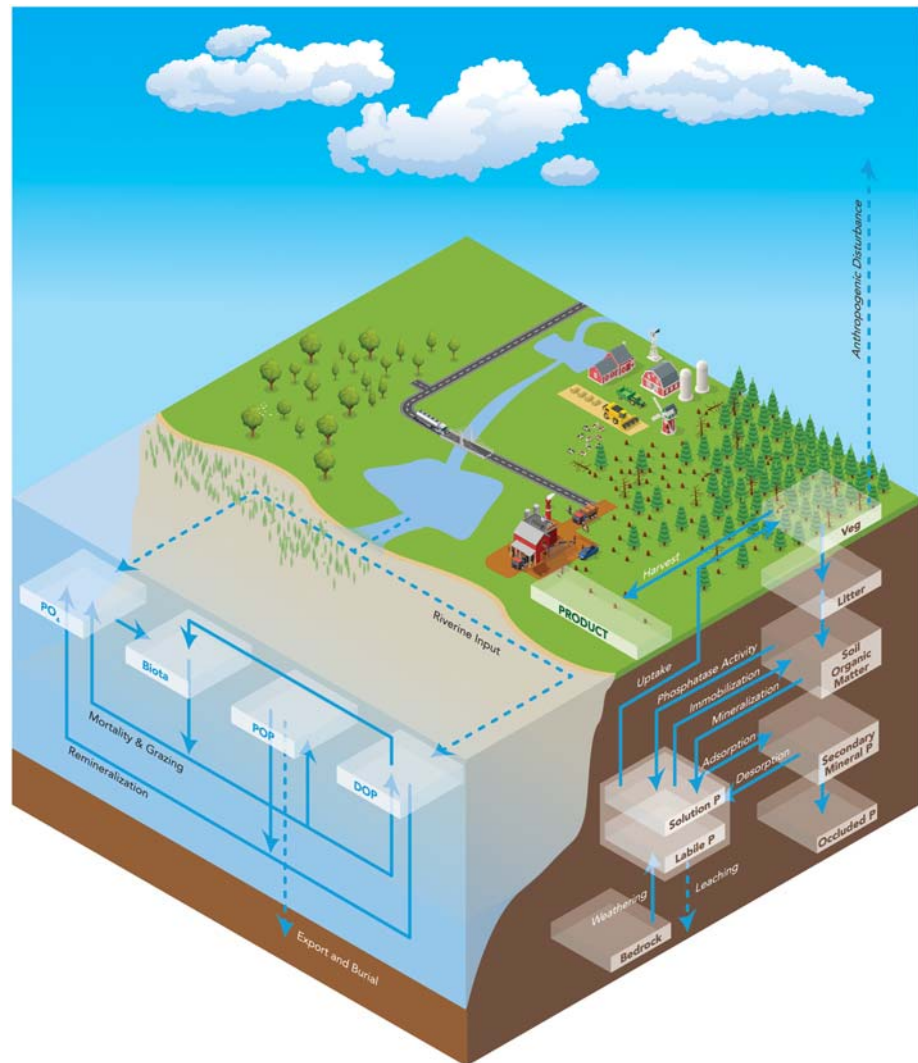


Figure 3. As in Figure 1, but for the E3SMv1.1-BGC global phosphorus cycle.

mineralized (through oxidation processes) or immobilized during decomposition of litter and SOM. Phosphatase activity releases inorganic phosphorus from SOM without carbon oxidation. Occlusion refers to the processes by which secondary mineral P becomes physically or chemically protected and is transferred to the occluded P pool.

Weathering of bedrock provides a continuous phosphorus source to soils on geological time scales. This source is prognostically simulated as the product of the abundance of mineral phosphorus in the parent material and a weathering rate (which is initialized from the parent phosphorus maps of Yang et al., 2013).

The phosphorus cycle is not fully closed in the ELMv1.1. Phosphorus losses from vegetation to atmosphere associated with fires (anthropogenic disturbance) and leaching of solution P into rivers are not tracked further in the model. Phosphorus from harvested vegetation enters the product pool and its evolution is not tracked further.

The ocean model tracks dissolved organic phosphorus, particulate organic phosphorus, and PO_4 . As with nitrogen, the phosphorus content of biota pools follows a fixed carbon:phosphorus ratio (117:1), except diazotrophs where the ratio is three times larger. As with carbon and nitrogen, riverine inputs of phosphorus to the ocean are prescribed and it is lost from the ocean through export and burial. There is no phosphorus cycle in the sea ice biogeochemistry.

2.4. E3SM Land Model Biogeochemistry Configurations

Structural uncertainties in the interactions of nutrient limitation, the land carbon sink, and climate were the primary focus of our initial development and simulation efforts in the E3SMv1.1-BGC model. We explore structural uncertainties by comparing simulations using two structurally different representations of soil biogeochemistry and nutrient effects on vegetation processes, the CTC and ECA approaches.

Both ELMv1.1-BGC and ELMv1.1-BGC-ECA share the same representations of many processes, including soil bulk oxygen content (Koven et al., 2015; Riley et al., 2011); soil radiocarbon dynamics (Chen et al., 2019; Koven et al., 2013); and aspects of the soil nitrogen cycle, for example, nitrification and denitrification (Koven et al., 2013).

Prognostic vegetation state fields in both configurations include biomass carbon, nitrogen, and phosphorus in leaves, fine roots, coarse roots, and multiple stem pools, LAI, stem area index, gradients of leaf morphology with vertical level in the canopy, and canopy height. Prognostic soil biogeochemistry variables include carbon, nitrogen, and phosphorus components for coarse woody debris, plant litter, and SOM, with litter and SOM pools resolved at multiple levels with depth in the soil column.

Vegetated surfaces are represented by up to 15 possible plant functional types (PFTs). The time-evolving fractional area of PFTs on the vegetated fraction of each grid cell is used to represent LULCC for managed and natural systems and is provided through an input file as described in Appendix C.

Both configurations of ELMv1.1-BGC also use the same fire parameterizations as in CLM4.5 (Li et al., 2012b; 2012a; Li, Levis, et al., 2013). Fires impact the model's ecosystems via loss of peat and biomass, vegetation mortality, and perturbation of carbon and nitrogen pools.

However, despite many common features, the emergent behaviors of the two configurations—such as the response of the global carbon sink to nutrient limitations—diverge because of other differences. The distinct approaches and features of the CTC and ECA configurations are described briefly in the following sections.

2.4.1. Default Land Biogeochemistry Configuration: Converging Trophic Cascade

The CTC biogeochemistry framework is the default representation of biogeochemistry within ELMv1.1. The CTC approach aims to capture the simplest and most tractable set of equations that can still represent the dominant ecosystem-level processes hypothesized to exert control over climate system feedbacks in the face of coupled carbon-nutrient interactions and multiple nutrient limitations.

The original implementation of the CTC approach focused on carbon and nitrogen dynamics in forest ecosystems with evaluation against flux observations and other in situ measurements (Thornton et al., 2002). Site-level model-data evaluations showed reasonable model response to the influence of large-scale forest disturbance processes and forest age structure (Law et al., 2001, 2003). The model is intended to achieve a dynamic but stable balance for energy, water, carbon, and nutrients when driven with constant or periodic forcings, and it uses a variant of the well-tested accelerated decomposition spin-up method (Thornton & Rosenbloom, 2005) to achieve that steady state at reasonable computational expense.

As implemented within an ESM, the primary purpose of the CTC is to solve research problems focused on global-scale climate-ecosystem feedbacks (Friedlingstein, 2015), with the objective of improving decadal- to century-scale climate predictions. The first climate-scale implementation of the CTC approach was as a component of the Community Land Model v4 (Oleson et al., 2010), a component of the Community Climate System Model (Gent et al., 2010). Simulations using this model showed that the CO₂ fertilization effect was likely overestimated by previous carbon-only global land biogeochemical model implementations (Thornton et al., 2007). Inclusion of nutrient limitation reduced the CO₂ fertilization effect, while also reducing carbon losses due to warming and increasing the sensitivity of carbon fluxes to precipitation. The CTC was later used in the first-ever, fully coupled, atmosphere-ocean-land-ice simulation with prognostic carbon and nutrient dynamics, where global-scale carbon climate feedbacks were profoundly influenced by nutrient limitation (Lindsay et al., 2014; Thornton et al., 2009).

For the current implementation within ELM v1.1, several significant developments to the CTC approach have been introduced. First, a carbon-nitrogen-phosphorus coupling developed by Yang et al. (2014) has replaced the earlier carbon-nitrogen coupling. While it is less well understood than nitrogen, phosphorus limitation may also significantly reduce global carbon uptake in response to rising levels of atmospheric CO₂. Phosphorus is believed to be a limiting nutrient for many lowland tropical forest ecosystems

(Cleveland et al., 2011; Vitousek & Howarth, 1991), which play a major role in the net carbon fluxes between land and atmosphere (Beer et al., 2010; Chhabra & Dadhwal, 2004; Sayer et al., 2007). Few ESMs have included representations of the effects of phosphorus limitation on ecosystems, but studies with land-only models that include phosphorus limitation find that it can significantly impact carbon uptake by terrestrial ecosystems (Wang et al., 2010a; Yang et al., 2016). The new carbon-nitrogen-phosphorus coupling resolves competition between vegetation and soil heterotrophic processes for mineral nutrient uptake on the basis of relative demand. The carbon-nitrogen-phosphorus implementation is similar to the approach used in earlier carbon-nitrogen versions of CTC (Thornton et al., 2002; Thornton & Rosenbloom, 2005), but allows shifts between four different nutrient limitation scenarios: no nutrient limitation, nitrogen limitation, phosphorus limitation, and colimitation. The limitation scenario is updated for each vegetated soil column during each model timestep.

A second significant CTC development for ELMv1.1 is the implementation of temporary carbon, nitrogen, and phosphorus storage pools for all plant types, and an associated revision in model response to nutrient limitation on plant growth. To assess which modifications would be required to reproduce observed behaviors, we first evaluated the model against observed (1) allocation of isotopically labeled carbon in a shade manipulation study (Mao et al., 2016), (2) fluxes and stable carbon isotopes in mature forest stands (Duarte, Raczka, et al., 2017; Raczka et al., 2016), and (3) rapid forest ecosystem carbon exchange using large chambers and paired nutrient fertilization (Metcalfe et al., 2017). These model-observation comparison studies all suggested that model performance can be improved by including new storage terms for plant carbon and nutrient pools. We therefore modified the model to allow carbon, nitrogen, and phosphorus storage in plant nonstructural pools, and introduced a storage turnover time controlling this storage for each element. Motivated by the same model-data evaluations, we changed the CTC handling of excess carbon. In the original implementation, plants responded to nutrient limitation by reducing carbon uptake through down-regulation of the photosynthetic rate. We replaced this with a new approach that allows excess carbon to accumulate in the plant storage pool, where it is released back to the atmosphere as a first-order loss process with a fixed time constant.

In addition, some of the prescribed values of vegetation physiological traits were updated on the basis of recent literature reviews and parameter sensitivity studies (Ricciuto et al., 2018).

2.4.2. Alternative Land Biogeochemistry Configuration: Equilibrium Chemistry Approximation

E3SMv1.1 includes an alternative approach to representing nitrogen and phosphorus limitations in soil biogeochemistry, the equilibrium chemical approximation (ECA Huang et al., 2018; Medvigy et al., 2019; Riley et al., 2018; Tang & Riley, 2013; Zhu et al., 2017). The ECA applies a functional coupling strategy to represent the multiple-consumer, multiple-substrate competition network composed of plant roots, soil microbes, and abiotic protection mechanisms (e.g., mineral surface interactions Medvigy et al., 2019; Tang & Riley, 2013; Tang, 2015; Zhu, Riley, et al., 2016; Zhu, Iversen, et al., 2016; Zhu et al., 2017).

The E3SMv1.1-BGC-ECA configuration is distinguished by several additional specific features. Dynamic resource allocation within plants is based on light, carbon, nitrogen, phosphorus, and water limitations (Friedlingstein et al., 1999; Sharpe & Rykiel, 1991). Variable plant stoichiometry prognostically affects plant physiology (e.g., photosynthetic capacity, allocation). Leaf, fine root, live stem, and dead stem carbon, nitrogen, and phosphorus are all flexible with baseline values constrained by observed stoichiometry for over 6,000 species (from the TRY database Kattge et al., 2011). This representation of plant stoichiometric flexibility has large effects on ecosystem carbon-nutrient interactions. Plant nutrient uptake is based on root functional traits rather than photosynthetic demand (Riley et al., 2018). Nutrient uptake in ELMv1.1-BGC-ECA is based on the capacity of plant nutrient uptake constrained by interactions with other nutrient consumers in the system (e.g., microbial decomposers, nitrifiers, denitrifiers, mineral surfaces). Plant physiology regulates N_2 fixation, and soil phosphorus acquisition strategies depend on root-nodulated fraction, nitrogenase activity, and temperature controls on enzyme kinetics (Grant, 2013; Wang et al., 2010b). We also include improvements to representation of nitrogen leaching (Zhu & Riley, 2015).

ELMv1.1-BGC-ECA has been evaluated against multiple observational data sets, including global carbon, water, and energy cycles (Zhu et al., 2019); diurnal cycles of nutrient uptake (Riley et al., 2018; Schimel et al., 1989); global soil carbon dynamics jointly using ^{12}C and ^{14}C observations from 671 sites around the world (Chen et al., 2019); short-term plant nutrient uptake (Riley et al., 2018); site-level tropical plant biomass (Holm et al., 2020); global patterns of nitrogen leaching versus gaseous losses (Houlton et al., 2015; Riley

et al., 2018; Zhu & Riley, 2015), and CO₂ fertilization effects on ecosystem carbon, nitrogen, and phosphorus processes in a tropical rainforest (Fleischer et al., 2019).

2.4.3. Differences in Land Component Initialization Approaches

The initialization of terrestrial ecosystem carbon and nutrient stocks in the preindustrial period also has important consequences for the simulated carbon cycle during the historical period (Koven et al., 2013; Thornton & Rosenbloom, 2005). Previous studies assessing climate-biogeochemistry feedbacks within Earth system models have assumed that the initial preindustrial state of the terrestrial carbon pools should be in equilibrium with the combined preindustrial forcings, and that a valid control simulation should have minimal drift in total global carbon stocks in the absence of anthropogenic forcings (e.g., Friedlingstein et al., 2006; Lindsay et al., 2014; Thornton et al., 2009; Zaehle et al., 2010). This approach was employed in the E3SMv1.1-BGC simulations in the default CTC configuration.

The E3SMv1.1-BGC-ECA simulations presented here used an alternative approach to initialize the soil phosphorus pools. Both the CTC and ECA initialization approaches used the global present-day soil phosphorus maps (Yang et al., 2014) for initialization of preindustrial global phosphorus stocks in surface soils. However, the ECA initialization approach diverged by assuming an exponential decline of phosphorus concentration from surface to deep soil, based on site observations by (Vaughan et al., 2007; van der Wal et al., 2007). This assumption led to significantly smaller subsurface (below 50 cm) soil phosphorus pools, and consequently less uptake of subsurface soil phosphorus, and significantly greater phosphorus limitation during the historical and future simulations, as compared with the default model.

Because of this difference, the ECA's smaller subsurface soil phosphorus pools were also more easily depleted. To minimize the departure of the soil phosphorus pools from the observationally based Yang et al. (2014) data set, the ECA initialization held soil phosphorus constant throughout the preindustrial spin-up. Soil phosphorus pools were then allowed to evolve during the historical transient simulation.

These design choices resulted in a drift nutrient stocks during simulations with either constant forcings or with forcings representative of the historical period. Further details about the initialization of ECA and differences between assumed initial states for available phosphorus between CTC and ECA are described in more detail in sections 3.1 and Appendix C3.

2.5. MPAS-Ocean Biogeochemistry

The E3SMv1.1-BGC configuration includes an implementation of the BEC model from CESM1, which consists of upper ocean ecological (Moore et al., 2001, 2004) and full-depth biogeochemical (Doney et al., 2006) dynamics. For over a decade, the BEC model has been shown to perform well according to a wide range of metrics, for example, in Doney et al. (2009) and Moore et al. (2013). The standard version of BEC has multiple phytoplankton functional groups (diatoms, diazotrophs, and small phytoplankton, some of which are implicitly assigned to be CaCO₃-shelled coccolithophores), a single zooplankton, several pools of dissolved organic matter, multiple limiting nutrients (nitrate, ammonium, phosphate, silicate, and iron), and inorganic carbonate chemistry. Iron:carbon and silicon:carbon ratios are allowed to vary, while carbon:nitrogen:phosphorus ratios are assumed to be fixed at the Redfield ratio (prescribed at 117:16:1 Moore et al., 2004), with the exception of the C:P ratio for diazotrophs which is 3 times larger. Riverine inputs of nutrients are prescribed from input files, and carbon and nutrients lost to sediments (export and burial) are removed from the model, resulting in a slight long term drift of these quantities.

The E3SMv1 adds the following novel features to the ocean biogeochemistry: (1) full two-way coupling of chemical constituents with the sea ice biogeochemistry (see section 2.6 below); and (2) prediction of oceanic dimethyl sulfide (DMS) production, including recently developed improved treatments of the strong DMS production by a fourth explicit phytoplankton functional group, the polar-adapted *Phaeocystis* (Wang & Moore, 2011). The treatment of *Phaeocystis* has been shown to impact the regional distribution of DMS production (Wang et al., 2015), with potentially important implications for high-latitude clouds and climate (Wang, Maltrud, et al., 2018).

In E3SMv1.1, the ocean biogeochemistry scheme has been implemented within the MPAS-Ocean, E3SM's ocean component model (Ringler et al., 2013). MPAS-Ocean replaces the previous DOE-developed model, the Parallel Ocean Program (Smith et al., 2010), which was the ocean component in the Community Earth System Model (CESM) at the branch point for E3SM development. MPAS-Ocean grid cells are generated via Voronoi Tessalations and are mostly hexagons for E3SMv1. The horizontal resolution was designed to

have a similar meridional distribution (on average) as the standard Parallel Ocean Program grid in CESM1, varying from 60 km in the midlatitudes to 30 km near the equator and poles. The vertical discretization was chosen to have the same 60-level distribution as CESM1, varying from 10 m at the surface to 250 m at depth, and is implemented as a *zstar* coordinate (Petersen et al., 2015; Reckinger et al., 2015). Advection is performed using flux corrected transport (Skamarock & Gassmann, 2011). Standard subgrid parameterizations were employed, such as the Gent-McWilliams (GM) eddy tracer transport (Gent & McWilliams, 1990), the Community Vertical Mixing project implementation of the K-Profile Parameterization vertical mixing (Van Roekel et al., 2018), and biharmonic momentum diffusion. The Redi coefficient, which adds diffusion along isopycnal layers, was set to zero in the E3SMv1-DECK configuration due to significant issues with its numerical formulation in the model, which were discovered late in the model's development cycle. We retain this setting in the E3SMv1.1-BGC simulations despite anticipating that interior tracer transport will be negatively affected; the numerical challenges in the implementation of Redi mixing in MPAS-Ocean are being addressed for future model versions as part of our current development efforts. For more details about the model configuration, see Golaz et al. (2019).

For all E3SMv1 model configurations, including the simulations presented here, there are no feedbacks between the ocean biogeochemistry and the physical ocean or climate states. The E3SMv1 has latent capabilities to simulate physical feedbacks from biogeochemistry onto climate, but these have been disabled for this set of simulations in order to reduce the complexity of the experiment. In particular, air-sea CO₂ flux is computed prognostically using the model's surface ocean *p*CO₂, but in the prescribed CO₂ concentration simulations discussed here, this has no radiative impact in the atmosphere. Similarly, the flux of DMS from the ocean to the atmosphere is calculated for diagnostic purposes, but the atmosphere uses only climatological DMS forcing. The model also has a capability to calculate the absorption of shortwave radiation in the surface ocean using the simulated chlorophyll distribution, but in these experiments this capability is not enabled.

2.6. MPAS-Seaice Biogeochemistry

Reviews analyzing the role of sea ice ecosystems have estimated they account for up to 25% of primary production in ice-covered waters, and their representation in models is important for projecting the implications of sea ice retreat for global oceanic primary production (Arrigo & Thomas, 2004; Arrigo et al., 2008).

MPAS-Seaice, the new sea ice component of E3SMv1, inherits many physical and biogeochemical formulations from the Los Alamos Sea Ice Model (CICE) (Hunke et al., 2015; Roberts et al., 2018), but with adaptations to use the nonuniform polygons of the MPAS meshes, which it shares with the MPAS-Ocean model. It simulates sea ice concentration, volume, velocity, and transport of tracers prognostically. Sea ice dynamics are calculated by solving the sea ice momentum equation (Hibler III, 1979; Hunke & Dukowicz, 1997, 2002); the primary thermodynamic state variables are ice enthalpy and salinity. The physical grid has seven vertical levels, while the biogeochemical grid has eight; the resolution of the vertical grid is on the order of centimeters. Within each vertical-level column, physical state tracers and biogeochemical tracer concentrations are defined and evolved within five subgrid ice thickness categories.

MPAS-seaice uses an early [or prerelease] version of the CICE column physics and biogeochemistry package Icepack (Hunke et al., 2019). The biogeochemistry scheme resolves nine biogeochemical components: three phytoplankton groups (diatoms, small phytoplankton, and *Phaeocystis* sp.), three macronutrients (nitrate, silicate, and ammonium), dissolved iron, and DMS and dissolved dimethylsulfoniopropionate produced by phytoplankton.

Each biogeochemical component tracer is carried by the model in two phases: (1) a purely mobile phase that advects with the brine and (2) an attached phase that adheres to the ice crystals. The concentration and velocity fields for the mobile and attached phase of each tracer are resolved in three dimensions. Vertical transport of the mobile phase tracers is based on the Jeffery et al. (2011) parameterization; their vertical transport follows the "mushy layer" vertical thermodynamics scheme of Turner and Hunke (2015). Attached-phase tracers, by contrast, retain their fixed vertical position within the ice column and are gained and lost only through ice growth and melt. Transfer between the mobile and attached phases is governed by prescribed adsorption and desorption time scales, which assume that ice growth facilitates adsorption while ice melt facilitates desorption.

Horizontal transport of ice concentration, volume, and tracers uses an incremental remapping scheme (Dukowicz & Baumgardner, 2000; Lipscomb & Hunke, 2004; Lipscomb & Ringler, 2005), which advects all biogeochemical components as volume-conserved tracers.

A novel feature in E3SMv1 is the full two-way coupling of biogeochemical tracers between ocean and sea ice, including organic and inorganic nitrogen, silicate, iron, dissolved organic carbon (DOC), and phytoplankton carbon (small, diatoms, and *Phaeocystis*). MPAS-seaice determines the ocean-ice fluxes of biogeochemical tracers based on ice growth and melt; snow loading, which can force ocean water into the sea ice brine channels; and brine expulsion, which depends on brine density, internal sea ice tracer concentrations, and upper ocean tracer concentrations from MPAS-Ocean.

For all E3SMv1 model configurations, including the simulations presented here, there are no feedbacks between the sea ice biogeochemistry and the physical sea ice or climate states.

2.7. E3SM Atmosphere Model

The E3SM Atmosphere Model (EAM) version 1 is the atmosphere component of E3SMv1, which branched from the Community Atmosphere Model (Neale et al., 2012). The atmosphere component of the CESM (Hurrell et al., 2013) has evolved considerably in E3SM, with a different dynamical core and substantially revamped suite of physics parameterizations, including replacing the turbulence and shallow convection parameterizations (Golaz et al., 2002; Larson & Golaz, 2005; Larson, 2017). EAMv1 uses a spectral element dynamical core with a cubed sphere geometry. The nominal horizontal resolution used for these simulations is 110 km and the model has 72 vertical layers from the surface to 60 km (~0.1 hPa).

An overview of the EAMv1 is provided in Rasch et al. (2019), including descriptions of innovations to the parameterized atmospheric processes. Cloud and convection characteristics are analyzed in Xie et al. (2018) and the model's sensitivity to various adjustable parameters is analyzed in Qian et al. (2018).

In E3SMv1, atmospheric processes are coupled with biogeochemical processes primarily via changes to surface energy exchanges (latent and sensible heat flux). However, in the real world, biogeochemistry on land and ocean is also coupled to atmospheric warming through a variety of other pathways. These include fluxes of CO₂ and non-CO₂ greenhouse gases, as well as fluxes of chemically reactive constituents that participate in atmospheric oxidation of chemically reactive greenhouse gases. Additionally, biogeochemical processes influence the surface exchanges of atmospheric aerosols and their precursor gases, which impact atmospheric radiation and clouds (Liu et al., 2012; Wang et al., 2020).

Several of the enhancements to aerosol and gas phase processes in EAMv1 (Wang et al., 2020), while currently not coupled to land and ocean biogeochemical processes, may facilitate such couplings in future model versions (section 7). These include

1. several improvements to the treatment of aerosol wet removal and other microphysical processes (Wang et al., 2013),
2. the introduction of a revised, and more explicit, scheme for secondary organic aerosol formation (Shrivastava et al., 2015),
3. the inclusion of organic matter into sea spray aerosol, as a step towards increased coupling of ocean biogeochemistry with atmospheric processes (Burrows et al., 2014), and
4. the introduction of a computationally efficient, dynamic treatment of stratospheric ozone, or linearized ozone chemistry (Hsu & Prather, 2009).

In E3SMv1.1-BGC, only the concentration-driven configurations of the atmosphere model are scientifically validated, that is, configurations with prescribed, globally homogeneous greenhouse gas concentrations. Several bugs affecting the mass conservation of nonwater advected tracers were not discovered until late in the development cycle and so could not be corrected for E3SMv1.1. These bugs have minor impacts on simulated concentrations of short-lived tracers (aerosols and their precursors), but may have significant cumulative effects on concentrations of long-lived greenhouse gases over longer simulations. For this reason and others, we caution against using the E3SMv1.1-BGC model for prognostic (emission-driven) CO₂ simulations until the known issues impacting carbon mass conservation can be addressed, and testing and verification completed. The results presented here are impacted by these bugs via their effects on the atmospheric concentrations of aerosols and their precursor gases, but we expect these impacts to be small due to their much shorter atmospheric residence time.

2.8. MOSART River Model

The Model for Scale Adaptive River Transport (MOSART) is the new river model component of E3SM. In E3SMv1.1, only the module for water-related processes is incorporated, that is, MOSART-water. MOSART-water provides physically based simulations of key hydrological variables, such as channel water depth, velocity, and surface area, that critically control the transport of riverine energy and biogeochemical processes (Li, Wigmosta, et al., 2013; Li, Leung, et al., 2015). Future developments of MOSART will incorporate biogeochemical features, for example, transport of nutrients and sediments, and are discussed in section 7.

3. Component and Coupled Model Tuning and Spin-up

Spin-up to produce initial conditions for a coupled Earth System Model is computationally expensive. For E3SMv1.1-BGC, we have taken the approach of spinning up the land component separately, to allow a long-term equilibration of land carbon pools at a much smaller computational cost, before combining it with a separately spun-up ocean and atmosphere state. We also significantly reduced resource requirements by limiting our ocean biogeochemistry spin-up to several hundred years. As we will discuss in greater detail later, while this length of simulation is not sufficient to equilibrate ocean biogeochemical fields in the deep ocean, it was sufficient to achieve our aim of conducting an initial assessment of the BEC model's behavior following its implementation into the MPAS-Ocean in E3SMv1.1-BGC. A schematic overview of the overall spin-up procedure is shown in Figure 4, and additional details of the spin-up procedure, and of all bug fixes applied during the spin-up, are provided in the supporting information.

3.1. Spin-up of Land Biogeochemistry

The initial land-only spin-up, for both the CTC and ECA biogeochemistry configurations, progressed in two phases. In the first phase, an accelerated decomposition method was applied during 200 simulated years to rapidly achieve initial equilibrium states for the slowly evolving nitrogen and carbon pools (Koven et al., 2013; Thornton & Rosenbloom, 2005). In the second phase, land-only simulations were continued in the normal operation mode until carbon and nitrogen pools reached a dynamic equilibrium state, which occurred after 710 (CTC) or 300 (ECA) years. Atmospheric boundary conditions were prescribed by repeatedly reading the 3-hourly instantaneous outputs from a 25-year period of the E3SMv1-DECK preindustrial spin-up simulation. Once nutrient pools were approaching equilibrium in the land-only simulations, these simulations were used to initialize the land model state for additional phases of partly and fully coupled spin-up (Figure 4).

Because some of the processes governing the global distribution of soil phosphorus stocks operate on geologic time scales, it is not possible at this time to perform a fully prognostic model spin-up from “bare ground” conditions to initialize phosphorus pools with slow turnover times. Instead, we rely on global maps of soil phosphorus pools synthesized from observations (Appendix C3; Yang & Post, 2011; Yang et al., 2013), which have previously been used successfully in land model simulations using prescribed atmospheric forcings (Yang et al., 2016).

In both the CTC and ECA configurations, phosphorus pools were initialized using these global phosphorus maps, but the initialization was handled differently in the two configurations. These differences reflect, in part, the lack of observational constraints on historical and present-day soil phosphorus levels. For example, it is not clear how soil phosphorus levels have evolved over the historical period, nor to what extent it is appropriate to treat preindustrial soil phosphorus pools as being in equilibrium with other ecosystem processes, due to the long time scales involved in the phosphorus cycle. Given this paucity of observational constraints, the developers of these two configurations made different choices about the treatment of phosphorus in the spin-up and initialization of the model.

In CTC, phosphorus was prescribed to be infinitely available (i.e., not limiting to plant growth and microbial decomposition) during the first spin-up phase (200 years of accelerated decomposition dynamics). All soil P pools were then initialized from the global maps at the start of the second spin-up phase, and allowed to evolve with full prognostic C-N-P cycling during all subsequent spin-up phases (710 years of offline land simulation plus 600 years of coupled simulation without ocean BGC + 265 years of coupled simulation with ocean BGC), allowing vegetation, soil organic matter, and phosphorus pools to approach their internally consistent preindustrial dynamic equilibrium values. The turnover times for rock-derived

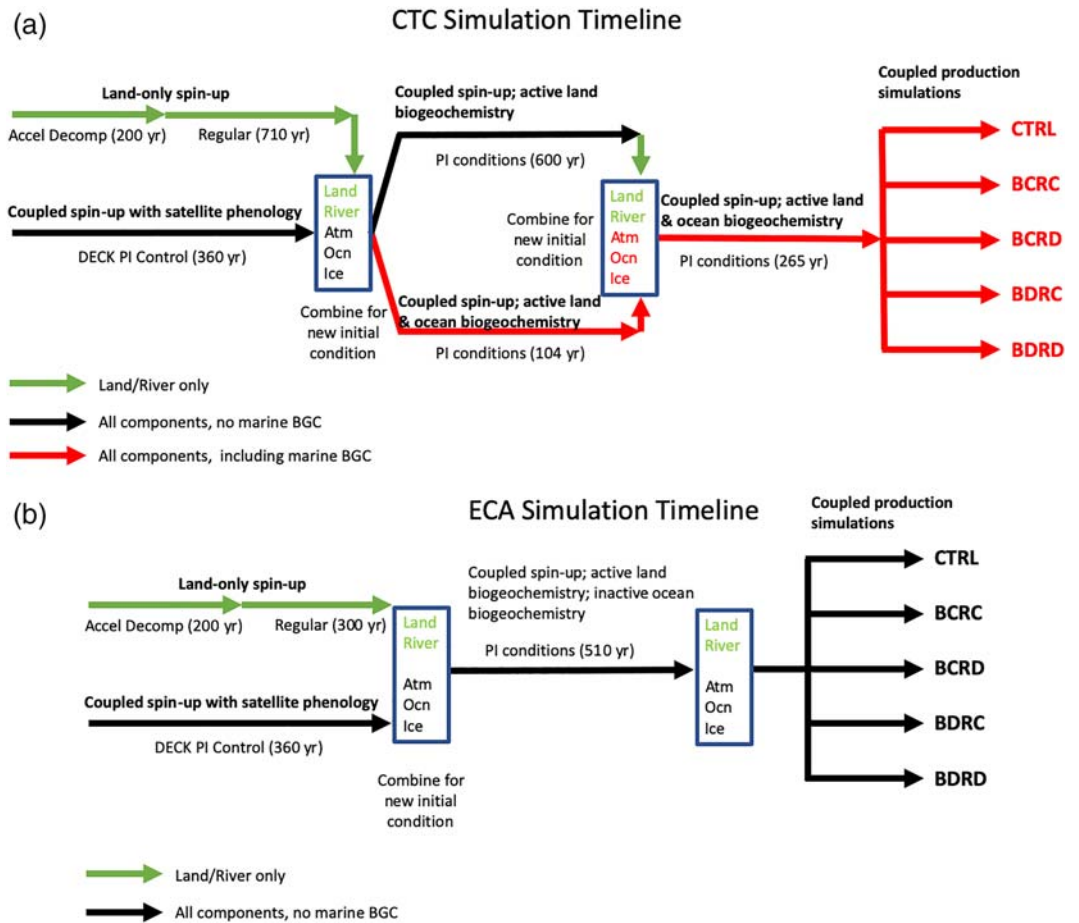


Figure 4. Summary of model spin-up steps and simulation campaign initialization: (a) CTC simulation spin-up; (b) ECA simulation spin-up.

and mineral-associated P are very long, and we found that there was minimal drift in the preindustrial equilibrated soil P values for CTC as compared to the global maps used for initialization.

In ECA, soil phosphorus pools were initialized from global maps and held constant at prescribed values throughout the entire spin-up (500 years of offline land simulation plus 510 years of coupled simulation without ocean BGC). With this approach, the fluxes of P depend on the initial P pool sizes, but the pool sizes are not allowed to update during the spin-up, so fluxes of P from the pools are not depleting the pools during this period. One consequence of this approach is that the preindustrial soil P states match the global soil P maps exactly. Another consequence is that the soil P pools are not in dynamic equilibrium with the rest of

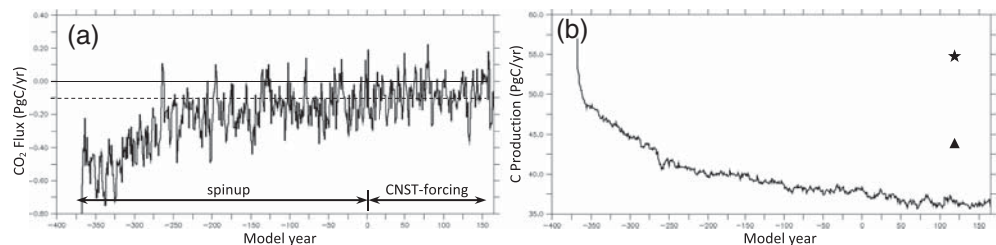


Figure 5. (a) Globally integrated CO_2 air-sea flux (positive values denote flux into the atmosphere) and (b) ocean primary production by phytoplankton in PgC/year from the beginning of the spin-up phase through 2014 of CNST-forcing showing the approach to equilibrium. The dashed line in (a) denotes the target equilibrium threshold of $0.1 \text{ PgC}/\text{yr}$. The star in (b) is an estimate from Ma et al. (2014), and the triangle is from Behrenfeld and Falkowski (1997).

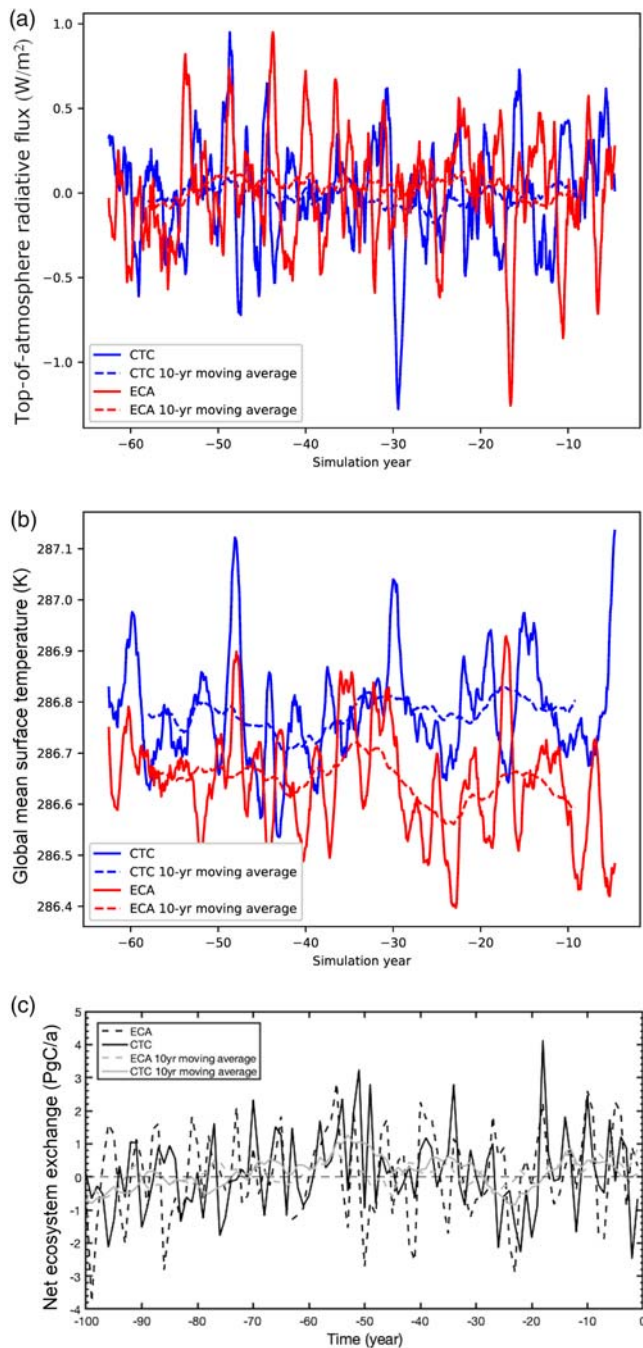


Figure 6. (a) Global mean net top-of-atmosphere radiative balance, (b) global mean surface air temperature, and (c) NEE from the final years of the CTC (solid lines) and ECA coupled spin-up simulations (dashed line).

the model processes at the start of the historical transient simulation. This leads to transient dynamics in the ECA simulations, including in the historical control simulation, as the soil P pools adjust in response to their disequilibrium state. Tests were conducted using the same initialization approach in ECA as described above for CTC, and it was found that the soil P pools in ECA were depleted too rapidly during the spin-up phase, resulting in P limitation that was deemed excessive at the preindustrial state. For both the CTC and ECA approaches to soil P pool spin-up, there is P limitation to vegetation growth and decomposition in the preindustrial state at the start of the historical transient simulations.

The two models also differ in the assumptions made about how initial soil P pools are distributed with depth. Very few observations are available to constrain the present-day vertical profiles of soil phosphorus below 50-cm depth, and this problem is of course more acute for the preindustrial period. For the CTC configuration the 0–50 cm soil P pools from observationally constrained input maps are assumed to apply to the full modeled soil depth (3.8 m). The ECA configuration assumes an exponential decrease in the phosphorus profiles below 50 cm, resulting in less column-integrated soil P for ECA than for CTC. The impact of these choices and the differences in subsequent evolution of nutrient pools is discussed in section 5.3.

We evaluated the spin-up of the land biogeochemical state by the following criteria:

1. We required a balanced land-atmosphere carbon exchange, that is, net ecosystem exchange (NEE) near zero with minimal drift (Figure 6c). Mean NEE over the 164-year constant-forcing (control) experiment was 0.02 PgC/yr for the default CTC configuration (section 5.1), well below the ± 0.1 PgC/yr threshold recommended for the C4MIP by (Jones et al., 2016). For the ECA simulations, mean NEE over the same spin-up period was 0.12 PgC/yr.
2. We also performed a qualitative evaluation of the spatial distributions of NEE, global total vegetation biomass and global total soil carbon.
3. Finally, we examined the time series of the global mean total vegetative carbon, soil carbon, GPP, net primary productivity, and nitrogen and phosphorus mineralization to ensure that temporal trends in these variables were minimized, but did not apply formal threshold criteria.

As noted above, the ECA simulation was also not in dynamic equilibrium during the 164-year constant-forcing (control) experiment, with a mean NEE of 0.78 PgC/yr over that period, or a net loss of 128.5 PgC from land. ECA was in good dynamic equilibrium for an equivalent duration at the end of its coupled model spin-up simulation, prior to release of soil P pool constraints.

3.2. Spin-up and Tuning of Ocean Biogeochemistry

To conserve computational resources, the ocean biogeochemistry was initially spun up in a separate, parallel effort in 104 years of fully coupled E3SMv1.1 simulations. For the CTC configuration, this model state was combined with the land model state from year 601 and the simulation was continued for another 265 years. In total, the ocean biogeochemistry was spun up for 369 years within coupled simulations.

Our primary aim in initializing the ocean biogeochemistry state variables was to achieve reasonable agreement with observational benchmarks for the surface ocean (such as the present-day observational data sets that we compare with model fields in section 4.5). This was judged adequate for achieving our primary goal,

that is, an initial evaluation of any major biases occurring in the behavior of the BEC biogeochemistry following its implementation into the MPAS-Ocean model. A full spin-up of ocean biogeochemistry fields in Earth System Models typically requires at least several thousand simulation years due to the long equilibration time scales of the deep ocean. This level of computational burden was felt to be premature for an initial evaluation of the ocean biogeochemical behavior in the absence of full carbon cycle coupling, so we did not attempt it. As a consequence of this somewhat short spin-up, the ocean continued to take up CO₂ throughout the preindustrial control simulation, as can be seen in Figure 5. Nevertheless, the exercise has enabled us to identify several important issues in the E3SMv1.1-BGC model's ocean biogeochemistry, which will be discussed later in this paper, and we are now targeting these issues as priorities for improvement in current development efforts.

We judged the spin-up of the ocean biogeochemical state adequate to our purposes by the following criteria:

1. We required that the absolute value of the globally integrated air-sea CO₂ transfer be less than 0.1 PgC/yr when averaged over a period of at least 30 years, with minimal drift, in accordance with (Jones et al., 2016). Although 30 years is a relatively short time for determining quasi-stationarity, it proved to be sufficient since the resulting imbalance was 0.08 PgC/yr averaged over the 164-year period of the constant-forcing (control) simulation. (Figure 5a).
2. We also performed qualitative evaluations of the spatial distributions of phytoplankton biomass and nutrient distributions.
3. Finally, we examined the time series of the global mean primary productivity (Figure 5b) to ensure that the temporal trend was small, but did not apply a formal threshold criterion. Global nutrient inventories were confirmed to be drifting slightly (1.5% or less per century) due to the imbalance of riverine inputs and removal in the benthos.

3.3. Spin-up and Tuning of Sea Ice Biogeochemistry

The MPAS-seaice biogeochemical submodule, Icepack 1.0 (Roberts et al., 2018), was tuned initially in one-dimensional configurations of the Arctic (Duarte, Meyer, et al., 2017) and the Southern Ocean (Jeffery & Hunke, 2014).

The sea ice biogeochemistry was then further tuned in ocean-ice simulations using E3SMv1.1 and related models. In ocean-ice configurations, the sole tuning criteria was the best fit between simulated ice-integrated chlorophyll and observations from six field locations: three in the Arctic—the Norwegian Sea (Duarte, Meyer, et al., 2017), Barrow (Lee et al., 2008), and the Bering Sea (Gradinger et al., 2012); and three in the Southern Ocean—the Western Weddell Sea (Lannuzel et al., 2013), West Antarctic Peninsula (Massom et al., 2006), and Prydz Bay (Paterson & Laybourn-Parry, 2012).

3.4. Spin-up and Tuning of the Physical Climate State in Coupled Spin-up Simulations

We initialized the spin-up of the coupled E3SMv1.1-BGC model by branching from the E3SMv1.0-DECK preindustrial control simulation. The climate of the E3SMv1.0-DECK has been extensively evaluated and documented in Golaz et al. (2019), so we do not discuss the climate features of the model in great detail here. However, in E3SMv1.1-BGC, due to the combined effect of using the active land model and two minor bug fixes (see Supporting Information for details), the E3SMv1.1-BGC model experienced a small change in the net top-of-atmosphere radiation balance, bringing the preindustrial spin-up slightly out of its steady-state condition. This necessitated a minor retuning of atmosphere model.

In evaluating this small retuning, we applied the same primary criteria as were applied to the E3SMv1.0-DECK Golaz et al. (2019); that is:

1. The model must have a balanced radiative state, that is, a mean globally integrated net top-of-atmosphere radiative balance close to zero. This is critical since the model will otherwise experience significant climate drift. After retuning, the E3SMv1.1-BGC model had a net top-of-atmosphere radiative balance averaged over the last 50 years of spin-up was -0.057 W/m^2 (CTC) and 0.036 W/m^2 (ECA), with a slope of $-1.7 \times 10^{-3} \text{ W/m}^2/\text{yr}$ (CTC) and $-1.7 \times 10^{-3} \text{ W/m}^2/\text{yr}$ (ECA). (Figure 6a).
2. The global mean surface temperature (at 2-m reference height) must be close to the expected preindustrial value and with minimal trend (Figure 6b). This is a key metric since observational constraints exist for the preindustrial surface atmospheric temperature. The global mean surface temperature averaged over 50 years was 286.79 K (CTC) and 286.64 K (ECA), with a slope of $1.9 \times 10^{-3} \text{ K/yr}$ (CTC) and

-2.0×10^{-3} K/yr (ECA). This is slightly cooler than the 286.95 K global mean surface temperature of the E3SMv1-DECK preindustrial spin-up (500-year long-term average), and well within the range of global mean surface temperatures of the CMIP5 models, which mostly fall within the range 13–14°C (286.15–287.15 K; Hawkins & Sutton, 2016). It is also consistent with observational estimates of the present-day surface temperature (14.00°C for the period 1961–1990) and the linear change in surface temperature from the preindustrial to the present-day (0.57°C for the period 1861–1997 Jones et al., 1999).

We also examined various other properties of the physical climate and determined that, after these minor changes and retuning, the climate remained otherwise similar to the E3SMv1.0-DECK preindustrial control simulation. Since no other notable differences were identified, we refer the reader to Golaz et al. (2019) for further documentation of the model's physical climate.

4. Preindustrial and Historical Simulations: Description and Observational Benchmarking

4.1. Experimental Design and Overview of the Simulations

As discussed in section 1, carbon cycle interactions with nitrogen and phosphorus nutrient cycles exert significant control on climate, but considerable uncertainty surrounds the approaches to representing these processes in ESMs. The simulations presented here exploit a rare opportunity to examine the role of nutrient limits in two structurally different approaches to modeling the biogeochemistry of soils (CTC and ECA) within an otherwise identical ESM framework.

Additionally, our simulations are designed to facilitate the calculation of feedback parameters characterizing the strength of the coupled carbon-climate feedbacks in the E3SMv1.1 model. When framed as a climate forcing, the feedbacks between the carbon cycle and climate are of similar magnitude as cloud-climate feedbacks (Friedlingstein et al., 1999; Gregory et al., 2009), and hence are one of the most important—that is, probably both large and poorly constrained (Friedlingstein et al., 2014)—uncertainties in predicting the climate response to emissions of CO₂ in the future.

To characterize the strengths of the feedback parameters, β (the CO₂ fertilization effect) and γ (the climate-only effect on carbon), we follow the methodology of Gregory et al. (2009), with modifications that will be described in section 6.2. This methodology requires running the simulations using four different coupling scenarios to quantify the strength of biogeochemical and radiative impacts of CO₂, and their nonlinear interactions.

In these coupling scenarios, we separately prescribe the CO₂ concentrations experienced by biogeochemical systems on land and in the ocean (“B”) and the CO₂ concentrations experienced by the atmosphere model's radiative transfer codes (“R”). In each experiment, the prescribed concentrations of CO₂ are either held constant at 1850 levels (“C”) or increased along historical diagnostic (“D”) pathways (as opposed to prognostically simulated based on emissions).

All of these scenarios follow historical pathways (“hist”) for all non-CO₂ forcings. Historical simulations were completed for the time period 1850–2014.

Additionally, a control simulation or constant (CNST)-forcing was performed, which used repeated 1850 conditions for all forcings, including LULCC, atmospheric aerosol emissions, and others as described in Appendix C. Long-term trends in the CNST-forcing simulation serve to diagnose and control for potential drifts in climate conditions associated with incomplete spin-up of long-timescale climate processes.

An overview of the simulations described in this paper is provided in Table 3.

All simulations were initialized from the final year of the coupled spin-up simulation for the respective model configuration, as described in section 3. Input data sets followed the CMIP6 specifications as closely as possible, they are identical to those used in the E3SMv1.1-DECK experiments, and are described in more detail in Appendix C. In addition, these simulations also required input data sets for the atmospheric nitrogen deposition to land and ocean.

Each simulation has a single, unique execution script for provenance and reproducibility, as described in section A0.5. All simulations were performed on Edison at the National Energy Research Scientific Computing Center. All code, input data, and compsets for the simulations are available at tis.ucar.edu

Table 3
E3SMv1.1-BGC Simulations Overview

Config-uration	Experiment / CO ₂ coupling	Intercomparison (if any)	Experiment name from intercompari-son	Simulation years for external forc-ings	Biogeochemical CO ₂	Radiative CO ₂
CTC	Spin-up	N/A	N/A	1850	constant	constant
	CNST-forcing	C4MIP / DECK	piControl	1850	constant	constant
	BCRC-hist	N/A	N/A	1850–2014	constant	constant
	BDRC-hist	C4MIP (Tier 2)	hist-bgc	1850–2014	diagnostic	constant
	BCRD-hist	N/A	N/A	1850–2014	constant	diagnostic
	BDRD-hist	C4MIP / CMIP6 historical	historical	1850–2014	diagnostic	diagnostic
ECA	Spin-up	N/A	N/A	1850	constant	constant
	CNST-forcing	C4MIP / DECK	piControl	1850	constant	constant
	BCRC-hist	N/A	N/A	1850–2014	constant	constant
	BDRC-hist	C4MIP (Tier 2)		1850–2014	diagnostic	constant
	BCRD-hist	N/A	N/A	1850–2014	constant	diagnostic
	BDRD-hist	C4MIP / CMIP6 historical	historical	1850–2014	diagnostic	diagnostic

Note. The “constant” CO₂ is held at 1850 concentration, while “diagnostic” CO₂ increases along CMIP6 historical pathway (see text for details). “Simulation years” are noted for the external forcing files, that is, solar inputs, aerosol emissions, LULCC, and atmospheric nitrogen deposition.

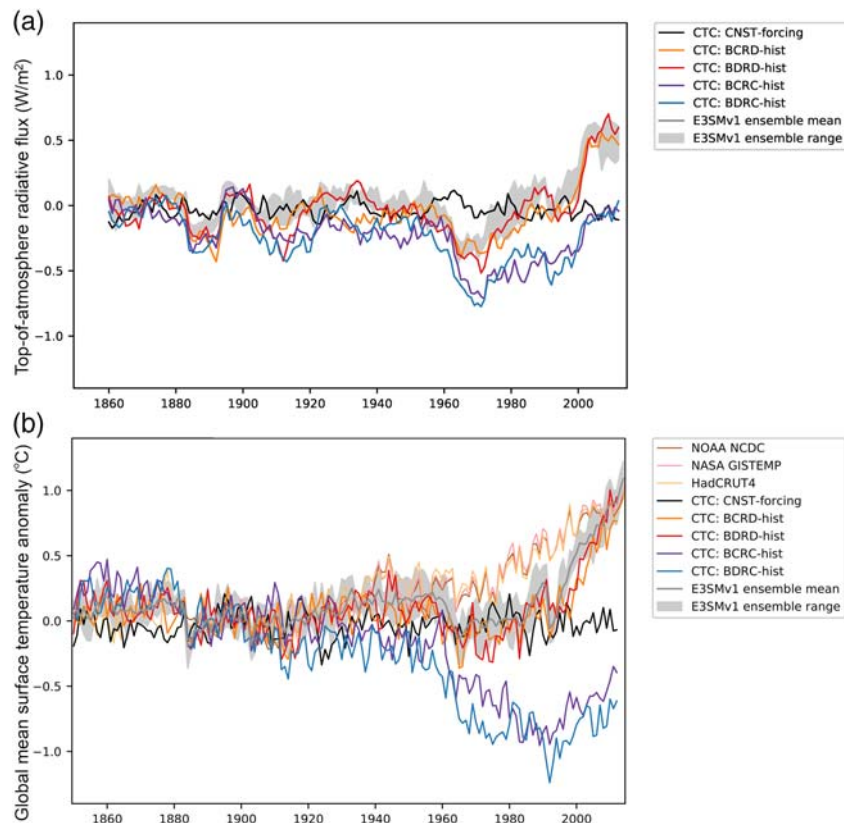


Figure 7. Time evolution of E3SMv1.1-BGC simulated global mean (a) net top-of-atmosphere radiative flux (with 10-year running mean), and (b) atmospheric temperature anomalies at 2-m reference height, for all historical CO₂ coupling cases and CNST-forcing. Anomalies for each temperature time series are calculated relative to its average over the period 1880–1909.

(<https://github.com/E3SM-Project/E3SM>). The E3SMv1.1-BGC simulations used the v1.1.0 tag (or git hash 19ab75a36d7c0d18a52107ad30ee312f796c3be8). The ECA simulations used the v1.1.1 tag (or git hash 25c94366a5888316aa3194940943e7ff86f21318).

Each simulation was continuously executed on a single compute cluster to avoid the risk of discontinuities due to architecture and compiler changes. In a minor exception to this, years 2000–2014 of the E3SMv1.1-CTC BCRD simulation had to be completed on a different computing platform due to the original platform being permanently taken offline.

4.2. Evaluation of Physical Climate

Before considering aspects of the simulation that are specific to the model's biogeochemical features, we briefly examine the model's overall climate and its transient evolution in the different CO₂ coupling scenarios. In this section, we focus only on simulations done in the default CTC configuration. The physical climate in the ECA is very similar and analogous figures for those simulations are provided in the supporting information (Text S2 and Figures S3–S8).

In the BCRD-hist scenario, the model's climate is generally quite similar to the climate of the DECK ensemble described by Golaz et al. (2019). Therefore, we do not repeat the detailed comparisons with observational benchmarks of the physical climate system presented in that paper, but instead focus on a smaller number of key climate metrics demonstrating the similarity of the historical trend and present-day climatology. Additionally, we highlight some physical climate features that respond differently in the four different coupling scenarios.

In Figure 7, we show time series of the global mean top-of-atmosphere radiative balance and the global mean 2-m air temperature, together with the same variables from the five-member DECK simulation ensemble and observational benchmarks for temperature. The preindustrial control simulation (CNST-forcing) exhibits a stable global mean surface temperature and near-zero net radiative balance, indicating the initial condition of the coupled simulation had attained a well-equilibrated physical climate state.

The differences between the CNST-forcing and BCRC-hist simulation represent the combined effects of all historical forcings except the rising CO₂ concentration. These include the impacts of major volcanic eruptions, which can be clearly seen in the net top-of-atmosphere radiative balance (e.g., the 1883 Krakatoa and 1991 Pinatubo eruptions). When the CO₂ greenhouse effect is not operative (BCRC-hist and BDRD-hist), the cooling impacts of aerosols and their interactions with clouds dominate the energy balance, resulting in a net cooling of more than 1 K by the end of the twentieth century. When the CO₂ greenhouse effect is operating (BCRD-hist and BDRD-hist), the greenhouse warming nearly balances the cooling impacts of aerosols until the late twentieth century. The net effect is a slight midcentury cooling, followed by a strong warming after 1960, with a net warming effect of ca. 0.5° by 2014.

This result is consistent with the E3SMv1.0-DECK ensemble and the analyses of Golaz et al. (2019), which found that the E3SMv1.0 has a comparatively strong climate response to aerosol (aerosol direct and indirect effects) and also a strong response to CO₂ (climate sensitivity). Additionally, it is worth noting that there is no detectable difference in the time series of global mean surface temperature between the paired BC and BD cases, indicating that biogeochemical feedbacks onto global mean surface temperature are minimal in these simulations. This will be discussed in greater detail in section 6.2.

Snow cover generally agreed well with observations, and showed some sensitivity to the climate radiative effect. Figure 8(a) compares December–February mean (1979–2014) snow water equivalent (SWE) with observations from GlobSnow-2 (<https://www.globsnow.info/swe/> Takala et al., 2011). Simulated SWE generally agreed well with observations, except for overpredictions in the mountainous regions of western North America and in Eastern Eurasia. We also compared the temporal evolution of DJF SWE over Northern Hemisphere land, excluding glacial regions (Figure 8(b)). Both the BDRD-hist and BCRC-hist simulations experienced a rapid SWE increase from 1950 to around 1980, which was associated with increased snowfall and an increased persistence of SWE through summertime in some higher latitude grid cells.

As expected, the ocean and sea ice states in our simulations display the same biases described in Golaz et al. (2019), many of which have a direct influence on the marine biogeochemistry. Of particular importance is the presence of overly extensive sea ice in the Labrador Sea (Figure 9a). This results in a strong cold and fresh water bias, which is observable as a dominant signature in the sea surface temperature and sea

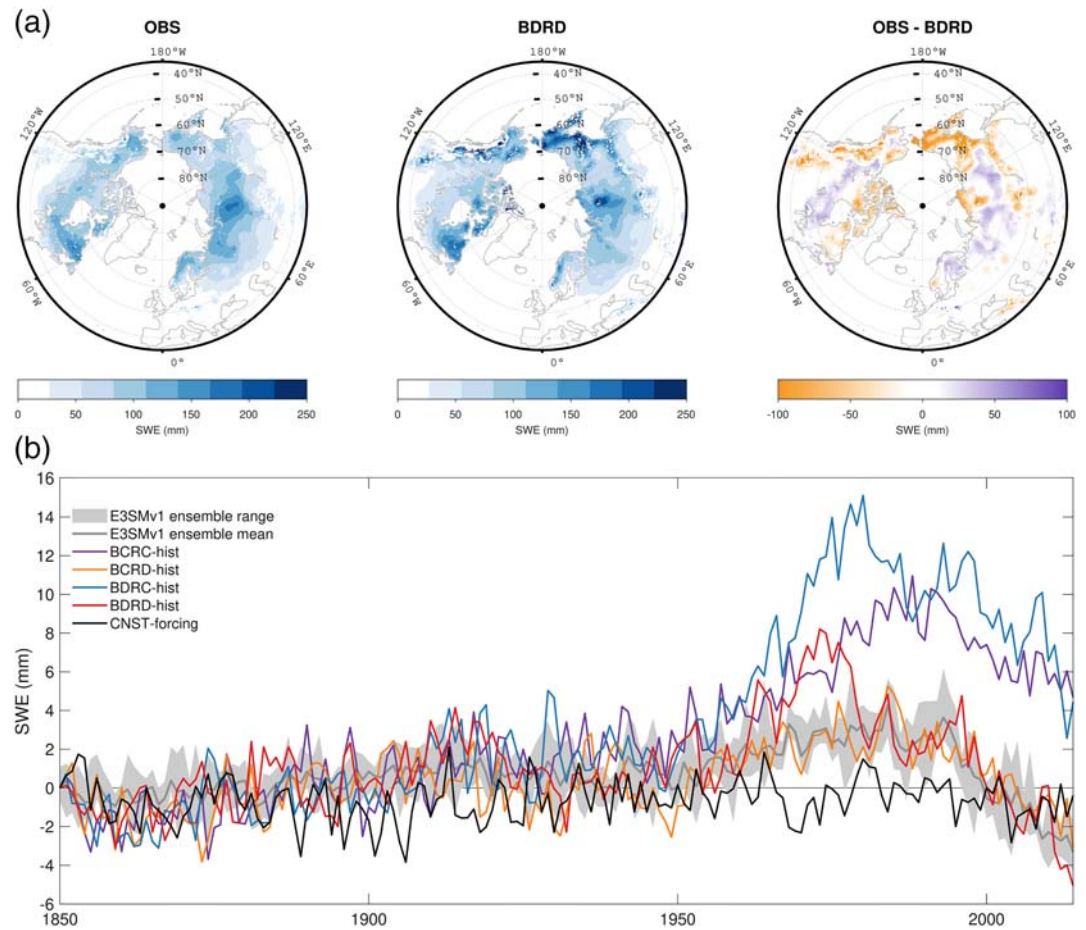


Figure 8. (a) Northern Hemisphere DJF mean snow water equivalent (SWE) comparisons between GlobSnow-2 observation and E3SMv1.1-BGC BDRD-hist simulation from 1979 to 2014. For consistency with observations, simulation results in glacier and mountainous areas are masked out using the GlobSnow-2 masking files. (b) Time series from 1850 to 2014 of DJF mean SWE from E3SMv1.1-BGC simulations, as anomalies relative to 1850, over the Northern Hemisphere land grids. Gray-shaded area shows range of five-member DECK historical ensemble (Golaz et al., 2019). In the time series, glacial grid cells have been excluded from the calculation of globally integrated SWE, that is, grid cells where SWE exceeds 1,000 mm throughout an entire summer in any year during the simulation.

surface salinity of the subpolar gyre (Figures 9b and 9c). These effects combine to create an overly stable water column, resulting in extremely shallow mixed-layer depths (Figure 9d). Not only does this contribute to a weak Atlantic meridional overturning circulation of about 11 Sv (Golaz et al., 2019), but also strongly curtails the replenishment of nutrients into the photic zone, resulting in very low productivity and biomass (see section 4.5).

Sea ice biogeochemistry is strongly impacted by the extent, thickness, and seasonal cycle of sea ice. Additional figures documenting biases in the model's present-day sea ice thickness, as compared with observations (Zwally et al., 2002), are included in the supporting information (Text S1 and Figures S1 and S2).

4.3. Observational Benchmarking of Land Biogeochemical and Physical Variables

We now turn to an evaluation of the land model in the BDRD-hist simulations. We evaluate the present-day simulated land biogeochemistry in comparison with a large suite of present-day observational benchmarks using the ILAMB package (section 4.3). The ILAMB package (Collier et al., 2018; Hoffman et al., 2017) was developed as a community effort to harmonize many disparate observational data sets, types of evaluation criteria, and types of model predictions into a single software package that can be used to quantify land model skill. The package evaluates land model results against a wide range of observationally inferred metrics (e.g., from in situ, remote sensing, and reanalysis-derived products), focusing on period mean bias, root-mean-square error (RMSE), spatial heterogeneity, and temporal dynamics (e.g., interannual variability

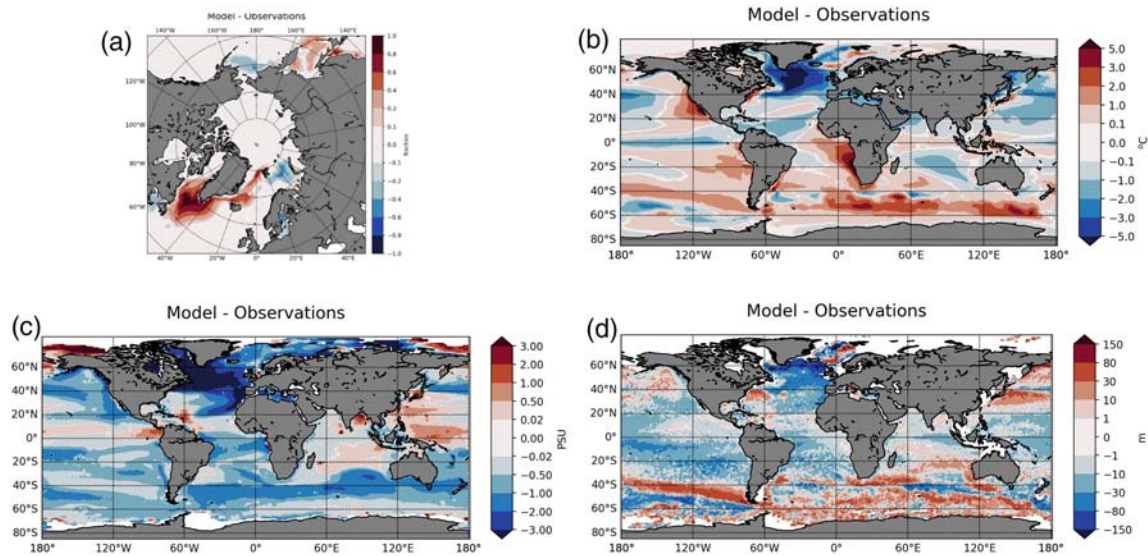


Figure 9. Differences between simulated fields averaged over the final 30 years of BDRD and observations (a) sea ice fraction relative to NASA Team satellite data (Cavalieri et al., 1996), (b) sea surface temperature ($^{\circ}\text{C}$) relative to the Hadley National Oceanic and Atmospheric Administration (NOAA)/Optimal Interpolation merged sea surface temperature data set (years 1985–2014, Hurrell et al., 2008), (c) sea surface salinity (psu) relative to the Aquarius satellite observations (Project, 2010), and (d) mixed layer depth (m) relative to Holte-Talley Array of Real-time Geostrophic Oceanography-based observations (Holte et al., 2017)

and seasonal cycles of carbon fluxes). Observational uncertainty estimates are included, although these estimates are somewhat qualitative, since many available data sets do not explicitly quantify uncertainty. We view the resulting metrics—which span the carbon, hydrology, radiation and energy cycles, climate forcings, and functional relationships—as important for evaluating model processes requiring more development and tracking improvements in model performance over time, rather than as indicating whether a model is “good” or “bad” overall.

We used ILAMB to assess the BDRD-hist simulations both E3SMv1.1-BGC configurations over the period 1980–2005, and compare them with nine CMIP5 land models and the multimodel mean of those CMIP5 models. A high-level “scorecard” summary of this assessment is shown in Figure 10; we also encourage readers to explore the interactive online version of this scorecard (<https://doi.org/10.6084/m9.figshare.11097356/>), which enables users to view all of the underlying geographic and temporal comparisons that make up these scores. These comparisons indicate the E3SMv1.1 configurations exhibit similar performance and outperform most CMIP5 models for nearly every variable. The superior performance shown by the E3SMv1.1 configurations is likely attributable to a combined effect of better mean atmospheric forcings, as indicated in the gray rows in Figure 10 (and further documented in Golaz et al. (2019) for the E3SMv1.0-DECK version), and of recent land model improvements.

As expected, the CMIP5 multimodel mean outperforms any single CMIP5 model. The E3SMv1.1-BGC model configurations show performance similar to the CMIP5 multimodel mean, with the CMIP5 multimodel mean outperforming either E3SMv1.1-BGC configuration to some degree for GPP, LAI, global net ecosystem carbon balance, ecosystem respiration, latent and sensible heat, and diurnal maximum temperature (an atmospheric forcing). In only four cases does either E3SMv1.1-BGC configuration exhibit worse than average performance among this collection of models.

In addition to the 30-year temporal and global mean comparisons with carbon cycle observations presented in the next section, the spatial and temporal structure of global carbon fluxes are important components of land model evaluation. ILAMB metrics combine model-observation comparisons for flux magnitudes, spatial structure, and monthly and interannual variability temporal dynamics. Both the CTC and ECA configurations performed better than most individual CMIP5 models for the dominant carbon exchanges with the atmosphere (GPP, NEE, and ecosystem respiration; Figure 10). The relatively better ECA scores for these land-atmosphere carbon exchange metrics (GPP, NEE, ecosystem respiration) resulted from improved estimates of both spatial and temporal structure. For the two metrics that are most relevant to the coupling with

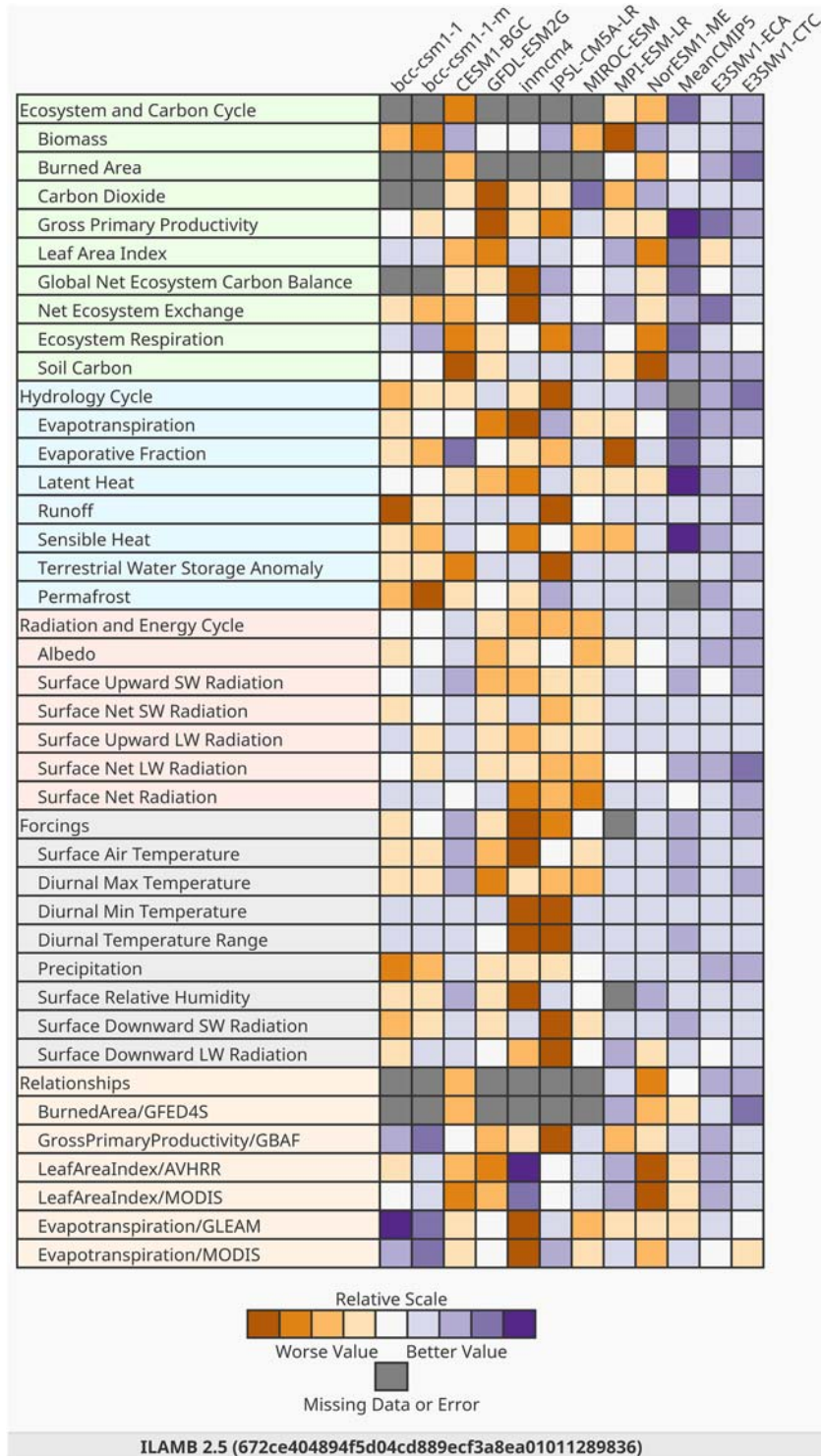


Figure 10. The performance of both land model configurations of E3SMv1.1 (model columns 11–12) was assessed and compared with that of nine CMIP5 land models (model columns 1–9) and the multimodel mean of those CMIP5 models (model column 10) using the ILAMB package (Collier et al., 2018). The E3SMv1.1 results were drawn from the concentration-forced (BDRD) CMIP6 historical simulations (Eyring et al., 2016), while the other model results came from the concentration-forced CMIP5 historical simulations (Taylor et al., 2012). Since the CMIP5 historical simulations ended after year 2005, all models were evaluated in ILAMB for the period 1980–2005.

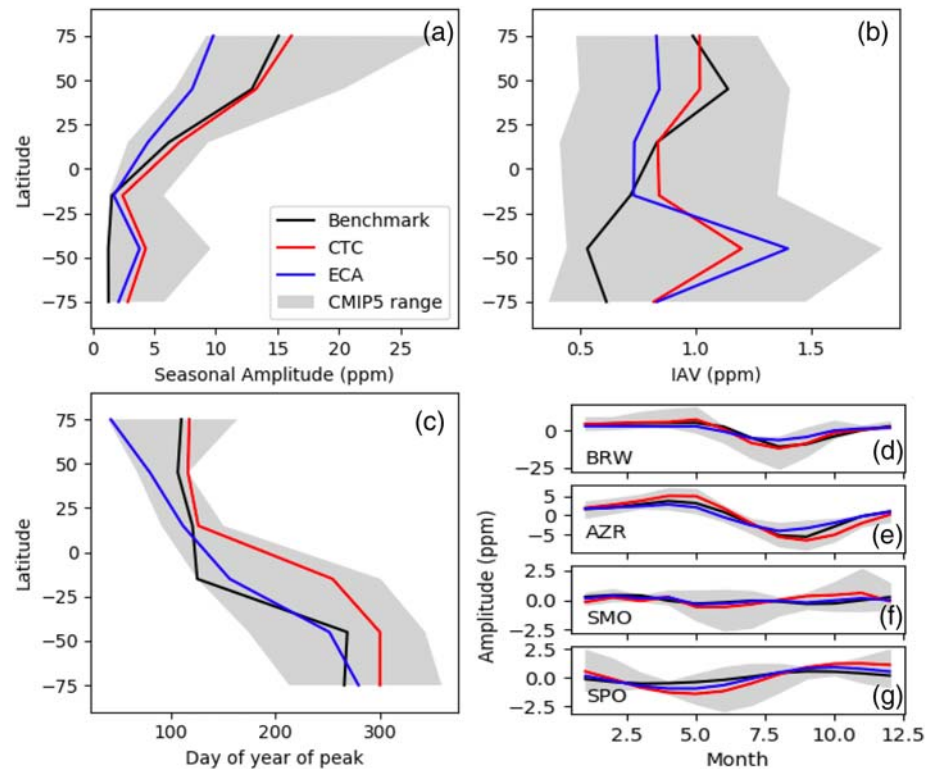


Figure 11. Atmospheric CO₂ concentrations inferred from E3SMv1.1-BGC BDRD-hist land-carbon fluxes (red lines), as compared with in situ flask measurements from NOAA's global Cooperative Air Sampling Network (Conway et al., 1994, gray lines). Subplots show (a) the mean seasonal amplitude over flask sites [ppm], (b) the range of interannual variability [ppm], and (c) the average month-of-year when the peak CO₂ concentration occurs. Observations and measurements are binned within 30° latitude increments; small gray dots indicate individual flask sampling locations. Subplots (d)–(g) show mean seasonal cycles (left) and full time series (right) for four flask sites: (d) Barrow, (e) Azores, (f) Samoa, and (g) South Pole. Methodological details are provided in the supporting information (Text S7).

atmospheric CO₂, that is, inferred CO₂ concentration (details in section 4.4) and global net carbon balance, CTC performs better. CTC also has better scores for biomass, burned area, and LAI.

Regarding hydrology and radiation metrics, both configurations performed better than most CMIP5 models for most variables. The CTC produced better runoff and Terrestrial Water Storage Anomaly predictions and the ECA better predicted evaporative fraction, latent and sensible heat flux, and permafrost extent. Surface upward short-wave and net long-wave radiation were predicted better by CTC, as compared with the ECA.

The ILAMB metrics also evaluate the modeled functional responses of GPP, LAI, and evapotranspiration to climate forcings. These metrics are intended to evaluate whether a model is predicting states and fluxes consistent with observed climate controls. Both the CTC and ECA configurations performed relatively well in these metrics compared to the individual and mean CMIP5 simulations, with the CTC better predicting the functional responses of burned area and the ECA better capturing the functional responses of GPP, evapotranspiration and LAI.

4.4. Observational Benchmarking of Inferred Atmospheric Carbon Dioxide Concentrations

Although the E3SMv1.1-BGC simulations presented in this paper are concentration-driven, ultimately we aim to understand the coupling of carbon fluxes between atmosphere, land, and ocean. As a first step toward this goal, we use a new capability recently implemented within the ILAMB diagnostic package to assess the seasonal and interannual variability of atmospheric CO₂ concentrations that would result from the land model's CO₂ fluxes.

ILAMB combines model-simulated land-atmosphere CO₂ exchange with impulse response functions computed by the reanalysis-driven GEOS-Chem atmospheric transport model to infer the time evolution of CO₂ concentrations at sampling locations. The method is based on approaches described in more detail

by Keppel-Aleks et al. (2014), and uses reanalysis winds from the Modern Era-Retrospective Analysis for Research and Applications data set (Rienecker et al., 2011). The seasonal and interannual variability in detrended CO₂ concentrations inferred by this inversion method are shown in Figure 11 and compared with CO₂ concentrations observed at flask measurement sites in NOAA's global Cooperative Air Sampling Network (<https://www.esrl.noaa.gov/gmd/ccgg/flask.html> Conway et al., 1994).

The diagnostic shown in Figure 11, as currently implemented in the ILAMB software package used to produce this figure, neglects anthropogenic CO₂ sources and the ocean CO₂ sink. Errors from this approximation are expected to be small, since anthropogenic and oceanic fluxes contribute comparatively little to the seasonal and interannual variability in detrended CO₂ concentrations (Keppel-Aleks et al., 2014; Nevison et al., 2008). For example, in the E3SMv1-BGC BDRD simulations (with the default CTC configuration), the seasonal amplitude of ocean NEE is about 0.17 PgC (difference between maximum monthly mean and minimum monthly month) while for land it is over 4 PgC. The interannual variability (calculated as the standard deviation of annual means, 1981–2009) for ocean fluxes is also quite small, about 0.13 PgC/yr, compared with 1.32 PgC/yr for land fluxes. Due to the order-of-magnitude greater seasonal and interannual variability in land fluxes, the errors in detrended CO₂ associated with neglecting ocean fluxes will be small. This diagnostic is therefore interpretable as a first-order approximation of the simulated seasonal cycles in detrended atmospheric CO₂ concentrations that would result from the land carbon fluxes simulated by E3SMv1.

In the CTC configuration, the amplitude of the detrended seasonal cycle in inferred atmospheric CO₂ (Figure 11a) is slightly too large in the Northern Hemisphere, while the ECA model significantly underpredicts the seasonal amplitude. Both configurations exhibit a similar, strong bias relative to observations binned in the region 30–60° south latitude. As with the seasonal amplitude, the interannual variability in the CO₂ time series (Figure 11b) is better simulated in the Northern Hemisphere by the CTC configuration, but is underpredicted by the ECA configuration. Both the CTC and ECA configurations again have a large (positive) bias in the Southern Hemisphere.

The timing of the maximum CO₂ values, that is, the average month during which peak CO₂ concentrations occur, is shown in Figure 11c. Again, the model-observation agreement is much better in the Northern Hemisphere than in the Southern Hemisphere for the model's default (CTC) configuration. The timing of the CO₂ peak is reproduced especially poorly in the tropical region (equator to 23°S). The ECA configuration agrees better with observations on the timing of the peak in the tropics and Southern hemisphere, but less well in middle-to-high northern latitudes, compared with CTC.

Finally, Figures 11d–11g show the mean seasonal cycle and full time series of inferred and measured CO₂ at four selected flask measurement sites: (d) Barrow, Alaska, is a high-latitude site within the Arctic circle; (e) the Azores is a northern midlatitude site located in the middle of the Atlantic ocean, (f) Samoa is located in the Tropical Pacific, and (g) the South Pole.

The overestimated seasonal amplitude in the Southern Hemisphere, which is shown in the averaged statistics in Figure 11a, is also observable in the time series at the South Pole station (Figure 11g). The overall better performance of the CTC configuration on this diagnostic at northern high latitudes is reflected in the seasonal cycle at Barrow (d), and the too-strong Northern Hemisphere seasonal cycle of CTC versus the too-weak cycle of ECA is reflected in the Azores seasonal cycle (e). In the tropics (Figure 11f), both CTC and ECA correctly simulate a weak amplitude to the seasonal cycle; the ECA configuration produces slightly better agreement with the observed timing of the seasonal cycle here. Errors in the tropical region could potentially be related to the complexity of tropical atmospheric dynamics introducing errors and uncertainties in simulation of transport processes, or to the occurrence of drought and drought responses.

The challenges in attaining model-observation agreement in the inferred CO₂ for the Southern Hemisphere are likely mostly due to the greater importance of the ocean sink in determining the seasonal cycle at the Southern Hemisphere measurement sites (Nevison et al., 2008), which are not accounted for in this method. Additionally, there are inherent difficulties in simulating interhemispheric exchanges of air, which result in large differences in the simulated interhemispheric gradient of CO₂ when using different atmospheric transport models (Gurney et al., 2003; Law et al., 1996). In particular, the interhemispheric transport of CO₂ has been shown to be sensitive to the covariance between the seasonality of CO₂ surface fluxes and interhemispheric air exchange (Dargaville et al., 2003), while differences in the strength of simulated convective air

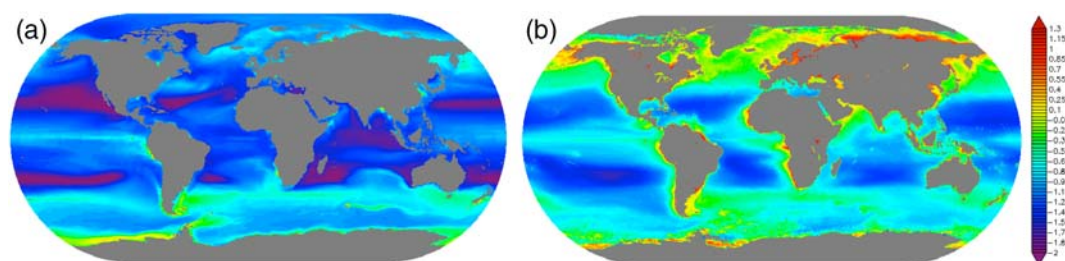


Figure 12. log(Ocean surface chlorophyll-a) (mg/m^3) (a) averaged over the final 30 years of BDRD and (b) averaged over 1997–2010 from SeaWiFS satellite observations.

transport strongly influence the simulation of CO_2 accumulation near continental source regions, relative to its transport to remote marine air.

While the results presented in Figure 11 were calculated using reanalysis-driven GEOS-Chem inversions, future efforts will be required to characterize the transport properties of the E3SMv1.1 atmosphere model. We note that atmospheric transport in E3SMv1.1 likely has significant differences from its ancestor, CESM, due to such modifications as an increase from 30 to 72 vertical layers, and the replacement of the convection parameterization.

4.5. Observational Benchmarking of Ocean and Sea Ice Biogeochemistry

Next, we compare the simulated ocean and sea ice biogeochemistry with observational benchmarks. Figure 12 shows the total surface chlorophyll concentration summed over all phytoplankton functional groups from BDRD-hist compared to Sea-Viewing Wide Field-of-View Sensor (SeaWiFS) satellite observations. The modeled chlorophyll has a large low bias throughout most of the global ocean, indicating that the model's production of biomass is biased low almost everywhere. The strong low bias in coastal and eastern basin upwelling regions is a common feature of coarse-resolution ocean biogeochemical models, since underresolved ocean dynamics create inherent challenges in simulating nutrient transport and other coastal processes. In addition, some processes known to be important in coastal ecosystems, such as sedimentation and resuspension of particulates, are currently not represented in the model.

However, the model's most prominent bias is its deficit in chlorophyll north of 35°N . Surface nitrate (Figure 13) and phosphate concentrations (not shown) are very low in this area compared to climatological data, strongly limiting phytoplankton growth. This depletion of surface nutrients is likely the result of a too-shallow mixed layer, caused by the cold and fresh bias of the North Atlantic (Figure 9), which can prevent the replenishment of nutrient stocks via deep vertical mixing. In addition, the sluggish meridional overturning strongly curtails the effectiveness of deep “nutrient streams” (Williams et al., 2011) in replenishing nutrient stocks even when deep mixing does occur.

Another notable bias is the extensive regions of the global ocean that are phosphate-limited (supporting information, Figure S12). However, the concentrations of other macronutrients are also scant in most of these areas, so all are effectively limiting where chlorophyll is low. On the other hand, the model realistically captures the presence of large iron-limited regions in much of the Southern Ocean (supporting information, Figure S12).

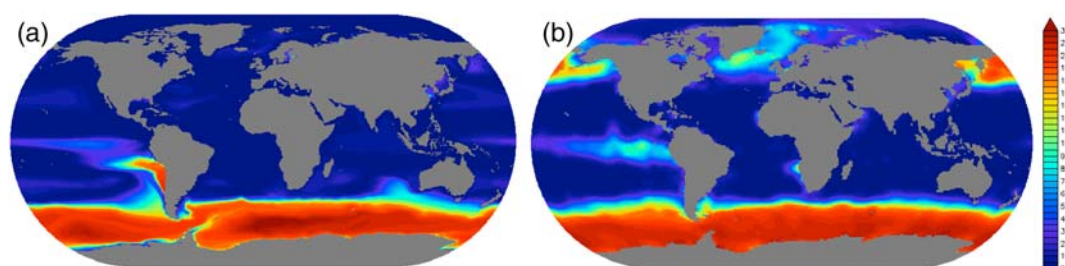


Figure 13. Ocean surface nitrate (mmol/m^3) (a) averaged over the final 30 years of BDRD and (b) World Ocean Atlas climatology (Boyer et al., 2013).

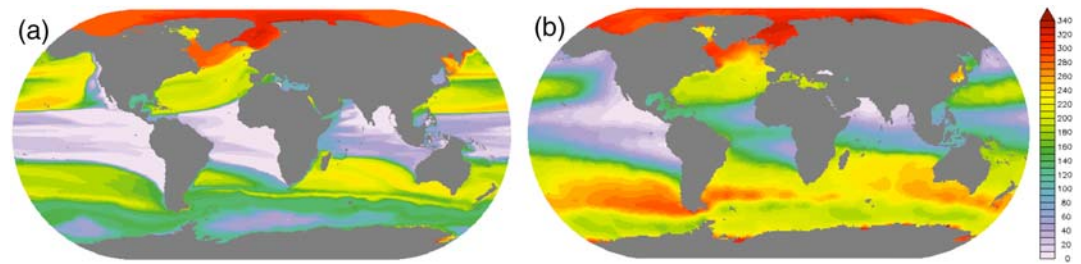


Figure 14. Ocean dissolved oxygen at 500-m depth (mmol/m^3) (a) averaged over the final 30 years of BDRD and (b) World Ocean Atlas climatology (Boyer et al., 2013).

An example of the interplay of physical and biogeochemical biases can be seen in the extent of the subsurface oxygen minimum zones (OMZs, Figure 14). Below the photic zone, oxygen is required for the heterotrophic bacterial processes that mediate remineralization of organic nutrient pools. Achieving a realistic simulation of OMZs has proven to be a challenge for ESMs due to a delicate balance between physics and chemistry, and E3SMv1.1-BGC is no exception. Overall, the OMZ bias of substantially overestimating the amount of low-oxygen water is very similar to CESM1 (Moore et al., 2013), though even larger here. According to the World Ocean Atlas estimate (Boyer et al., 2013), the volume of OMZs in the global ocean (defined by oxygen levels $<20 \text{ mmol/m}^3$) should be about $13 \times 10^6 \text{ km}^3$, compared to $38 \times 10^6 \text{ km}^3$ in CESM1 and $82 \times 10^6 \text{ km}^3$ here. In addition, the model's tropical Atlantic has extensive regions of hypoxia, which are rare in reality.

As noted in section 4.6.1, the net flux of CO_2 from the ocean to the atmosphere is relatively weak, though the distribution in BDRD is quite realistic since it is strongly related to SST and circulation, with ocean outgassing in the low latitudes and in the Antarctic Circumpolar Current, and uptake occurring in the midlatitudes and high northern latitudes (Figure 15). The high outgassing seen in the Southern Ocean is partly due to a relatively low mean sea ice concentration, especially to the east of the Weddell Sea. As seen in Table 5, the net transfer of CO_2 into the ocean is 1.2 PgC/yr averaged over the final 30 years of BDRD, while the estimate of Landschützer et al. (2017) is 1.4 PgC/yr .

Sea ice algal production in the Arctic Ocean is tightly constrained by extensive low surface ocean nitrate and silicate biases in all simulations. This leads to significant underestimations of Arctic ice primary production: CNST-forcing simulations range from $5.5\text{--}7 \text{ TgC/yr}$; RD-hist values peak at 8.5 TgC/yr in the early 1980s before decreasing to CNST-forcing values of 6 TgC/yr by the end of the historical period; and RC-hist runs fluctuate between $9\text{--}10.5 \text{ TgC/y}$ over the last 20 years of the historical period. Increases relative to CNST-forcing in all historical simulations are in large part due to increases in sea ice extent. By contrast, estimates of total Arctic ice algal primary production range from $23\text{--}170 \text{ TgC/yr}$ (Arrigo, 2014).

What is perhaps surprising is the relatively good agreement between total ice algal chlorophyll concentrations in CNST-forcing and historical simulations and field observations (Figure 16). In particular, modelled results show good agreement in the key Arctic primary production regions of the Bering Sea and the waters north of Point Barrow, though we do see substantial overestimations in the Beaufort Sea simulations in early spring. It is important to note that comparable chlorophyll with very low production is achieved by limiting carbon turnover: algal mortality and loss to the ocean during meltwater flushing are minimized. In reality, we expect at least an order of magnitude greater carbon cycling in Arctic sea ice. Comparisons of historical

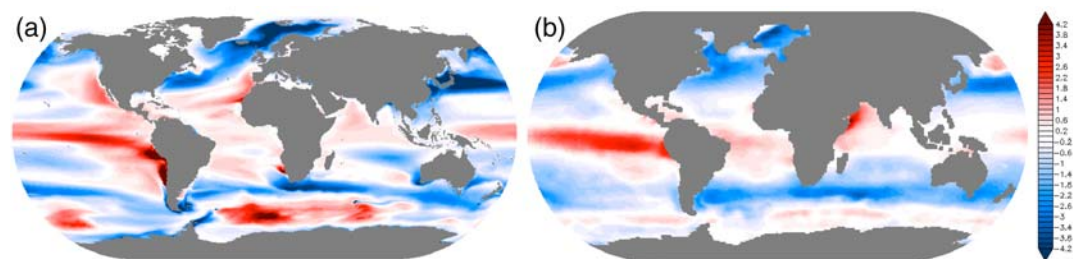


Figure 15. CO_2 flux from ocean to atmosphere ($\text{mmol/m}^2/\text{yr}$). (a) averaged over the final 30 years of BDRD. (b) Landschützer climatology (Landschützer et al., 2017).

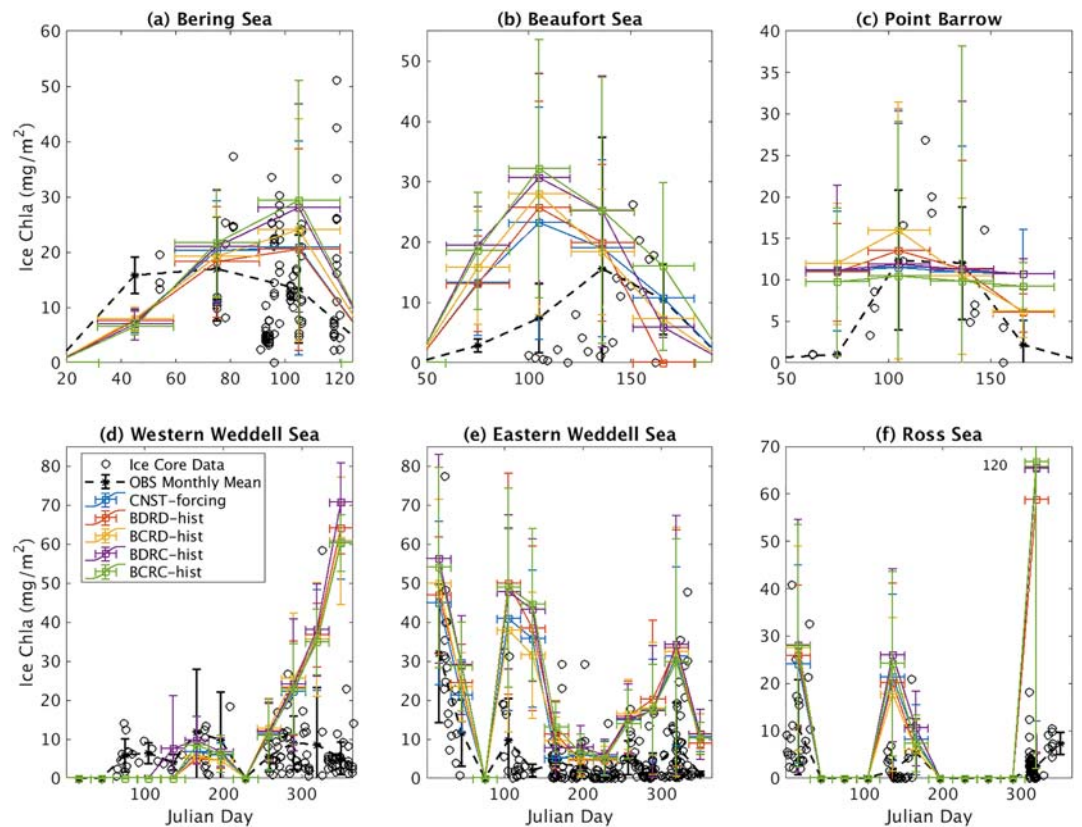


Figure 16. Comparison of simulated sea ice chlorophyll concentrations in historical and CNST-forcing runs (colored solid lines; vertical error bars indicate 1 standard deviation; horizontal bars indicate averaging window; mg/m^2) versus in situ ice core measurements ($^{\circ}$). Monthly mean of observations is also plotted with standard deviations (dashed line). Simulated curves are 20-year monthly means from 1986–2006. Observations are from (a) Gradinger et al. (2012); (b) Horner and Schrader (1982), and Alou-Font et al. (2013); (c) Lee et al. (2008) and C. Deal (personal communication, 2002); and (d)–(f) Meiners (2013).

and CNST-forcing ice integrated chlorophyll in the three Arctic locations (Figures 16a–16c) do not reveal a consistent pattern except, perhaps, for clustering of RD and RC tendencies.

Simulations of Southern Ocean ice primary production are generally limited by light, not nutrients, and so less affected by biases in upper ocean nutrient concentrations. Simulated total annual primary production is low but within the wide 3.6–456 TgC/yr range of previous estimates (Arrigo, 2014): CNST-forcing simulations are 14–16 TgC/yr; radiatively forced (BDRD-hist, BCRD-hist) values are slightly lower, spanning 12.5–15 TgC/yr in the last 20 years of the historical period; while biogeochemically forced (BDRC-hist, BDRD-hist) are slightly higher (15–17.5 TgC/yr). When normalized by sea ice extent, all historical simulations show decreases in annual primary production from a CNST-forcing value of 1,350 $\text{mgC}/\text{m}^2/\text{yr}$ to a 20-year historical mean of 1,150 $\text{mgC}/\text{m}^2/\text{yr}$.

Ice chlorophyll estimates in the Southern Ocean (Figures 16d to 16f) compare well with in situ core observations in the western Weddell Sea (-60°E to -45°E), eastern Weddell Sea (-45°E to 30°E), and the Ross Sea (160 to 210°E), although simulations tend to overestimate chlorophyll concentrations in the austral summer. This suggests that algal retention mechanisms (slow rates of desorption from the ice crystal and high algal motility rates that allow diatoms to remain in the sea ice under slower rates of ice melt) are likely too effective. As in the Arctic analysis, there are no consistent patterns in historical and CNST-forcing chlorophyll time series for the three regions investigated.

4.6. Observational Benchmarking of Global Carbon and Nutrient Budgets

To assess the model's ability to correctly represent carbon and nutrient inventories, we examine the 30-year mean global budgets of land carbon and nutrient pools and fluxes simulated by the CTC and ECA

Table 4
Land Carbon Budget Terms in [PgC] for Pools or [PgC/yr] for Fluxes

	CTC		ECA		Observations
	CNST-forcing	BDRD	CNST-forcing	BDRD	
Total ecosystem carbon	2,530	2,470	1,970	1,990	
Total vegetation carbon	648	589	416	383	450–650 (IPCC AR5), 455 (GEOCARBON), 550 ± 100 from 1980s to 1990s (Houghton, 2003) 560 ± 94 from 1982 to 1990 (DeFries et al., 1999)
Total SOM carbon	1,747	1,758	1,247	1,278	1,500–2,400 (IPCC AR5), 1,750 ± 250 (Jobbgy & Jackson, 2001), 2,376–2,456 (Batjes, 1996), 3,000 (Köchy et al., 2015)
Total SOM carbon (top 1 m)	1,095	1,106	1,024	1,054	890–1660 (Todd-Brown et al., 2013), 1462–1548 for the last 20–30 years (Batjes, 2014), 1,325 (Köchy et al., 2015)
Total litter carbon	21	23	37	44	68 (Matthews, 1997), 43 ± 3 from 1990 to 2007 (Pan et al., 2011)
Coarse woody debris carbon	110	101	288	269	75 (Matthews, 1997), 43 ± 3 from 1990 to 2007 (Pan et al., 2011)
Product 10 carbon	0	2.9	0	3.4	
Product 100 carbon	0	2.9	0	4.6	
Total product carbon	0	5.8	0	8.0	
GPP	109	124	91	108	123 ± 8 from 1998 to 2005 (Beer et al., 2010), 119 ± 6 from 1982 to 2008 (Jung et al., 2011), 123 from 1998 to 2005 (IPCC AR5), 150–175 from 1980s to 2010 (Welp et al., 2011), 140 (for year 2007 Joiner et al., 2018), 125 ± 25 PgC/yr from 2001 to 2011 (Jiang & Ryu, 2016)
Autotrophic respiration	68	79	49	59	
Litter fall	45	48	62	63	
Litter to soil	20	21	12	14	
Heterotrophic respiration	37	39	38	41	
Fire loss from vegetation and litter	4.6	4.8	4.2	4.4	
Anthropogenic disturbance	0	0.55	0	0.72	
Product decomposition	0	0.72	0	0.88	
Harvest to product	0	0.65	0	0.83	
LULCC to product	0	0.11	0	0.10	

Note. Methodological details are provided in the supporting information (Text S5).

configurations. We also briefly discuss the carbon pools and fluxes simulated by the ocean model, while noting that these are impacted by the biases described in section 5.1.

For all terms, we compare the preindustrial (1977–2014 from CNST-forcing) and present day (1977–2014 from BDRD-hist). Methodological details of the model budget calculations are provided in the supporting information (Text S5).

4.6.1. Observational Benchmarking of Global Land and Ocean Carbon Cycle Budgets

The mean budgets of land carbon pools and fluxes for the years 1977–2006 from CNST-forcing and BDRD (CTC and ECA) are shown in Table 4, together with a summary of observational estimates for some terms. The values for CNST-forcing represent the preindustrial equilibrium state, while the values for BDRD represent the contemporary state. Most of the observational estimates represent contemporary conditions, but note that mismatches between the years for which specific observational estimates are valid and the simulation years that have been averaged for this comparison are an important caveat to consider when comparing these values. Nevertheless, it is useful to place the global budgets in context with previous observational estimates and we discuss these comparisons in this section.

As discussed previously (section 5.1 and Figure 17), model-simulated TEC declines over the historical period due to LULCC and these declines are greater in ECA simulations due to stronger phosphorus limitation in ECA. Toward the end of the twentieth century, stronger CO₂ fertilization leads to recovery of TEC, producing

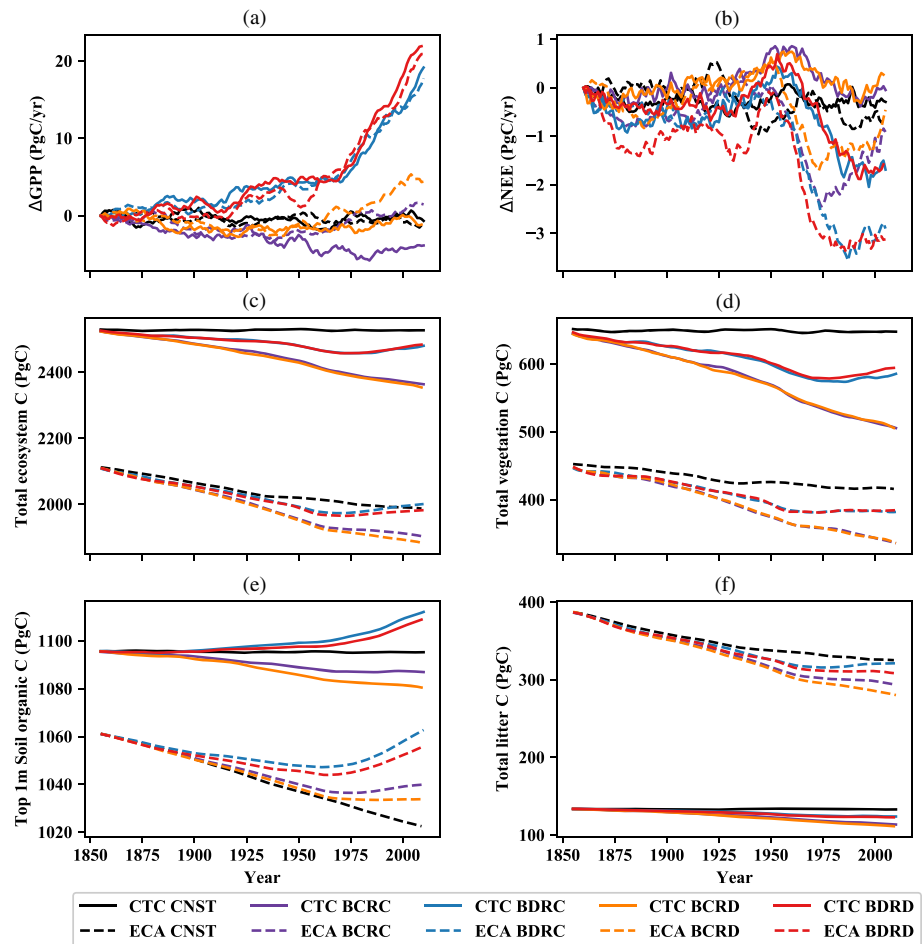


Figure 17. Time series of global annual totals for (a) GPP [PgC/yr], (b) NEE [PgC/yr], (c) total land ecosystem carbon (as anomaly from 1850; PgC), (d) total vegetation carbon (as anomaly from 1850; PgC), (e) total SOM carbon in the top 1 m (as anomaly from 1850; PgC), and (f) total litter carbon including coarse woody debris (as anomaly from 1850; PgC). All panels show 10-year running mean values between 1850–2014, with CTC simulations shown as solid lines and ECA as dashed lines. Note that the same results are shown again in the supporting information either as anomalies (GPP and NEE; a and b), or as absolute values (carbon pools; c–f).

a simulated total carbon stock in the contemporary period that is larger in CTC (2,470 PgC) than in ECA (1,990 PgC).

The two model configurations also partition carbon differently among the various ecosystem pools. For CTC, 24% of the terrestrial carbon is stored in vegetation (589 PgC), 5% in litter and coarse wood debris (124 PgC), and 71% in SOM (1,758 PgC). For ECA, about 19% of the terrestrial carbon is stored in vegetation (383 PgC), 16% in litter and coarse wood debris (313 PgC), and 64% in SOM (1,278 PgC). Soil carbon stocks were similar between the two configurations in the top 1 m of soil, while CTC had significantly more deep-soil carbon than ECA. Such differences in deep soil carbon stocks may generate different carbon-climate feedbacks under future warming scenarios that include high-latitude thawing (Pries et al., 2017).

For vegetation carbon, the CTC simulation (589 PgC) is within the range of the inventory-based estimates from the Fifth Assessment Report of the United Nations Intergovernmental Panel on Climate Change (IPCC AR5) (450–650 PgC Ciais et al., 2013) and moderately higher than the most recent global observational estimates (380–536 PgC Erb et al., 2018), which include subsequent reductions in vegetation carbon due to deforestation and other land management activities (2006 to ca. 2018). The ECA-simulated vegetation carbon (383 PgC) is lower than the IPCC AR5 estimate, but at the lower end of the range presented in Erb et al. (2018).

Table 5
Ocean Carbon Budget Terms in [PgC] for Pools or [PgC/yr] for Fluxes Calculated From the Final 30 Years of BDRD

Ocean Pool or Flux	Magnitude [PgC] or [PgC/yr]
Total DIC	36,884
Total DOC	14.2
Total biotic carbon	0.4
Primary production	36.2
Remineralization	
POC to DIC	7.8
DOC to DIC	6.5
Carbonate to DIC	0.6
Grazing, mortality, aggregation	
Biota to DIC	21.9
Biota to DOC	6.3
Biota to POC	7.9
Flux from atmosphere	1.2
Flux from sea ice	0.01
Flux from rivers	0.4
Export at 100 m	3.7
Burial	0.1

Note. Fluxes are positive into the ocean and carbon:nitrogen:phosphorus ratios for most pools and fluxes follow the model's value of the Redfield ratio, 117:16:1.

Global SOM carbon estimates are currently uncertain but better constrained for the top 1 m of soil than for deep soil (i.e., 1–3 m). For SOM carbon in the top 1 m of soils, both CTC- and ECA-simulated values are within the range of estimates reported by Todd-Brown et al. (2013) (890–1,660 PgC), but lower than some other observationally based estimates (1462–1,548 PgC, Batjes, 1996; 1,325 PgC, Köchy et al., 2015). CTC-simulated 0–3 m depth interval SOM carbon is within the range of estimates reviewed in the IPCC AR5 report (1,500–2,400 PgC Ciais et al., 2013) and in Jobbgy and Jackson (2001) (1,750 ± 250 PgC), while ECA-simulated soil carbon is below the range of those estimates. Both CTC and ECA simulate less 0–3 m SOM carbon than is suggested by some other recent observational estimates (2,376–2,456 PgC, Batjes, 1996; 3,000 PgC, Köchy et al., 2015). This large range in observationally inferred global SOM carbon stocks indicates more observational data is needed to better constrain global carbon cycling models.

For total litter carbon, observational estimates range from 43 ± 3 for forests (Pan et al., 2011), to a global estimate of 68 PgC (Matthews, 1997). The CTC configuration simulates lower litter carbon than these estimates (23 PgC), while ECA-simulated litter carbon is comparable to the lower estimate (44 PgC). Both CTC and ECA simulate a larger coarse woody debris carbon stock (101 PgC for CTC and 269 PgC for ECA) than is supported by observation-based estimates, which range from 73 ± 6 (forests Pan et al., 2011) to 75 PgC (Matthews, 1997).

For GPP, the CTC-simulated value of 124 PgC/yr is comparable to several observationally based estimates: 123 ± 8 PgC/yr (years: 1998–2005 Beer et al., 2010), 119 ± 6 PgC/yr (years: 1982–2008 Jung et al., 2011) and 123 PgC/yr (Ciais et al., 2013). It is lower than the range of 150–175 PgC/yr that was estimated by Welp et al. (2011) based on the oxygen isotopes of atmospheric CO₂ (years: 1977–2009). Another recent study based on satellite data suggested a global GPP of 140 PgC/yr for the year 2007 (Joiner et al., 2018). ECA-simulated GPP is generally lower than these observational values, but is within the uncertainty range of a more recent remote-sensing-driven estimate: 122 ± 25 PgC/yr (years: 2000–2015 Jiang & Ryu, 2016).

Analogous to the land results, 30-year means of the simulated ocean carbon pools and fluxes are shown in Table 5. Note that the carbon:nitrogen:phosphorus ratios for most pools and fluxes in the ocean and sea ice follow the model's Redfield ratio, and so we do not repeat the figures for nitrogen and phosphorus.

Table 6
Nitrogen Budget Terms in [PgN] for Pools or [PgN/yr] for Fluxes

	CTC		ECA		Observations
	CNST-forcing	BDRD	CNST-forcing	BDRD	
Vegetation	4.3	4.3	2.6	2.7	Model estimates: 3.8 (Zaehle et al., 2010), 5.3 (Xu-Ri & Prentice, 2008), 16 (Lin et al., 2000), 18 (Yang et al., 2009)
Litter	0.61	0.64	1.72	1.78	
Soil organic nitrogen	174	175	113	116	Top 1 m: 95 PgN (Post et al., 1985), 133–140 PgN (Batjes, 1996)
Product	0	0.01	0	0.01	
Soil mineral nitrogen	0.68	0.76	2.7	2.8	
Vegetation to litter	0.62	0.69	0.55	0.65	
Litter to soil	0.62	0.68	0.54	0.63	
Biological nitrogen fixation	0.086	0.087	0.12	0.18	0.195 1990s (Cleveland et al., 1999); Preindustrial estimates: 0.108 (Galloway et al., 2014); Preindustrial estimates 0.058 (Vitousek et al., 2013)
Plant nitrogen uptake	0.66	0.75	0.52	0.61	
Nitrogen deposition	0.019	0.064	0.019	0.064	
Net nitrogen mineralization	0.62	0.65	0.55	0.58	
Leaching from mineral nitrogen pool	0.00069	0.00088	0.0033	0.0047	
Leaching from land	0.0079	0.012	0.0085	0.012	
Anthropogenic disturbance	0	0.0075	0	0.011	
Product decomposition	0	0.0014	0	0.0020	
Harvest	0	0.0013	0	0.0018	
N ₂ O gas	0.0021	0.0021	0.0068	0.0083	
LULCC to product	0	0.00022	0	0.0040	

Note. Methodological details are provided in the supporting information (Text S5).

We find that the model-simulated ocean carbon uptake in E3SMv1.1 (which includes effects of sea ice coupling) is slightly below the low end of data-based estimates. For example, observational studies summarized in the IPCC AR5 (Ciais et al., 2013) estimated the ocean carbon sink to be in the range 2.0 ± 0.7 PgC/yr for the 1980s and 2.2 ± 0.7 PgC/yr for the 1990s, compared with 1.1 PgC/yr for the 1980s and 1.3 PgC/yr for the 1990s in the E3SMv1.1 BDRD-hist simulations.

Although we did not directly simulate a separate anthropogenic carbon pool, we can estimate it by differencing the BDRD and BCRD cases. The total ocean uptake of anthropogenic carbon since 1850 is estimated to be 150 ± 20 PgC/yr (Le Quéré et al., 2018), compared to ~ 93 PgC/yr for E3SM, further confirming the model's relatively weak air-sea transfer.

This underprediction of the ocean carbon sink is likely related to the lack of Redi mixing, though the incomplete spin-up of the ocean biogeochemical state also plays a role. We document these biases here as they represent an important development milestone for the E3SM biogeochemistry, and we note that the biases are sufficiently large that the ocean biogeochemical outputs from E3SMv1.1-BGC should not be used for scientific purposes. Efforts are currently underway to understand and address the issues causing these biases, and we expect to be able to document improvements in the ocean biogeochemistry in future versions of E3SM.

4.6.2. Observational Benchmarking of Global Land Nitrogen Cycle Budgets

Overall, fewer observational estimates are available for nitrogen pools and fluxes compared to carbon, so the evaluation of the global nitrogen cycle is necessarily more limited. As done previously in the evaluation of global carbon pools, we compare observational benchmarks with the mean values from the period 1977–2014 of the BDRD simulation (Table 6), noting again that discrepancies between the years referred to by the observations and the simulations are a limitation in this analysis.

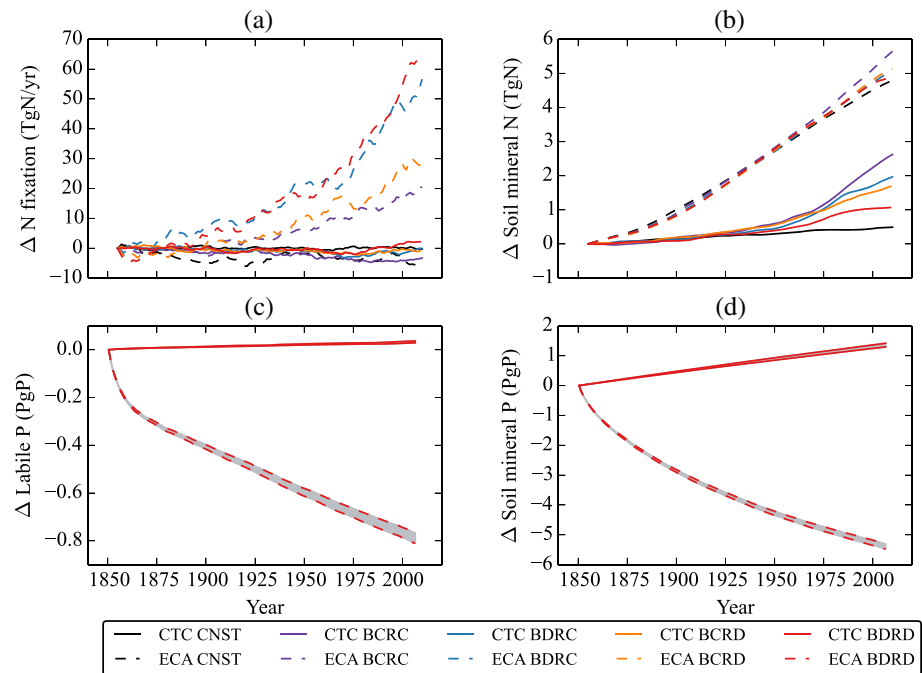


Figure 18. Time series of globally integrated pools and global mean fluxes, as anomalies from their respective 1850 values: (a) nitrogen fixation to soil mineral nitrogen (TgN/yr), (b) total soil mineral nitrogen (TgN), (c) labile phosphorus in top 40–60 cm (TgP), (d) soil mineral phosphorus in top 40–60 cm (TgP), (e) gross nitrogen mineralization (TgN/yr), and (f) net phosphorus mineralization (TgP/yr).

The models simulate vegetation nitrogen stocks of 4.3 PgN (CTC) and 2.7 PgN (ECA), compared to the range of 3.8–18 PgN estimated in previous modeling studies (Lin et al., 2000; Xu-Ri & Prentice, 2008; Yang et al., 2009; Zaehle et al., 2010).

Observationally based estimates for soil organic nitrogen in the top 1 m of soil range from 95 PgN (Post et al., 1985) to 133–140 PgN (Batjes, 1996). Model-simulated soil organic nitrogen for the full soil column is moderately larger than observational estimates for the top 1 m of soil in CTC (175 PgN) and within the observed range for ECA (116 PgN). This comparison provides some confidence that the model simulations of global nitrogen pools are likely within the range of values supportable by observations.

Biological nitrogen fixation during the preindustrial period was estimated at 0.058 PgN/yr by Vitousek et al. (2013) and 0.108 PgN by Galloway et al. (2014). E3SM simulates levels of biological fixation that are comparable to these estimates, at 0.087 PgN/yr and 0.18 PgN/yr for CTC and ECA, respectively. Over the historical period, nitrogen fixation increased slightly (~1 TgN) for CTC while it increased significantly (~60 TgN, 50%) for ECA (also shown in Figure 18a).

4.6.3. Observational Benchmarking of Global Land Phosphorus Cycle Budgets

Very few observations of ecosystem phosphorus are available on a global scale, limiting the ability to assess whether model behaviors are realistic for phosphorus cycling. In the absence of observational constraints, we compare our results with previous modeling studies (Table 7). Model-simulated vegetation phosphorus is 0.36 PgP for CTC and 0.24 PgP for ECA, comparable to the estimates from previous modeling studies, which range from 0.23 to 3 PgP (Goll et al., 2012; Jahnke, 1992; Wang et al., 2010a). Model-simulated soil organic phosphorus is 3.50 PgP for CTC and 1.12 PgP for ECA, which for both configurations is lower than values from previous studies, ranging from 5 to 10 PgP (Goll et al., 2012; Smil, 2000; Yang et al., 2013).

As discussed in section 5.3 and detailed in Appendix C3, initialization of phosphorus, and the evolution of phosphorus limitation over the course of the historical simulations, is among the key aspects that distinguishes the CTC and ECA simulations presented in this paper. Currently, the only observationally based global gridded soil phosphorus product is the global map that was used to initialize these simulations (Yang et al., 2013). Because this data set relied on observations of only the top 50 cm, we evaluate the model-simulated soil mineral phosphorus for the top 40 cm and top 60 cm (Table 7). We find that for the

Table 7
Phosphorus Budget Terms in [PgP] for Pools or [TgP/yr] for Fluxes

	CTC		ECA		Observations
	CNST-forcing	BDRD	CNST-forcing	BDRD	
Vegetation	0.37	0.36	0.23	0.24	Model estimates: 0.23–3 PgP (Jahnke, 1992; Smil, 2000; Wang et al., 2010a)
Litter	0.07	0.07	0.15	0.15	
Soil organic phosphorus	3.48	3.50	1.07	1.12	
Product	0	0.0019	0	0.00051	
Soil mineral phosphorus	270	270	30	30	
Soil mineral phosphorus (40cm)	65	65	30	30	
Soil mineral phosphorus (60cm)	88	88	31	31	
Vegetation to litter flux	41	45	51.2	59.6	
Litter to soil flux	41	44	55	62	
Plant phosphorus uptake	37	42	54	63	
Weathering	1.7	1.7	28.7	28.5	
Adsorption	414	412	45	45	
Desorption	415	415	26	26	
Occlusion	1.9	1.9	0.12	0.12	
Net phosphorus mineralization	34	37	48	54	
Gross phosphorus mineralization	52	55	66	73	
Immobilization	18	18	17	18	
Biochemical mineralization	0.04	0.11	0.34	0.45	
Leaching from land	0.40	0.38	12.11	11.29	
Anthropogenic disturbance	0	0.94	0	1.02	
Product decomposition	0	0.24	0	0.12	
Harvest	0	0.22	0	0.10	
LULCC to product	0	0.04	0	0.02	

Note. Methodological details are provided in the supporting information (Text S5).

contemporary period, the simulated global phosphorus pool in the top 40–60 cm of soil are comparable to the observationally based estimate of 45 PgP (Yang et al., 2013) in both model configurations. The two configurations differ significantly in their choices regarding the vertical distribution of mineral phosphorus below 50 cm, but additional observations in different parts of the world are needed to better constrain the present-day vertical distribution of phosphorus.

5. Ecosystem Responses to Prescribed Historical Increases in CO₂ in the Default and Alternative Land Biogeochemistry Configurations

5.1. Time Evolution of Global Land Biogeochemistry Metrics in CTC and ECA Configurations

We now turn to a more detailed analysis of the biogeochemical responses to prescribed historical increases in radiatively coupled and biogeochemically coupled CO₂, in both the default CTC configuration and alternative ECA configuration of the land biogeochemistry. Figure 17 provides an overview of the temporal evolution of several critical metrics of land biogeochemistry in response to the four different CO₂ coupling scenarios.

First, we consider the behavior of the CNST-forcing simulations, focusing initially on establishing whether any drifts in overall behavior emerge in the default CTC configuration of E3SMv1.1-BGC. For all biogeochemical metrics, the global mean values are stable throughout the CNST-forcing simulation. In particular, over the full CNST-forcing simulation (1850–2014), mean NEE was 0.031 PgC/yr in the E3SMv1.1-BGC (default configuration), indicating that the carbon cycle is well-equilibrated. Some small trends appear (e.g., a slight increase in total soil carbon), but these are small enough that we did not make any corrections for them in analyzing the simulations.

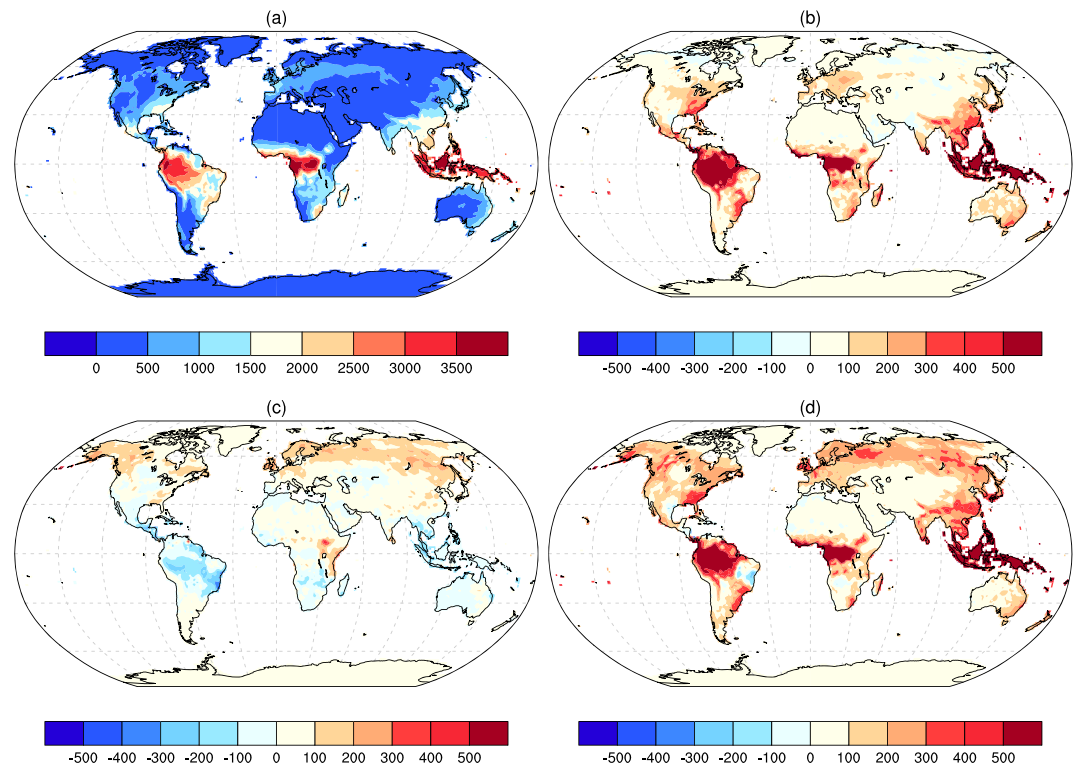


Figure 19. Spatial pattern of annual GPP in E3SMv1.1-BGC simulations, and its response to historical CO₂ coupling scenarios: (a) BCRC-hist, (b) physiological effect: BDRD-hist – BCRC-hist, (c) radiative effect: BCRD-hist – BCRC-hist, and (d) full effect: BDRD-hist – BCRC-hist.

In the ECA CNST-forcing simulation, GPP and NEE remained stable, but trends emerged in the metrics of ecosystem carbon pools. In the ECA configuration, soil phosphorus pools were fixed at constant values during spin-up, and then allowed to evolve during the simulation period. Consequently, the ECA CNST-forcing simulation, by design, depletes phosphorus from soils during the historical period; the trends in the ECA CNST-forcing carbon pools are consequences of this increasing phosphorus limitation. These interactions will be discussed in more detail below, as well as in section 5.3.

We now turn to a more detailed discussion of the individual panels in Figure 17. GPP is stable over the course of the simulations at ~110 PgC for the CNST-forcing simulation of CTC and 92 PgC for ECA (Figure 17a). A strong CO₂ fertilization effect on GPP is evident, with BD simulations exhibiting much stronger growth in GPP compared to BC simulations. Additionally, in the late twentieth century, a response of GPP to CO₂-driven warming begins to appear, with higher productivity in the RD simulations than in the RC simulations, in both biogeochemistry configurations. Similarly, in the CTC configuration, the BCRC-hist simulation exhibits slightly lower GPP than the CNST-forcing, likely due to the cooler climate in the BCRC-hist. This is explored further by examining the geographic patterns of these effects in section 5.2 (Figure 19).

The temporal evolution of NEE is shown in Figure 17b. The slightly positive average values of NEE until the midtwentieth century reflect the net effects of a carbon source associated with LULCC, which exceeded the magnitude of the net carbon sink associated with CO₂ and nitrogen deposition fertilization of plant growth, consistent with observational estimates (Le Quéré et al., 2018). Aerosol-induced cooling may also act to reduce the land carbon sink during the historical period (Zhang et al., 2019), but we are unable to disentangle this effect from CO₂ effects in the simulations. In the late twentieth century, NEE becomes negative in BD simulations, as the land responds to increasing atmospheric CO₂ concentrations by increasing its uptake of CO₂.

Figure 17c shows the evolution of TEC, which reflects the cumulative effect of land-atmosphere carbon exchanges. While stable in the CNST-forcing simulation of CTC, TEC decreases in the CTC BCRC historical

simulation due to LULCC, as harvesting and deforestation move carbon from land ecosystems to the atmosphere. The CNST-forcing ECA simulation shows a nearly linear decline in TEC, the result of losses of ecosystem phosphorus. Further discussion of the nutrient limitation effects in the two model configurations is provided in section 5.3.

When the historical simulations are compared to CNST-forcing, the TEC in both the CTC and ECA simulations exhibits the expected responses to CO₂ biogeochemical coupling (BD) and radiative coupling (RD) (although in ECA simulations, these responses are superimposed on top of the overall declining trend). TEC is significantly higher for biogeochemically coupled (BD) cases, reflecting the accumulation of carbon under the influence of CO₂ fertilization of plant growth. For both CTC and ECA, TEC is slightly lower for BCRD than BCRC, indicating that radiatively forced climate change through the historical period is driving a small carbon release from land.

In the fully coupled historical simulations (BDRD-hist), the time evolution of TEC in BDRD simulations exhibits a U-shaped behavior, declining in the early years of the twentieth century and then increasing. A similar pattern was exhibited by some of the CMIP5 models and is supported by observationally derived reconstructions of historical carbon storage (Hoffman et al., 2014; Khatiwala et al., 2013). In the CTC BDRD simulation, TEC declines by a total of about 50 PgC over the period 1850–1950, in good agreement with the observationally based estimate of Khatiwala et al. (2013), which has an uncertainty range of about 10–50 PgC/yr in 1950. In the CTC simulation, TEC declines further until about the year 1975, with a peak change of about 80 PgC, before increasing again. This is a somewhat greater loss over the 1850–1975 period than is supported by the Khatiwala et al. (2013) estimate of about 0–50 PgC, but is within the range of the Khatiwala et al. (2013) estimate for the 1765–1975 period (~30–80 PgC). By the year 2008, the TEC recovers to about 50 PgC below its 1850 value in the CTC simulation, which is slightly less than the 1850–2008 loss of ~–40 to 40 PgC estimated by Khatiwala et al. (2013), but within the 1765–2008 estimate of ~–10 to 70 PgC.

Le Quéré et al. (2018) reviewed and compiled and summarized various estimates of historical carbon emissions and uptake, as well as the estimated partitioning of carbon uptake among land, ocean, and atmosphere. Based on their review, they reported an estimated cumulative 1850–2014 carbon source associated with LULCC of 195 ± 75 PgC, and a cumulative carbon sink from land ecosystem uptake over this time period of 185 ± 50 PgC. This equates to an estimated net TEC loss of 10 PgC, but with a large uncertainty range of at least 50 PgC, which encompasses the CTC BDRD simulation's total net carbon loss over the same period.

By comparison, the ECA BDRD simulation loses nearly 150 PgC by 1975 before it begins to gain TEC again, ending with a net loss of about 130 PgC over the entire period 1850–2014. This constitutes a greater loss of carbon from land than is suggested by either observational estimates (discussed above), or the CMIP5 models Hoffman et al. (2014).

There is some evidence of potential nonlinear interactions between the radiative and biogeochemical coupling in CTC simulations: the BDRD simulation has a TEC almost identical to BDRD, while a small radiative response is observed when comparing the BCRD and BCRC simulations. We hypothesize that progressive nutrient limitation occurs under CO₂ fertilization (Luo et al., 2004; Zaehle et al., 2014), and that warming temperatures enhance mineralization, and thus increase nutrient availability to plants, in the CTC BDRD simulation (see also Figures 17a and 17b).

We next examine the evolution of the individual components of TEC: vegetation carbon (Figure 17d), SOM carbon in the top 1 m of the soil column (Figure 17e), and total litter carbon (Figure 17f). In CNST-forcing simulations, each of these carbon pools is stable in the CTC configuration, whereas they all decline in the ECA configuration. The largest declines in ECA ecosystem carbon pools occur for total litter, followed by SOM, then vegetation carbon. In historical simulations, LULCC removes vegetation and thus litter and soil inputs, resulting in a re-equilibration of the soil carbon pools and typically losses to the atmosphere (Li et al., 2018), this phenomenon is reflected in the loss of carbon from all pools in simulations where CO₂ is constant (BCRC-hist).

The responses of vegetation to increasing CO₂ concentrations are driven primarily by CO₂ fertilization, leading to enhanced primary production. The CO₂ fertilization effect is stronger in the CTC configuration than in ECA, especially toward the end of the twentieth century, likely due to the stronger phosphorus limitation in ECA (see section A0.2).

Two competing mechanisms impact soil and litter carbon response to increasing CO₂ concentrations. First, increased vegetation growth caused by the CO₂ fertilization effect leads to increased carbon input to soils via leaf litter production and plant mortality (Zhu, Piao, et al., 2016). Second, warmer temperatures lead to more rapid decomposition of SOM by heterotrophic microbiota, resulting in loss of carbon to the atmosphere (Bond-Lamberty et al., 2018).

The effects of both mechanisms can be seen in the evolution of soil and litter carbon stocks shown in Figures 17e and 17f. Soil and litter carbon increase in the BD cases due to fertilization. The litter pool response to fertilization is stronger in the ECA configuration, mainly driven by greater accumulation of coarse woody debris in ECA simulations (partitioning of carbon between different pools will be discussed in section 4.6.1, and is shown in Table 4). Both model configurations lose a small amount of SOM and litter carbon due to climate change (RD cases), with the litter losses somewhat larger for ECA than for CTC, probably reflecting decomposition losses from its larger coarse woody debris pool.

5.2. Geographic Distribution of GPP and CO₂ Responses in CTC and ECA Configurations

The geographic distribution of annual mean GPP (BCRC) and its differences between the CTC simulations are shown in Figure 19. Results for ECA simulations are similar and are provided in the supporting information (Figure S9). GPP is highest in tropical forest ecosystems, consistent with expectations and observational estimates (Figure 19a) (Anav et al., 2015; Chen et al., 2017). Figure 19b shows that the CO₂ fertilization effect on GPP (quantified as BDRC - BCRC) increases GPP globally, especially in the tropics. In contrast, the warming associated with the CO₂ radiative effect leads to increased GPP at high latitudes, where colder present-day temperatures limit ecosystem growth, while producing moderate declines in GPP in the tropics (Figure 19c). When operating together, the CO₂ fertilization effect dominates in the tropics, while the radiative effect dominates at high latitudes, leading to an overall increase in GPP across the globe (Figure 19d).

Warming reducing tropical GPP is reasonable given these ecosystems' already-warm environment, dependence on water availability via precipitation and deep soil water (Poulter et al., 2009), and sensitivity to drought (Bonal et al., 2016; Corlett, 2016; Poulter et al., 2009). The negative sensitivity of Arctic GPP to CO₂ increases in the CTC configuration is perhaps less expected but consistent with the highly divergent responses observed in high-latitude Canadian ecosystems (Girardin et al., 2016; Sulla-Menashe et al., 2018) for example, due to the complex interplay of CO₂ fertilization, fire, water stress, and perhaps permafrost thaw (Peñuelas et al., 2017).

5.3. Nutrient Limitation in CTC and ECA Configurations

Here we describe and compare the evolution of nitrogen and phosphorus limitation in the CTC and ECA configurations. Figure 18 shows the time evolution of the globally integrated biological nitrogen fixation to soil mineral nitrogen (Figure 18a) and soil mineral nitrogen pool (Figure 18b), as anomalies from their 1850–1859 means. The time evolution of both configurations as absolute values is shown in the supporting information (Figure S11).

In the default CTC simulations, biological nitrogen fixation is stable at ~86 TgN/yr throughout the CNST-forcing simulation, and exhibits only minor changes in response to historical forcings and increasing CO₂. In contrast, the ECA simulations begin with a higher initial rate of nitrogen fixation of around 130 TgN/yr and nitrogen fixation responds strongly to non-CO₂ historical forcings as well as to biogeochemical CO₂ coupling.

Soil mineral nitrogen (Figure 18b) increases over time in the CNST-forcing simulations; the increase is slight for CTC (from ~4 to 4.5 TgN) and moderate for ECA (from ~14 to 18.5 TgN). This trend indicates that the coupled global nutrient cycles were not completely equilibrated in the initial state. In the historical simulations, atmospheric deposition of nitrogen to land ecosystems increases rapidly after the first industrial-scale production of ammonia in 1913, leading to a rapid rise in soil mineral nitrogen in all historical simulations.

Across the historical simulations, the BD cases have less soil mineral nitrogen than biogeochemically uncoupled (BC) cases, due to the increased plant demand caused by CO₂ fertilization. Additionally, the radiatively coupled (RD) cases have less soil mineral nitrogen than the radiatively uncoupled (RC) cases due to increased soil microbial uptake under a warmer climate, and increased plant uptake at high latitudes

(Figure 19c). For ECA simulations, the soil mineral nitrogen content also increased across the historical simulations.

The evolution of the surface (top 40–60 cm) pools of both labile phosphorus and total soil mineral phosphorus, of which labile phosphorus is the most variable component, is shown in Figures 18c and 18d. In the CTC configuration, the labile phosphorus pool decreases slightly over the course of the control simulation, as leaching gradually removes phosphorus from land ecosystems. In the historical simulations, LULCC leads to an additional reduction in labile phosphorus, as clearance of vegetation biomass removes phosphorus from land ecosystems. Additionally, in the BD cases, the labile phosphorus pool is depleted more rapidly than the BC cases due to the enhanced vegetation productivity in the BD cases (Figure 17(a)) and associated enhanced phosphorus uptake.

The surface labile phosphorus pool is more rapidly depleted in the ECA configuration and the surface mineral phosphorus pool is also depleted. This different behavior resulted primarily from different initialization strategies for vertical distribution of soil mineral phosphorus. In the CTC simulations, the initial soil phosphorus pool was much larger in the total soil column and marginally larger in the top 50 cm, when compared with ECA (Table 7). In the ECA simulations, the limited availability of soil phosphorus in deeper layers constrains its mobilization to the surface. Additionally, ECA exhibits stronger leaching of phosphorus from land, as well as a net adsorption of phosphorus onto soil minerals, which contributes to the lower plant-available phosphorus in the ECA simulations, while CTC exhibits a net desorption, which may contribute to the more rapid removal of phosphorus in the ECA simulations. These and other differences in the globally integrated nutrient cycle budgets are discussed in section 4.6.

We quantified the extent of nitrogen and phosphorus limitation for plants and soils separately, as follows:

- Due to the structural differences between the CTC and ECA approaches, the nutrient limitation factor for plants is defined differently for each:
For CTC, the factor for plants is defined as the ratio of actual vegetation growth to potential vegetation growth if the instantaneous nutrient limitation did not exist, and is termed fraction of potential GPP (FPG). It is calculated separately for nitrogen (FPG_N) and phosphorus (FPG_P).
For ECA, the limitation factors l_n and l_p are calculated from the optimal and actual nutrient ratios with carbon, compared with the minimum nutrient ratios for the respective nutrient.
- CTC and ECA use the same definition of nutrient limitation for soil nutrient immobilization processes, the fraction of potential immobilization (FPI). FPI is the ratio of actual immobilization to potential immobilization if instantaneous nutrient limitation did not exist, and is calculated separately for nitrogen ($FPI_{N,CTC}$ and $FPI_{N,ECA}$) and phosphorus ($FPI_{P,CTC}$ and $FPI_{P,ECA}$).

For all nutrient limitation metrics, lower values indicate a stronger limitation on growth. Detailed explanations and definitions of the nutrient limitation factors are provided in section A0.2.

Figure 20 summarizes the nutrient limitation metrics across all simulations. Globally averaged FPG_P is greater than globally averaged FPG_N in all simulations (for both CTC and ECA), reflecting the greater role of nitrogen in limiting vegetative growth globally, as compared with phosphorus.

We first discuss the limitations on vegetative growth in the CTC simulations (Figures 20a and 20b). The fraction of potential GPP FPG_N is relatively stable in the CNST-forcing simulation, indicating little change in nitrogen limitation in the absence of external forcings. By contrast, the BCRC-hist case has weaker nitrogen limitation (increasing FPG_N), likely due to anthropogenic increases in atmospheric nitrogen deposition. The BCRD-hist simulation exhibits a further slight reduction in vegetation nitrogen limitation, likely due to increased soil nitrogen mineralization in a warming climate. In contrast, phosphorus limitation increases in the BC simulations. We hypothesize that this is a direct result of increases in nitrogen availability, which cause an increase in vegetation growth and a subsequent increase in phosphorus demand. In this situation, if phosphorus availability is not increasing as quickly as nitrogen availability, then phosphorus availability can become relatively more limiting for vegetation growth. In the BD simulations, both nitrogen and phosphorus limitation increases, possibly due to GPP increases in response to CO_2 fertilization, which increases the demand for both nitrogen and phosphorus.

Turning to soil nutrient limitation for CTC (Figures 20e and 20f), the CNST-forcing simulation again exhibits fairly constant limitation by nitrogen and phosphorus. In the BC simulations, both nitrogen and phosphorus limitation becomes weaker, while they remain fairly constant in the BD simulations. Further effort will be

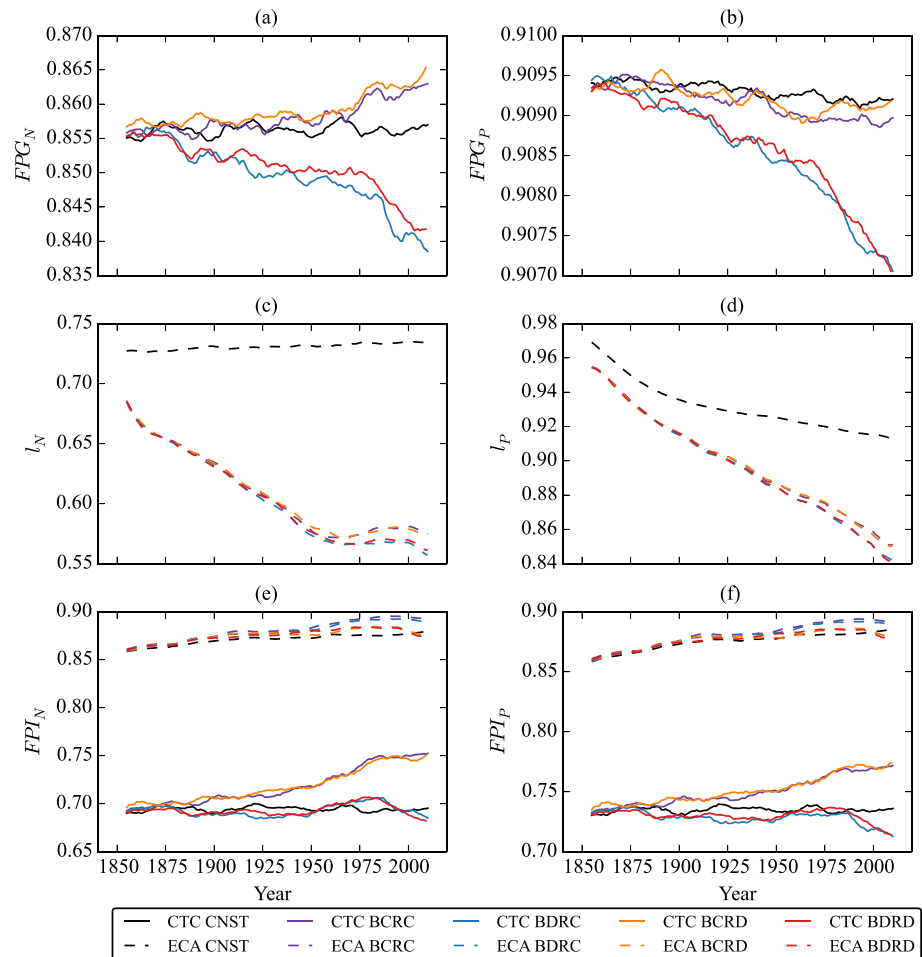


Figure 20. Time series of globally integrated land nutrient limitation metrics: (a) nitrogen limitation factor for plant growth in CTC, (b) phosphorus limitation factor for plant growth in CTC, (c) nitrogen limitation factor for plant growth in ECA ($1 - cn_scalar$), (d) P limitation factor for plant growth in ECA ($1 - cp_scalar$), (e) nitrogen limitation for microbial decomposition (CTC) and ECA), and (f) phosphorus limitation for microbial decomposition (CTC and ECA).

required to untangle the underlying mechanisms of these behaviors, which arise from a complex interaction of multiple processes, including changes in nitrogen deposition, LULCC, and changes in vegetation inputs to soils. There is no discernable indication of a radiative impact on CTC soil nutrient limitation.

We now turn to the globally integrated nutrient limitation metrics for the ECA vegetation (Figures 18c and 18d) and soils (Figures 18e and 18f) in the BDRD simulations. Although the vegetation nutrient limitation metrics for CTC and ECA cannot be compared quantitatively due to their different definitions (section A0.2), we note that the ECA approach represents concurrent limitation by nitrogen and phosphorus. Globally, at present day, ECA exhibits stronger limitation on vegetative growth by nitrogen than by phosphorus, as does CTC, but ECA has much stronger phosphorus limitation on photosynthesis than CTC, particularly in the tropics. The depletion of soil mineral phosphorus from surface soils by ECA causes a substantial increase in phosphorus limitation on plant growth as the ECA simulations progresses over the historical period (Figure 20d).

This difference in soil phosphorus limitation has important implications for the uptake of carbon into plants and soils. The increasing phosphorus limitation in the ECA simulation causes decreasing plant photosynthesis, litter production, and carbon input to soils from the litter pool.

To understand the role of nitrogen and phosphorus limitation in more detail, we examine the geographic distributions of nitrogen and phosphorus limitation metrics, as averaged over the last thirty years of the BDRD simulations (Figure 21).

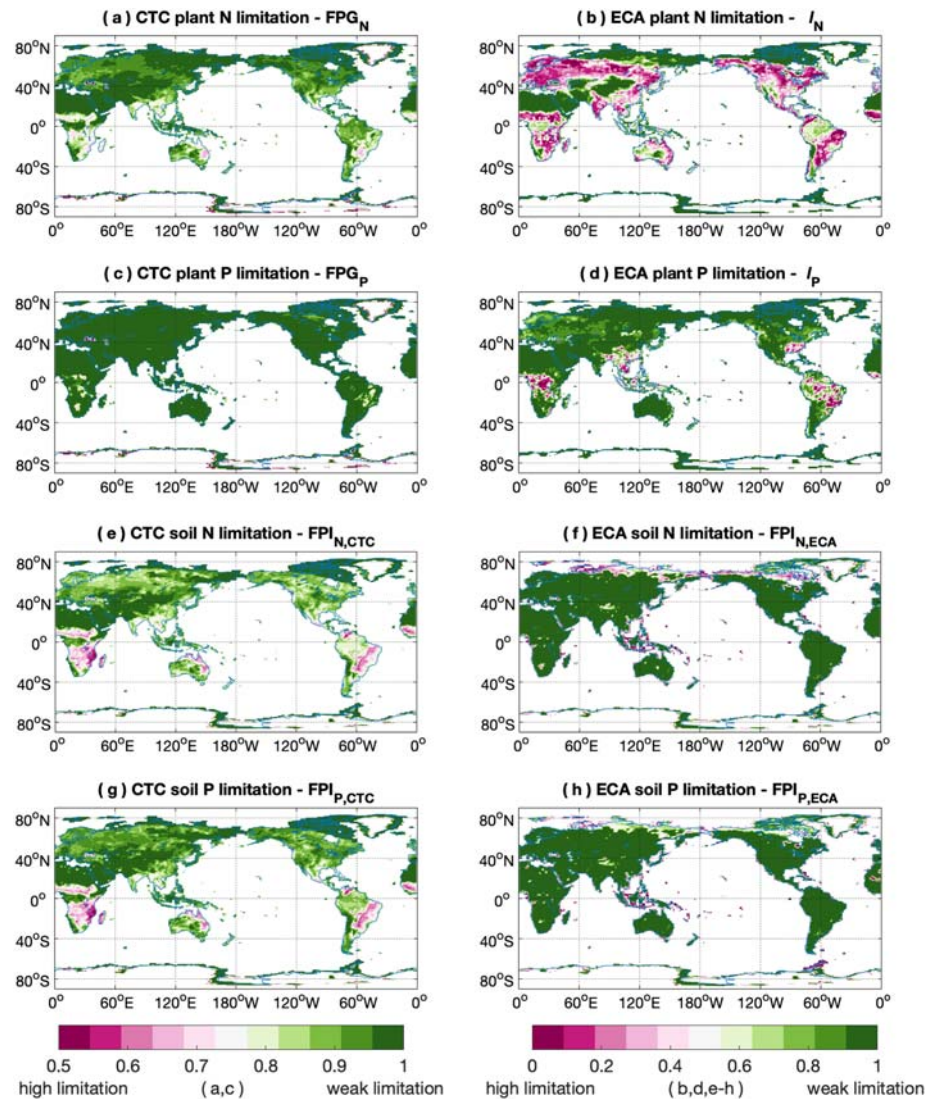


Figure 21. Geographic distribution of plant and soil nitrogen (a, b, e, and f) and phosphorus (c, d, g, and h) limitation metrics for CTC and ECA simulations, averaged over the last 30 years of BDRD-hist. Note that the color scale of (a) and (c) (0.5–1) is different from other panels (0–1).

In the CTC BDRD simulations, soils are more strongly limited by nutrient availability than plants (Figures 21a and 21e nitrogen limitation, Figures 21c and 21g phosphorus limitation). By contrast, in the ECA BDRD simulation, the nutrient limitation mainly constrains plant productivity rather than heterotrophic respiration (Figures 21b and 21f nitrogen limitation, Figures 21d and 21h phosphorus limitation). This difference occurs because in ECA, soil microbes trap soil nutrients more efficiently and tend to outcompete plants for nutrients, following Kuzyakov and Xu (2013).

In the ECA BDRD-hist simulations, the plant productivity is constrained by different nutrients in different regions. Low latitude ecosystems, particularly tropical rainforests, are strongly limited by phosphorus (Figure 21d), while the majority of mid- and high-latitude plants are strongly limited by nitrogen (Figure 21b). Note that in regions of the model where nutrient limitation is weak, growth may be more limited by environmental factors such as precipitation (in deserts) or temperature (at high latitudes).

Taken together, the results discussed in this section and section 5.1 show that structural differences between the CTC and ECA configurations of the model, combined with the different choices regarding the initialization of soil phosphorus, lead to a variety of differences in the behavior of their biogeochemical cycles. For many of the observed differences, observational constraints to distinguish which behaviors are more

realistic are limited, pointing to the need for improved observational products (Wang, Ciais, et al., 2018). This is particularly true for the newly introduced treatments of phosphorus cycling, as few observations of ecosystem phosphorus are available that are appropriate for constraining global ESM simulations (Yang et al., 2016). In particular, additional measurements (or syntheses) focused on the distribution of different forms of phosphorus with soil depth, extending to 1 m or more, would help constrain a next generation of nutrient-enabled models. Colocated measurement of nutrient concentrations and rooting distributions across a range of ecosystems and climate gradients would also help to constrain mechanistic representations of plant access to nutrients.

Follow-up studies are planned to further elucidate the structural differences between carbon, nitrogen, and phosphorus cycles, and their interactions with climate in these two model configurations, as well as to isolate the impact of including phosphorus limitation in the CTC (default) configuration of the model.

6. Interactions Between Ecosystem Responses and the Physical Climate System

6.1. Radiative and Ecosystem Effects on Temperature and Precipitation

In addition to the impacts of carbon dioxide and climate on ecosystems, the climate system also experiences feedbacks from ecosystem responses. For example, changes in surface evapotranspiration due to stomatal closure in response to increasing CO₂ Swann et al. (2010) (i.e., plant physiological response) or shifts in ecosystem productivity in response to CO₂ warming (i.e., radiative effect) may have substantial feedback onto climate dynamics.

Figures 22a and 22b shows the present-day (1985–2014) annual mean surface temperature, and precipitation, respectively, and the differences in these fields that arise from enabling plant physiological response ecosystem and/or radiative response effects to increasing atmospheric CO₂, with statistically significant responses indicated by stippling.

The impact of non-CO₂ historical forcings (aerosols and LULCC) on the present-day mean climate is shown in the lower left panels. Historical aerosol emissions, which were concentrated in the industrialized nations, likely explain the relatively greater cooling and drying in the Northern Hemisphere in response to non-CO₂ forcings.

The full impact of CO₂, that is, its combined radiative effect and plant physiological biogeochemical responses (BDRD-hist – BCRC-hist; top central panels), exhibits the expected characteristics of a warming planet, including amplification of the warming signal in the Arctic and intensification of the hydrological cycle (with increased precipitation). The warming pattern is attributable almost entirely to the radiative effect (BCRD-hist – BCRC-hist; bottom central panels).

The physiological effect of CO₂ (BDRD-hist – BCRC-hist; top right panels) is significantly weaker than the radiative effect in our simulations, but has significant nonlinear interactions with radiative effects (BDRD-hist – BDRD-hist – BDRD-hist + BCRC-hist). The nonlinear interaction term contributes significantly to the water budget in the Amazon and to modifying precipitation across the tropics. The precipitation response shows a similar zonal asymmetry to the results of Kooperman et al. (2018), with drying over the Amazon and increased rainfall over Africa and the Maritime Continent. The precipitation patterns are somewhat displaced relative to the multi-model mean shown in Figure 1 of Kooperman et al. (2018), which may be the result of the strong southward shift owing to aerosols seen in the lower left panel of Figure 22b. The cooling in the northern high latitudes from the physiology response may be related to cooling owing to reductions in water vapor from stomatal closure, consistent with Swann et al. (2010).

6.2. Calculation of Global Coupled Carbon-Climate Feedback Parameters

For the purpose of understanding projected future changes in atmospheric CO₂ concentrations under various greenhouse gas emissions scenarios and comparing projections across multiple models, it is useful to estimate coupled climate biogeochemistry model feedback characteristics (Gregory et al., 2009). In spite of some methodological differences in feedback calculations, this analysis allows us to examine the strength of these feedbacks in the E3SMv1.1-BGC relative to other models. While we only analyze results from historical simulations here, prior work has demonstrated that the early stages of their projected 21st century trajectories are already discernible in model results from the end of the twentieth century (Thornton et al., 2009). These results should be interpreted with caution, since future trajectories of feedback parameters depend on the specifics of future forcing scenarios.

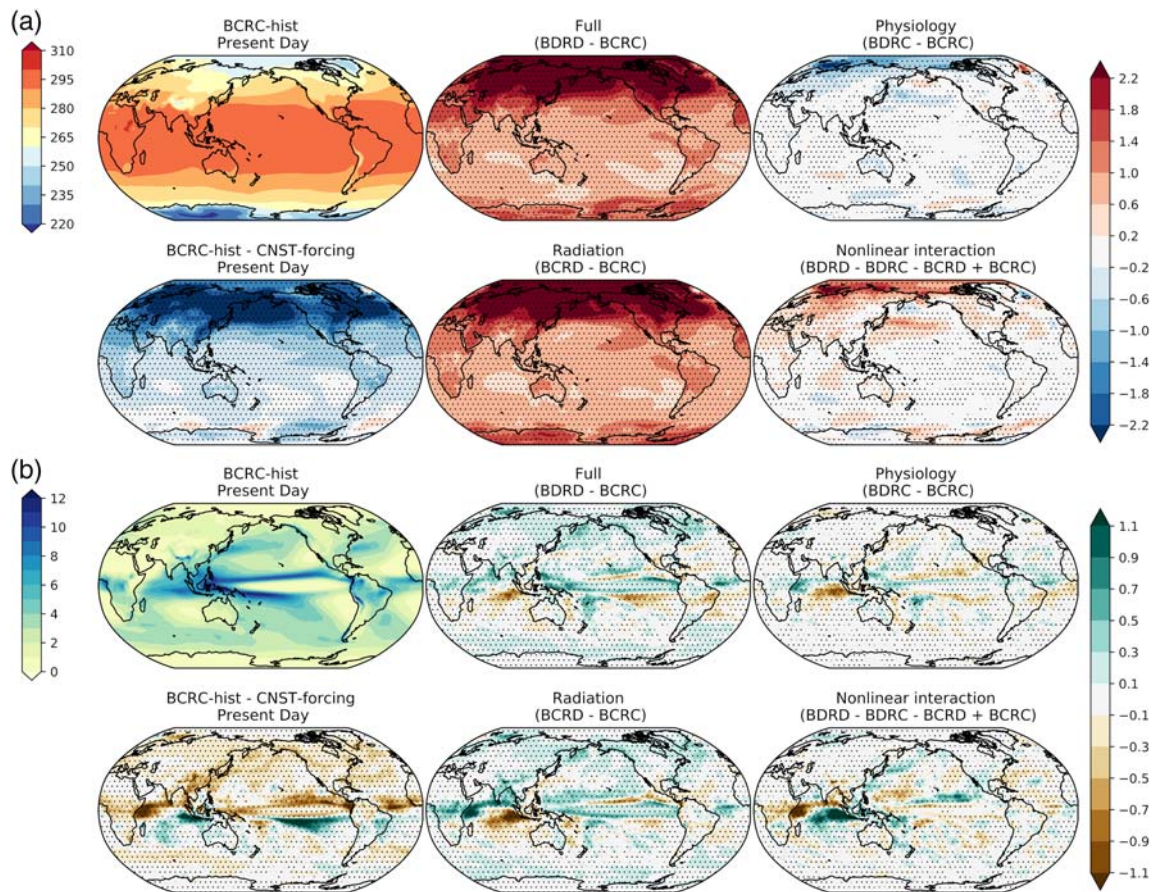


Figure 22. Present-day (1985–2014) mean climatological state of the E3SMv1.1-BGC's (a) 2-m air temperature (K) and (b) precipitation (mm/day), in the BCRC-hist simulation, and differences from the CNST-forcing and other historical experiments. For each figure, top row of panels shows the BCRC-hist simulation, the full (radiative+physiological) response to CO₂ (as BDRD-hist – BCRC-hist), and the physiology response (as BDRD-hist – BCRC-hist). Bottom row of panels shows the present-day change from preindustrial (BCRC-hist – CNST-forcing), radiation effect (as BCRD-hist – BCRC-hist), and the magnitude of the nonlinear interactions between the radiative and physiological effects, that is, (Full – Physiology – Radiation) = (BDRD-hist – BDRD-hist – BCRD-hist + BCRC-hist). For the full, physiology, radiation, and nonlinear panels, ‘-hist’ is removed from the panel titles for convenience. Stippling is included where differences pass a *t* test (at 95% confidence). Sixteen 30-year climatologies were constructed from the 500-year E3SMv1 piControl simulation to estimate the standard deviation of a 30-year climatology.

Here we use the feedback linearization framework described by Friedlingstein et al. (2006) to estimate the land and ocean carbon stock response to changing atmospheric CO₂ (β_{land} and β_{ocean} , respectively: PgC ppm⁻¹), the land and ocean carbon stock response to changing climate as characterized by global mean near-surface air temperature (γ_{land} and γ_{ocean} , respectively: PgC K⁻¹), as well as the linearized transient climate sensitivity to CO₂ (α : K ppm⁻¹). Following Gregory et al. (2009), we use the difference between simulations BDRD-hist and BCRC-hist to estimate β , and the difference between simulations BCRD-hist and BCRC-hist to estimate γ and α . We replace the end-point analysis of Friedlingstein et al. (2006) with the moving window regression analysis described in Thornton et al. (2009), reporting time series of the feedback parameters from regression windows of 75 and 100 years in length.

In spite of significant differences in the structure and function of the CTC and ECA land biogeochemistry configurations, they appear to converge on similar estimates of the carbon-concentration feedback strength (Figure 23a). The variability in estimates of β_{land} early in the twentieth century is expected, as the CO₂ fertilization effect is still weak compared to interannual variability in carbon fluxes. The values of 1.0–1.2 PgC ppm⁻¹ toward the end of the simulations suggest the fertilization effect has a low magnitude compared to models lacking carbon-nutrient feedbacks, and is similar in magnitude to other models with carbon-nutrient coupling (Arora et al., 2013, 2019; Thornton et al., 2009). The carbon-concentration feedback for the ocean appears to be on the low end of prior multimodel comparisons, and is similar in magnitude to the ocean biogeochemistry configuration reported in Thornton et al. (2009) (Figure 23b).

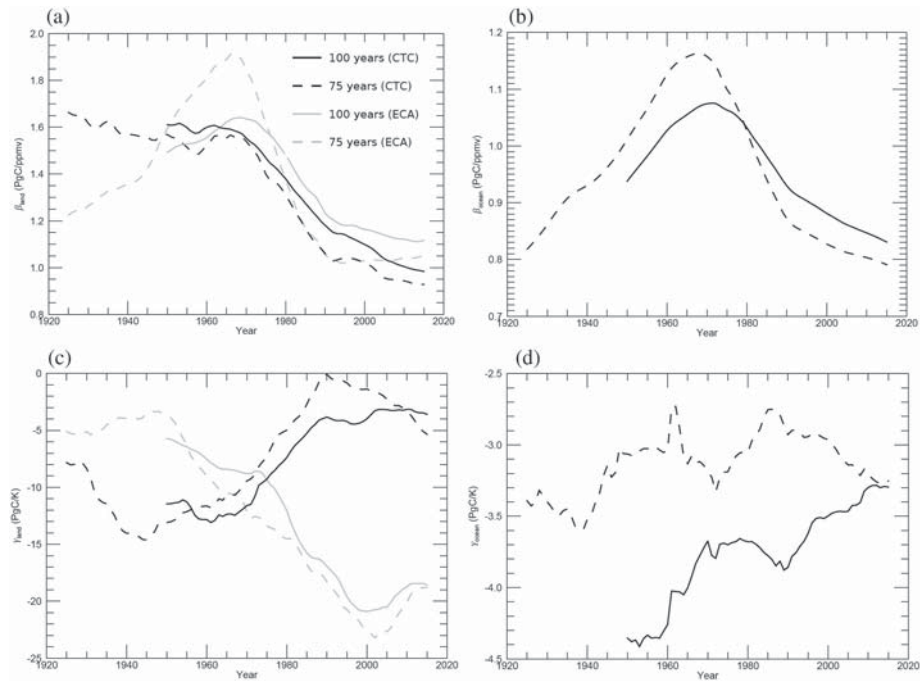


Figure 23. Model estimates of land and ocean carbon-climate feedback parameters, based on the definitions from Friedlingstein et al. (2006), but calculated using multiyear moving regressions as described in the text. (a, b) Temporal variation of land and ocean carbon storage to change in atmospheric CO₂ concentration (β_{land} and β_{ocean} , respectively). (c, d) Temporal variation of land and ocean carbon storage to change in global mean near-surface air temperature (γ_{land} and γ_{ocean} , respectively). Solid and dashed lines show results for regression windows of length 100 and 75 years, respectively. Black lines show results from E3SMv1.1-BGC simulations (using CTC), while gray lines (in a and c) show ECA results.

The carbon-climate feedback estimates for CTC and ECA land configurations appear to be diverging toward the end of these historical simulations (Figure 23c), but even so, both fall on the low-magnitude end of the values reported in other multimodel comparisons. This result is consistent with prior estimates from carbon-nutrient coupled models, suggesting a feedback closer to neutral than what has been estimated previously with nonnutrient-enabled models. The introduction of terrestrial phosphorus cycle coupling in E3SM

v1.1 does not appear to fundamentally alter the feedback behavior of either model configuration compared to earlier carbon-nitrogen coupled models. The ocean carbon-climate feedback appears to be converging on a low-magnitude negative value, similar to the behavior observed for ocean biogeochemistry in CESM1-BGC (Thornton et al., 2009).

The transient climate sensitivity to rising CO₂ concentration (α , Figure 24) is at the high end of prior model estimates, but previous work suggests that this value is likely to decline over time as the simulations progress into a future high-forcing scenario (Thornton et al., 2009). This strong radiative forcing for the E3SMv1.1 model is consistent with analysis of the E3SMv1.0-DECK model in simulations without biogeochemical coupling (Golaz et al., 2019).

We note that feedback parameter estimates are likely to shift as these simulations progress from the historical period into future scenarios. Also, with nitrogen deposition, land use change, and changes in aerosols and other transient factors in effect, comparison to simpler simulations such as the 1 pct/yr rising CO₂ protocol used in Arora et al. (2013) is not direct. Comparison to the historical period from Thornton et al. (2009) is more robust since that study used a similar set of historical forcings.

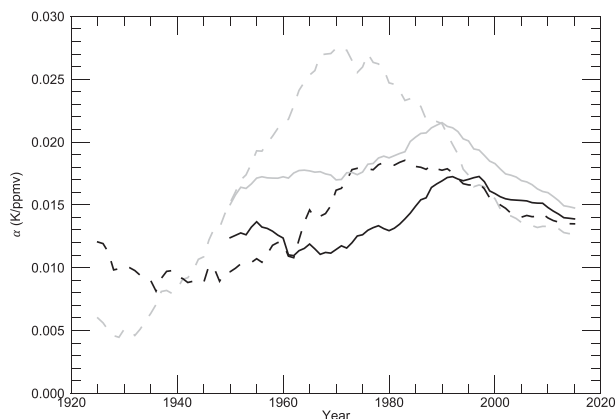


Figure 24. Model estimate of the sensitivity of mean global near-surface air temperature (over land and ocean) to change in atmospheric CO₂ concentration (α), based on definition from Friedlingstein et al. (2006), but calculated using moving regressions as described in text. Line styles are as in Figure 23.

The analysis of the E3SMv1.1 biogeochemistry model under 21st century climate projections and the 1 pct/yr rising CO₂ protocol will be the subject of future publications.

7. Planned Improvements to Biogeochemistry, Land, and Energy Systems in Future Versions of E3SM

Here we provide an overview of the model developments underway and planned for upcoming versions of E3SM, focusing on biogeochemistry, land, and energy systems, and their interactions with the Earth system and climate.

In particular, the E3SM biogeochemistry science question for E3SMv2 is: “What are the implications of different energy futures for the biogeochemical cycle through changes in land use land cover, water availability, and extreme events?”

Using insights gained from this study and other intercomparison efforts, the E3SM project is currently working to identify and consolidate the best features of both approaches to representing terrestrial biogeochemistry, and v2 of E3SM will use only a single approach to represent and initialize the land biogeochemistry. Near-term development efforts will shift our focus toward various other aspects of the broader E3SMv2 science question.

Several near-term (v2) developments are targeted toward improving the model's capabilities to address this question. Recent efforts have coupled E3SM to the Global Change Assessment Model (GCAM), a global Integrated Assessment Model (Calvin et al., 2019). GCAM projects emissions and concentrations of greenhouse gases, aerosols, and aerosol precursors, as well as LULCC. E3SM simulates changes in the Earth system that affect the human system, for example, temperature and precipitation changes that impact agricultural productivity and energy demand, altering the future emissions and LULCC pathways GCAM projects. By allowing two-way feedback between GCAM and E3SM, energy use and LULCC change can respond dynamically to climate, with implications for simulated future energy pathways and climate responses (Collins et al., 2015; Jones et al., 2018; Thornton et al., 2017).

Additional, longer-term developments are planned for future versions (v3 and beyond). To better simulate the impacts of climate on agriculture, the crop model, which is present in the E3SMv1 code base but was not active in the simulations presented here, will be used as part of the default configuration in future model versions. The crop model replaces the current generic grassy crop with three crop classes (maize, wheat, and soybean). The crop model is based on the representation described in Levis et al. (2012), but with updates to include dynamic roots (Drewniak, 2019) and a new dynamic planting date scheme. An irrigation module will be used to simulate the impacts of surface water and groundwater irrigation water supply on land-atmosphere interactions (Leng et al., 2017). Agricultural production and irrigation have important effects on soil erosion. A new soil erosion model will be used to simulate impacts on the biogeochemical cycle (Tan et al., 2017, 2018).

The land model in future versions of E3SM will also be updated with a refactored model grid to enable better representation of subgrid heterogeneity in the land surface, particularly surface topography (Tesfa & Leung, 2017). A new soil hydrology scheme will be available, the Variable Saturation Flow Model (Bisht et al., 2018). The addition of regionally resolved grids in the atmosphere model, with higher resolution over North America will support representation of managed systems (e.g., built energy and water infrastructure) with greater fidelity.

Additionally, for future versions of E3SM, the project plans to incorporate dynamic vegetation via the Functionally Assembled Terrestrial Ecosystem Simulator model (Fisher et al., 2015), allowing vegetation classes to migrate in response to climate change.

In the ocean model, E3SM will incorporate the Marine Biogeochemistry Library (MARBL; <https://climate.modeling.science.energy.gov/projects/marbl-marine-biogeochemistry-library>). The DOE has funded the MARBL project to develop a library for the simulation of marine ecosystems and biogeochemical cycles that is independent of the host ocean model. In incorporating MARBL, E3SM will largely retain biogeochemistry formulations similar to those in the E3SMv1.1 model and will gain flexibility to benefit from new developments and improvements to ocean biogeochemistry capabilities contributed to the MARBL library by

other investigators. Additional improvements to the representation of ocean physics are planned, including improved vertical mixing, and corrected Redi isopycnal diffusion.

Planned developments for future versions of EAM will advance E3SM's capabilities for simulating interactions between natural and managed biogeochemical and energy systems and climate. Future versions of EAM will incorporate more detailed, but still concise and computationally efficient, treatments of gas-phase atmospheric chemistry, enabling dynamic representation of short-lived climate forcers (methane, ozone) and their couplings to surface systems. Additional changes will include improved coupling of aerosols, CO₂, and other greenhouse gases to simulated surface fluxes, and improved calculation of the influence of clouds and aerosols on photosynthetically active radiation.

Finally, the coupling of land and ocean biogeochemical cycles will be represented in greater detail in future E3SM versions through developments to the MOSART river model. A stream temperature module will be incorporated to improve representation of heat and moisture exchange with the atmosphere (Li, Ruby Leung, et al., 2015). A water management module will add representation of the two most important water management activities: reservoir regulation and surface water extraction (Li, Ruby Leung, et al., 2015; Voisin, Li, et al., 2013; Voisin, Liu, et al., 2013). Finally, new modules will treat suspended sediments, an important step toward coupling the riverine transport of sediments, as well as nutrients in their particulate and dissolved forms. Ultimately, the project aims to couple this riverine discharge to radiative transfer and biological production in estuaries and the ocean.

8. Summary and Conclusions

Natural and managed processes on the land and in the ocean have a significant impact on the carbon cycle and its influence on climate, including surface temperature, precipitation, evapotranspiration, and atmospheric greenhouse gas concentrations. Limits in the availability of nutrients, however, can reduce carbon uptake and affect the surface energy balance, impacting the coupled carbon-climate system.

To explore these dynamics, this paper has introduced E3SMv1.1. We have presented simulations that have been carried out in two model configurations:

- The default configuration, E3SMv1.1-BGC, includes the CTC as the land model biogeochemistry framework as well as coupled ocean-sea ice biogeochemistry. Two notable new features in this model version are (1) the introduction of a soil and vegetation phosphorus nutrient cycle and (2) two-way coupling of ocean and sea ice carbon and nitrogen cycles.
- An alternative land model configuration, E3SM-v1.1-BGC-ECA, which couples carbon, nitrogen, and phosphorus cycles using the ECA approach, is used to explore the impacts of land model structural uncertainties.

Both model configurations exhibit physical climates similar to the climate of the E3SMv1.0-DECK, which has been extensively documented in Golaz et al. (2019). Transient historical simulations show a stronger midtwentieth century cooling than the historical record followed by a stronger late twentieth century warming. The RD cases are slightly cooler than the five-member E3SMv1.0-DECK historical ensemble during some periods, but generally fall within the range of ensemble variability. Northern Hemisphere SWE over nonglaciated land has similar transient behavior to the E3SMv1.0-DECK. When compared with GlobSnow-2 observations (1979–2014), E3SMv1.1 exhibits regional overprediction and underprediction of SWE over Arctic and sub-Arctic land. Ocean and sea ice also exhibited similar biases to those described in Golaz et al. (2019), including overly extensive sea ice in the Labrador Sea, resulting in a strong cold and fresh water bias in the North Atlantic and weak overturning, reducing replenishment of nutrients in the photic zone. Additionally, the Arctic consistently exhibits excessively thick sea ice in the region from the Beaufort Sea through the Siberian Sea.

Rising CO₂ impacts physical climate through both the direct radiative pathway (greenhouse gas effect) and the indirect physiological pathway (biogeochemical responses including fertilization and stomatal responses). We find that atmospheric temperature changes are dominated by the radiative effect, while changes in precipitation have important contributions from physiological effects and their nonlinear interactions with radiative effects.

In the default E3SMv1.1-BGC configuration (CTC), the carbon cycle is stable throughout the CNST-forcing simulation. The ECA configuration exhibited carbon losses throughout the CNST-forcing simulation,

consistent with its stronger nutrient limitations on the carbon cycle. Both configurations simulate historical trends in GPP and key carbon cycle metrics (globally integrated NEE and carbon pools) that show the expected losses of carbon associated with LULCC, combined with responses to different carbon coupling scenarios (radiative versus biogeochemical coupling). Simulated GPP is highest in tropical ecosystems, consistent with theoretical expectations and observations. Modeled CO_2 fertilization led to greater vegetation carbon uptake in both configurations, and thus higher litter and soil carbon in BD scenarios. Increased heterotrophic respiration led to more rapid decomposition and losses from litter and soil carbon pools in the warming climate of the RD scenarios. CO_2 fertilization increases tropical GPP, but to different degrees in the CTC and ECA configurations, while the radiative impact of CO_2 increases GPP at high latitudes, leading to global increases in GPP when both effects operate together.

The model showed overall improvements in modeled carbon, hydrology, and energy cycles compared to CMIP5 models in the ILAMB package. Both the CTC and ECA configurations fell within the wide range of observationally constrained estimates of global GPP, 0–1 m SOM carbon stocks, and vegetation and soil nitrogen and phosphorus content, but differ in their geographic and temporal distributions. The configurations differed in estimates of biological nitrogen fixation, but fell within the very wide range of observational constraints; we highlight this difference as an important avenue for future research, since the modeled carbon cycles are sensitive to ecosystem nitrogen inputs. A thorough benchmarking exercise for phosphorus dynamics will require investment in developing large-scale observational constraints for these types of models. The full suite of ILAMB benchmarks and visualizations of the underlying model and observational data sets can be explored in the interactive online ILAMB tool, provided as part of the supporting information for this paper (Data Set S1; additional documentation details in Text S6).

With respect to evaluating structural uncertainty in nutrient controls on the terrestrial carbon cycle, we note the large differences between the CTC and ECA configurations in their emergent nitrogen and phosphorus controls on soil decomposition (relatively strong in CTC and weak in ECA) and photosynthesis (relatively strong in ECA and weak in CTC). Present day photosynthesis in CTC is not strongly limited by either nitrogen or phosphorus, while heterotrophic respiration is colimited, most strongly in the tropics and moderately across temperate and high latitudes. In the ECA configuration, present-day photosynthesis is colimited by nitrogen and phosphorus in the tropics, and more strongly nitrogen-limited at high latitudes, although some high-latitude phosphorus colimitation is also modeled. Soil heterotrophic respiration in ECA is nitrogen and phosphorus co-limited at high latitudes, and much less so in temperate and tropical latitudes. These contrasting emergent nutrient controls on the global terrestrial carbon cycle motivate new observations of nutrient constraints that can help develop and falsify land model structural hypotheses. Additionally, CTC and ECA partition carbon differently, with CTC storing more carbon in soils below 1 m and ECA producing more woody debris. These differences may have consequences for carbon cycle feedbacks, particularly over longer time scales and in future scenarios.

As a first step toward understanding the potential implications of simulated land atmosphere CO_2 fluxes for atmospheric concentrations, we used a new ILAMB capability the CO_2 seasonal and interannual variability implied by ELMv1.1 CO_2 fluxes. Overall, inferred fluxes agree with observations better in the Northern Hemisphere midlatitudes, and worse in tropics and Southern Hemisphere, probably due to a combined effect of the larger ocean influence on seasonal and interannual variability of CO_2 concentrations in the tropics and Southern Hemisphere, and to inherent difficulties in accurately simulating interhemispheric exchange. Many of the changes made in the model since it branched from CESM will have substantial impacts on transport, in particular the deep convection parameterization has been replaced and the 30-level vertical grid.

Turning to the ocean carbon cycle, we examine the behavior of the modified BEC biogeochemical model, which was implemented into the MPAS-Ocean for inclusion into E3SMv1. We have identified some important biases that will need to be addressed before the ocean biogeochemistry can be used for scientific investigations. Surface chlorophyll concentrations are biased low in nearly all parts of the global ocean, most prominently in the regions north of 35°N . Physical biases in the new MPAS-Ocean model are likely a dominant cause of the insufficient oceanic biomass production, specifically:

1. Ocean surface nitrate and phosphate have large low biases, particularly the North Atlantic and Arctic. This is likely due to a deficiency in deep overturning and the associated replenishment of nutrients.

2. Lateral mixing is too limited in the ocean, causing insufficient ventilation and unrealistic expansion of the subsurface OMZs. This inhibits remineralization of dissolved and particulate organic carbon, nitrogen, and phosphorus, which in turn limits nutrient availability for primary production.

Sea ice algal production in the Arctic is strongly constrained by the low biases in surface ocean nitrate and silicate, leading to significant underestimation of sea ice primary production. Southern Ocean ice primary production is light-limited and so is less affected by biases in surface nutrient supply, but is near the low end of previous estimates.

Overall, the E3SMv1.1 coupled ocean-sea ice biogeochemistry significantly underpredicts the anthropogenic ocean sink, with much of the bias likely due to the impacts of deficiencies in aspects of the ocean physics that are critical to ocean biogeochemistry. This points to the need for additional effort to improve the treatment of ocean transport and biogeochemical processes in future versions of E3SM.

Coupled carbon-climate cycle feedbacks were evaluated using the linearization framework described by Friedlingstein et al. (2006), which allows comparison of the feedback parameters with the ancestor model, CESM1-BGC (Thornton et al., 2009), and with intercomparisons of the strength of carbon cycle-climate feedbacks across multiple models (Arora et al., 2013). We find that in spite of significant structural differences, the CTC and ECA configurations converge on similar estimates of the carbon-concentration feedback strength, with $\beta_{land} = 1.0\text{--}1.2 \text{ PgC/yr}$ by the end of the twentieth century. The carbon-climate feedback strength in the two configurations starts to diverge by the end of the twentieth century, but both configurations show γ_{land} values that are lower in magnitude than other ESMs. These results suggest that both the fertilization and climate feedback effects are relatively weak in both configurations of E3SMv1.1 when compared with models that do not incorporate nutrient limitations on carbon uptake (Arora et al., 2013; Thornton et al., 2009). The similarity to results reported in (Thornton et al., 2009) suggests that the inclusion of phosphorus limitation in the land does not have a strong impact on the coupled carbon-climate feedbacks during the historical simulations presented here, but those differences may emerge more strongly under future forcing scenarios. Additional efforts are ongoing to characterize the impacts of phosphorus limitation on various aspects of the model's biogeochemistry under future forcing scenarios. The ocean model's carbon-concentration and carbon-climate feedback strengths are both similar in magnitude to the ocean biogeochemistry configuration in CESM-BGC as reported in (Thornton et al., 2009) and at the low end of prior multi-model intercomparisons.

Planned future developments to E3SM will improve the model's capabilities to simulate the responses of biogeochemical cycles to different energy futures, and the interactions of those responses with changes in land use land cover, water availability, and extreme events. These developments will include a more complete coupling between the GCAM integrated assessment model and E3SM in order to simulate the two-way feedbacks between human activities and climate. In the land model, we plan to improve capabilities for simulating climate impacts on agriculture, improve the representation of subgrid heterogeneity in the land surface, and incorporate dynamic vegetation. In the ocean model, E3SM will incorporate MARBL and address deficiencies in the model's physical climate that impede accurate representation of ocean biogeochemistry in E3SMv1.1. In the atmosphere, we will incorporate more detailed treatments of gas-phase atmospheric chemistry, improve the calculation of photosynthetically active radiation, and improve couplings of atmospheric tracers to surface fluxes.

In addition to future model developments, improved observations are also necessary to further constrain the model. The two configurations of the E3SMv1.1 model have very different carbon dynamics but perform similarly against the standard ILAMB benchmarks. For example, one notable difference between the two configurations is with respect to phosphorous, including both vertical distribution of phosphorous today and the magnitude of the effect of phosphorous limitations on carbon uptake, neither of which have current global observations. This demonstrates the need for additional observations to distinguish between the behaviors of structurally different models.

Interestingly, in spite of differences between the two model configurations in their approach to representing biogeochemical processes, and in certain behaviors such as the temporal evolution of soil nutrient pools, both CTC and ECA converge to similar results for global parameters of carbon-climate feedback, β_{land} , γ_{land} , which have been used in past model intercomparisons. Additional effort is needed to determine whether this similarity persists for future projections, as the impacts of nutrient limitation in ecosystems act over

longer times scales, and also to investigate other differences in behavior between the models. Based on the results presented here and other intercomparison efforts, v2 of E3SM will consolidate the best features of both approaches to representing terrestrial biogeochemistry, and use only a single representation.

In summary, we have introduced a new version of the E3SM model, with active biogeochemistry in the land, ocean, and ice. We have used this model to examine carbon-climate dynamics. Additionally, we have compared the model to observational benchmarks, noting model biases. Future work will use this version of the model to explore other aspects of nutrient limits and structural uncertainty in the coupled system. Additionally, model developments are planned to reduce existing biases and enhance the capabilities of the model.

Appendix A: Calculation of Nitrogen, Phosphorus Nutrient Limitation Metrics

A1. Nutrient Limitation Metrics for CTC

In CTC, plants and microbes compete for nutrients (both nitrogen and phosphorus) on the basis of their *relative demand*: the balance between actual nutrient supply (plant and microbial uptake) and potential demand for nutrients determines the extent of nutrient limitation for plant growth and microbial decomposition. Potential nutrient demand for plants ($F_{\text{plant_demand}}$) is calculated based on photosynthetic carbon uptake, allometric parameters that relate allocation between various tissues, and specified carbon:nutrient ratios for each tissue type, as well as nutrient flux from retranslocation. Photosynthetic carbon uptake itself is a function of prognostic and evolving vegetation canopy state, and evolving environmental factors such as soil moisture, temperature, humidity, and atmospheric CO_2 concentration. Nutrient demand for microbial immobilization is the sum of all potential immobilization fluxes during litter and SOM decomposition ($F_{\text{potential_immobilization}}$). The nitrogen limitation factors for plant growth (FPG) and microbial decomposition (FPI) are then calculated as:

$$FPG = \frac{F_{\text{plant_uptake}}}{F_{\text{plant_demand}}} \quad (\text{A1})$$

$$FPI = \frac{F_{\text{actual_immobilization}}}{F_{\text{potential_immobilization}}} \quad (\text{A2})$$

The phosphorus limitation factors for plant growth (FPG_P) and microbial decomposition (FPI_P) are calculated in a similar manner to Yang et al. (2014). Finally, nutrient uptake for plants ($F_{\text{plant_uptake}}$) and nutrient immobilization ($F_{\text{actual_immobilization}}$) by microbes are based on the nutrient availability and their relative demand.

A2. Nutrient Limitation Metrics for ECA

In the ECA configuration, the nutrient uptake of the plant and microbial pools are based on their competitiveness or uptake capacity rather than on nutrient uptake demand, for example, plants could have high demand but still lower competitiveness than microbes. Under nutrient-abundant conditions, the full uptake capacity is activated to compete with other nutrient consumers (e.g., microbes), while under nutrient-limited conditions, a plant will deactivate a portion of its nutrient carrier enzymes and down-regulate the uptake capacity accordingly. Plants' *nutrient limitation factor* is the difference between the carbon:nutrient ratio calculated prognostically by the model and its minimum value, relative to the difference between the optimal and minimum value of the respective ratio. The factor is limited to fall in the range [0, 1], where 1 indicates no limitation, and values approaching 0 indicate increasingly stronger limitation by that nutrient.

For example, the nitrogen limitation factor for leaf uptake of carbon, l_n , is defined as:

$$l_n = 1 - \max \left\{ \min \left\{ \frac{CN_{\text{act}} - CN_{\text{min}}}{CN_{\text{opt}} - CN_{\text{min}}}, 1 \right\}, 0 \right\} \quad (\text{A3})$$

where CN_{min} is the minimal leaf carbon:nitrogen ratio, CN_{opt} is the optimal leaf carbon:nitrogen ratio, and CN_{act} is the actual leaf carbon:nitrogen ratio.

The nutrient limitation factor for soil microbes is based on the ratio between the actual soil immobilization after ECA competition (e.g., with plants) and the potential immobilization before ECA competition. These approaches to calculating nutrient limitation were introduced and documented further in Zhu et al. (2019).

Appendix B: The International Land Model Benchmarking Package

The ILAMB package provides a comprehensive assessment of land model fidelity through comparison with terrestrial biogeochemical and hydrological site-based, regional, and global observational data sets on seasonal, annual, and interannual time scales (Collier et al., 2018; Hoffman et al., 2017). It compares model variables with observations and scores model performance based on a combination of bias, RMSE, spatial distribution, seasonal cycle, and long-term trend metrics. Relationships between many biogeochemical variables and physical driver variables are calculated from model results and compared with observational estimates, and performance on these functional relationships contributes to overall model scores. ILAMB provides detailed graphical diagnostics and tabular information about each model-data comparison, and it features an interactive interface designed to enable the user to explore land biogeochemical and hydrological model responses to underlying environmental drivers.

Appendix C: Input Data Sets

Except where noted below, the E3SMv1.1-BGC simulations used the same inputs as the E3SMv1.0 DECK simulations, which are described in Golaz et al. (2019, Appendix B). The input data sets generally followed the input4MIPS data sets, which are described by the input4MIPS document at this site (<https://goo.gl/r8up31>).

C1. Nitrogen Deposition—Land

Atmospheric deposition is an important source of biologically active nitrogen to the terrestrial biosphere, particularly during the last few decades and in future projected scenarios, due to intense anthropogenic production. The E3SM-BGCv1.1 simulations directly use the atmospheric nitrogen deposition as nitrogen input to the land surface based on C4MIP standard (Jones et al., 2016). Nitrogen deposition input files were obtained from CMIP6 input4MIPS repository (<https://esgf-node.llnl.gov/projects/input4mips/> Hegglin et al., 2016) for the historical period (1850–2014) and the SSP585 future scenario (2015–2099), and regridded to the ELM ne30 grid. The input4MIPS files provide deposition inputs separately for the dry and wet deposition pathways, both for NH_x and NO_y , which were simulated by the Chemistry-Climate Model Initiative version of the CESM model at National Center for Atmospheric Research. Because the ELMv1 does not differentiate between these different modes of nitrogen deposition, all four inputs were summed to provide a total atmospheric nitrogen deposition to land.

C2. Ocean Biogeochemistry Input Files: Riverine Inputs, Atmospheric Nitrogen, and Iron Deposition

Several ocean biogeochemistry fields are subject to external climatological inputs from the atmosphere, land, and sea floor sediments that are supplied as prescribed input files in the E3SMv1.1-BGC simulations. After the simulations had already progressed significantly, it was discovered that the ocean biogeochemistry model was using a different nitrogen deposition data set (Lamarque et al., 2010) than the land model. Since this was judged unlikely to have a significant effect on the simulation results, we chose to continue simulations with this minor discrepancy. Atmospheric iron deposition is based on the dust climatology from Luo et al. (2003) as modified by Krishnamurthy et al. (2009) to allow spatially variable solubility. Sedimentary iron fluxes are based on Moore and Braucher (2008) using climatological E3SM particulate carbon fluxes calculated during the spin-up phase. Due to the relatively low rate of carbon burial in the model, the magnitude of the sedimentary iron flux was increased by a factor of 5 to maintain quasi-steady globally integrated iron levels. Riverine inputs of several constituents (organic and inorganic nitrogen, carbon, and phosphorus as well as iron, silicate, and alkalinity) to the ocean are prescribed as a monthly climatology, which was calculated using the NEWS model (Mayorga et al., 2010).

C3. Phosphorus Initial Conditions

Since soil phosphorus transformations occur on geological time scales, calculating an appropriate initial condition for phosphorus by explicitly modeling the nutrient cycles would be prohibitively expensive.

Instead, we derive our initial condition for phosphorus using an approach that appropriately estimates the global distribution of soil phosphorus for use in global biogeochemical models. In previously published work (Yang et al., 2013), we assembled databases of global surface lithology, rock phosphorus concentration, and soil weathering stages, along with measurements from soil chronosequences, vertical pedon profiles, and data on various forms of soil phosphorus (labile, secondary mineral, etc.), to develop global maps of various forms of soil phosphorus (Yang & Post, 2011). The published soil P data set (Yang et al., 2013) does not cover all of the land grid cells in the ELM, so a small number of missing grid cells were filled in using the values from their nearest neighbors.

The global soil phosphorus data set was developed to be representative for the top 50 cm of soils. Since we currently lack a detailed understanding of the vertical distribution of phosphorus in soils, we used simple assumptions to vertically distribute phosphorus in the soil column. For the E3SMv1.1-BGC configuration, we assumed the initial phosphorus concentrations to be the same in each layer. For the E3SMv1.1-BGC-ECA configuration, we initialized the soil phosphorus vertical profile to follow an exponential decay curve (Jobbgy & Jackson, 2001), with an e -folding length of 3 m, rescaled to conserve the total phosphorus area concentration [gP/m^2] for the whole soil column.

C4. LULCC

The Land-Use harmonization data set (LUH2 v2h Hurtt et al., 2017; <https://luh.umd.edu>) is the standard land use product for the CMIP6 and the same file used by the E3SM-DECK simulations described in Golaz et al. (2019). The LUH2 data set was regridded to the E3SM ne30 grid and LUH2 land types were remapped to five types: crop, pasture, urban, primary, and secondary. Specific PFTs were assigned to each category based on historical distributions of land types, as described in (Di Vittorio et al., 2014, 2018). In particular, we use the default method of converting land use to LULCC as described in Di Vittorio et al. (2018). As noted in that article, the precise means of converting land use to LULCC could result in a difference in CO_2 concentrations of up to 5 ppmv in 2004.

C5. Solar Input

Solar irradiances were specified monthly from v3.2 of the input4MIPS solar irradiance data set. This is the same file used by the E3SM-DECK experiments described in Golaz et al. (2019).

C6. Orbital Parameters

Earth's orbital parameters were inadvertently fixed to 1990 values for all DECK simulations and, for consistency, this bug was not fixed for the E3SMv1.1-BGC simulations. The impact on simulated climate is expected to be very minor over the historical time period. This was also true for the DECK simulations by E3SMv1 described by Golaz et al. (2019)

Appendix D: Software Engineering Practices for Transparency, Provenance and Reproducibility

The E3SM project team has invested significant effort into improving software engineering practices across the project, including the implementation of an automated testing system to improve the robustness and efficiency of code development, code reviews, and the development of infrastructure for provenance capture and analysis. For optimal transparency, the E3SM project follows an open development model, that is, the model code, its full development history, and reported issues are maintained and available from the public github repository (<https://github.com/E3SM-Project/E3SM>). To ensure reproducibility, a standardized script (run_e3sm) downloads the specified version of the model code, configures and builds the model, sets paths to initial conditions and boundary conditions as well as other runtime parameters, and submits the model simulation to the queuing system. By implementing a single command to configure, build, and execute each production simulation, we ensure reproducibility and provenance of these simulations. Finally, for the present simulation campaign, we implemented the use of a checklist for the verification of key model configuration details, a practice shown by extensive research to significantly reduce rates of human error and improve outcomes in many complex fields of work (Hales & Pronovost, 2006). For each simulation, this checklist was verified by representatives of each component model to ensure that all aspects of the simulations were correctly configured.

Acknowledgments

We thank Cortland Johnson for assistance in preparing Figures 1, 2, and 3. We also thank three anonymous reviewers for their careful comments, which helped to significantly improve the manuscript. This research was supported as part of the Energy Exascale Earth System Model (E3SM) project, funded by the U.S. Department of Energy, Office of Science, Office of Biological and Environmental Research. Additional support was provided by the Reducing Uncertainties in Biogeochemical Interactions through Synthesis and Computation (RUBISCO) Scientific Focus Area (SFA), which is sponsored by the Regional and Global Model Analysis (RGMA) Program in the Earth and Environmental Systems Sciences Division (EESDD) of the Office of Biological and Environmental Research in the U.S. Department of Energy Office of Science. We acknowledge the World Climate Research Programme's Working Group on Coupled Modelling, which is responsible for CMIP, and we thank the climate modeling groups (listed in the supporting information, Table S1) for producing and making available their model output. For CMIP the U.S. Department of Energy's Program for Climate Model Diagnosis and Intercomparison provides coordinating support and led development of software infrastructure in partnership with the Global Organization for Earth System Science Portals. Simulations described in this work, and most developmental simulations leading up to them, relied on computational resources provided by the National Energy Research Scientific Computing Center, a DOE Office of Science User Facility supported by the Office of Science of the U.S. Department of Energy under Contract DE-AC02-05CH11231. Computing resources were provided through the ASCR Leadership Computing Challenge (ALCC). The remaining developmental simulations used a high-performance computing cluster provided by the BER Earth System Modeling program and operated by the Laboratory Computing Resource Center at Argonne National Laboratory as well as resources of the Oak Ridge Leadership Computing Facility, which is a DOE Office of Science User Facility supported under Contract DE-AC05-00OR22725. The Pacific Northwest National Laboratory (PNNL) is operated for DOE by Battelle Memorial Institute under Contract DE-AC05-76RLO1830. Oak Ridge National Laboratory (ORNL) is managed by UT-Battelle, LLC, for the U.S. Department of Energy under Contract DE-AC05-00OR22725. The work at Lawrence Livermore National

Data Availability Statement

The E3SM project, code, simulation configurations, model output, and tools to work with the output are described at this site (<https://e3sm.org>). Instructions on how to get started running E3SM are available here (<https://e3sm.org/model/running-e3sm/e3sm-quick-start>). The E3SMv1.1-BGC simulations (default model with CTC land configuration) were conducted with E3SMv1.1.0, which is archived at this site (<https://www.osti.gov/doi/10.1146/annurev-marine-010213-135103>). The E3SMv1.1-ECA simulations were conducted with a version containing minor updates to the ECA configuration, E3SMv1.1.1, which is archived at this site (<https://www.osti.gov/doi/10.1146/annurev-marine-010213-135103>). Model output data are accessible through the DOE Earth System Grid Federation at this site (<https://esgf-node.llnl.gov/projects/e3sm>) under the model names “E3SM-1-1” (i.e., the E3SMv1.1 default model) and “E3SM1-1-ECA”. The full, interactive analysis of the E3SMv1.1 land model using the ILAMB diagnostic tool, and comparison with selected CMIP5 models, is available online at this site (<https://doi.org/10.6084/m9.figshare.11097356.v2>).

References

Alou-Font, E., Mundy, C. J., Roy, S., Gosselin, M., & Agustí, S. (2013). Snow cover affects ice algal pigment composition in the coastal Arctic Ocean during spring.

Anav, A., Friedlingstein, P., Beer, C., Ciais, P., Harper, A., & Jones, C. (2015). Spatiotemporal patterns of terrestrial gross primary production: A review. *Reviews of Geophysics*, *53*, 785–818. <https://doi.org/10.1002/2015RG000483>

Anderson, E. A. (1976). A point energy and mass balance model of a snow cover (NOAA Technical Report NWS): Silver Spring, MD, Office of Hydrology, National Weather Service.

Arora, V. K., Boer, G. J., Friedlingstein, P., Eby, M., Jones, C. D., & Christian, J. R. (2013). Carbon-concentration and carbon-climate feedbacks in CMIP5 Earth system models. *Journal of Climate*, *26*(15), 5289–5314.

Arora, V. K., Katavouta, A., Williams, R. G., Jones, C. D., Brovkin, V., & Friedlingstein, P. (2019). Carbon-concentration and carbon-climate feedbacks in CMIP6 models, and their comparison to CMIP5 models. *Biogeosciences*, *17*, 4173–4222.

Arrigo, K. R. (2014). Sea ice ecosystems. *Annual Review of Marine Science*, *6*(1), 439–467. <https://doi.org/10.1146/annurev-marine-010213-135103>

Arrigo, K. R., & Thomas, D. N. (2004). Large scale importance of sea ice biology in the Southern Ocean. *Antarctic Science*, *16*(4), 471–486.

Arrigo, K. R., van Dijken, G., & Pabi, S. (2008). Impact of a shrinking Arctic ice cover on marine primary production. *Geophysical Research Letters*, *35*, L19603. <https://doi.org/10.1029/2008GL035028>

Batjes, N. H. (1996). Total carbon and nitrogen in the soils of the world. *European Journal of Soil Science*, *65*(1), 10–21.

Beer, C., Reichstein, M., Tomelleri, E., Ciais, P., Jung, M., & Carvalhais, N. (2010). Terrestrial gross carbon dioxide uptake: Global distribution and covariation with climate. *Science*, *329*(5993), 834–838.

Behrenfeld, M. J., & Falkowski, P. G. (1997). Photosynthetic rates derived from satellite-based chlorophyll concentration. *Limnology and Oceanography*, *42*(1), 1–20. <https://doi.org/10.4319/lo.1997.42.1.0001>

Bisht, G., Riley, W. J., Hammond, G. E., & Lorenzetti, D. M. (2018). Development and evaluation of a variably saturated flow model in the global E3SM Land Model (ELM) version 1.0. *Geoscientific Model Development*, *11*(10), 4085–4102.

Bonal, D., Burban, B., Stahl, C., Wagner, F., & Hérault, B. (2016). The response of tropical rainforests to drought—Lessons from recent research and future prospects. *Annals of Forest Science*, *73*(1), 27–44. <https://doi.org/10.1007/s13595-015-0522-5>

Bond-Lamberty, B., Bailey, V. L., Chen, M., Gough, C. M., & Vargas, R. (2018). Globally rising soil heterotrophic respiration over recent decades. *Nature*, *560*(7716), 80.

Boyer, T., Antonov, J. I., Baranova, O. K., Coleman, C., Garcia, H. E., Grodsky, A., & Zweng, M. M. (2013). World ocean database 2013, NOAA Atlas NESDIS 72. <https://doi.org/10.7289/V5NZ85MT>

Burrows, S. M., Ogunro, O., Frossard, A., Russell, L. M., Rasch, P. J., & Elliott, S. (2014). A physically based framework for modeling the organic fractionation of sea spray aerosol from bubble film Langmuir equilibria. *Atmospheric Chemistry & Physics*, *14*(24), 13,601–13,629.

Calvin, K., Patel, P., Clarke, L., Asrar, G., Bond-Lamberty, B., Cui, R. Y., & Wise, M. (2019). GCAM v5.1: representing the linkages between energy, water, land, climate, and economic systems. *Geoscientific Model Development*, *12*(2), 677–698. <https://doi.org/10.5194/gmd-12-677-2019>

Cavalieri, D., Parkinson, C., Gloersen, P., & Zwally, H. J. (1996). Sea ice concentrations from Nimbus-7 SMMR and DMSP SSM/I-SSMIS passive microwave data [1979–2008]: National Snow and Ice Data Center, digital media. Boulder, Colorado, USA, <ftp://sidacs.colorado.edu/DATASETS/NOAA/GO2135/north/daily/data/>, Accessed: 2019-01-30, <https://doi.org/10.5067/8GQ8LZQVL0VL>

Chapin, F. S., Woodwell, G. M., Randerson, J. T., Rastetter, E. B., Lovett, G. M., & Baldocchi, D. D. (2006). Reconciling carbon-cycle concepts, terminology, and methods. *Ecosystems*, *9*(7), 1041–1050.

Chen, M., Rafique, R., Asrar, G. R., Bond-Lamberty, B., Ciais, P., & Zhao, F. (2017). Regional contribution to variability and trends of global gross primary productivity. *Environmental Research Letters*, *12*(10), 105005.

Chen, J., Zhu, Q., Riley, W. J., He, Y., Randerson, J. T., & Trumbore, S. E. (2019). Comparison with global soil radiocarbon observations indicates needed carbon cycle improvements in the E3SM land model. *Journal of Geophysical Research: Biogeosciences*, *124*, 1098–1114. <https://doi.org/10.1029/2018JG004795>

Chhabra, A., & Dadhwal, V. (2004). Assessment of major pools and fluxes of carbon in Indian forests. *Climatic Change*, *64*(3), 341–360.

Ciais, P., Sabine, C., Bala, G., Bopp, L., Brovkin, V., Canadell, J., & Thornton, P. (2013). *Carbon and other biogeochemical cycles*. Cambridge, United Kingdom and New York, NY, USA: Cambridge University Press.

Cleveland, C. C., Townsend, A. R., Schimel, D. S., Fisher, H., Howarth, R. W., Hedin, L. O., & Wasson, M. F. (1999). Global patterns of terrestrial biological nitrogen (N₂) fixation in natural ecosystems. *Global Biogeochemical Cycles*, *13*(2), 623–645. <https://doi.org/10.1029/1999GB900014>

Cleveland, C. C., Townsend, A. R., Taylor, P., Alvarez-Clare, S., Bustamante, M. M., & Chuyong, G. (2011). Relationships among net primary productivity, nutrients and climate in tropical rain forest: A pan-tropical analysis. *Ecology letters*, *14*(9), 939–947.

Laboratory was performed under the auspices of the U.S. Department of Energy under Contract DE-AC52-07NA27344. Los Alamos National Laboratory is operated by Triad National Security, LLC, for the National Nuclear Security Administration of U.S. Department of Energy (Contract 89233218CNA000001).

- Collier, N., Hoffman, F. M., Lawrence, D. M., Keppel-Aleks, G., Koven, C. D., Riley, W. J., & Randerson, J. T. (2018). The International Land Model Benchmarking (ILAMB) system: Design, theory, and implementation. *Journal of Advances in Modeling Earth Systems*, *10*, 2731–2754. <https://doi.org/10.1029/2018MS001354>
- Collins, W. D., Craig, A. P., Truesdale, J. E., Di Vittorio, A. V., Jones, A. D., Bond-Lamberty, B., & Hurtt, G. C. (2015). The integrated Earth system model version 1: Formulation and functionality. *Geoscientific Model Development*, *8*(7), 2203–2219. <https://doi.org/10.5194/gmd-8-2203-2015>
- Conway, T. J., Tans, P. P., Waterman, L. S., Thoning, K. W., Kitzis, D. R., Masarie, K. A., & Zhang, N. (1994). Evidence for interannual variability of the carbon cycle from the National Oceanic and Atmospheric Administration/Climate Monitoring and Diagnostics Laboratory global air sampling network. *Journal of Geophysical Research*, *99*(D11), 22,831–22,855.
- Corlett, R. T. (2016). The impacts of droughts in tropical forests. *Trends in Plant Science*, *21*(7), 584–593.
- Dai, Y., & Zeng, Q. (1997). A land surface model (IAP94) for climate studies part I: Formulation and validation in off-line experiments. *Advances in Atmospheric Sciences*, *14*(4), 433–460.
- Dargaville, R. J., Doney, S. C., & Fung, I. Y. (2003). Inter-annual variability in the interhemispheric atmospheric CO₂ gradient: Contributions from transport and the seasonal rectifier. *Tellus B: Chemical and Physical Meteorology*, *55*(2), 711–722.
- Di Vittorio, A., Chini, L., Bond-Lamberty, B., Mao, J., Shi, X., Truesdale, J., & Thomson, A. (2014). From land use to land cover: Restoring the afforestation signal in a coupled integrated assessment-Earth system model and the implications for CMIP5 RCP simulations. *Biogeosciences*, *11*(22), 6435–6450. <https://doi.org/10.5194/bg-11-6435-2014>
- Di Vittorio, A., Mao, J., Shi, X., Chini, L., Hurtt, G., & Collins, W. (2018). Quantifying the effects of historical land cover conversion uncertainty on global carbon and climate estimates. *Geophysical Research Letters*, *45*, 974–982. <https://doi.org/10.1002/2017GL075124>
- Doney, S. C., Lima, I., Moore, J. K., Lindsay, K., Behrenfeld, M. J., Westberry, T. K., & Takahashi, T. (2009). Skill metrics for confronting global upper ocean ecosystem-biogeochemistry models against field and remote sensing data. *Journal of Marine Systems*, *76*(1–2), 95–112.
- Doney, S. C., Lindsay, K., Fung, I., & John, J. (2006). Natural variability in a stable, 1000-yr global coupled climate-carbon cycle simulation. *Journal of Climate*, *19*(13), 3033–3054.
- Drewniak, B. A. (2019). Simulating dynamic roots in the Energy Exascale Earth System Land Model. *Journal of Advances in Modeling Earth Systems*, *11*, 338–359. <https://doi.org/10.1029/2018MS001334>
- Duarte, P., Meyer, A., Olsen, L. M., Kauko, H. M., Assmy, P., Rsel, A., & Turner, A. K. (2017). Sea ice thermohaline dynamics and biogeochemistry in the Arctic Ocean: Empirical and model results. *Journal of Geophysical Research: Biogeosciences*, *122*, 1632–1654. <https://doi.org/10.1002/2016JG003660>
- Duarte, H. F., Raczka, B. M., Ricciuto, D. M., Lin, J. C., Koven, C. D., Thornton, P. E., & Ehleringer, J. R. (2017). Evaluating the Community Land Model (CLM4.5) at a coniferous forest site in northwestern United States using flux and carbon-isotope measurements. *Biogeosciences*, *14*(18), 4315–4340. <https://doi.org/10.5194/bg-14-4315-2017>
- Dukowicz, J. K., & Baumgardner, J. R. (2000). Incremental remapping as a transport/advection algorithm. *Journal of Computational Physics*, *160*(1), 318–335.
- Erb, K., Kastner, T., Plutzar, C., Bais, A., Carvalhais, N., Fetzel, T., & Pongratz, J. (2018). Unexpectedly large impact of forest management and grazing on global vegetation biomass. *Nature*, *553*(7686), 73.
- Eyring, V., Bony, S., Meehl, G. A., Senior, C. A., Stevens, B., Stouffer, R. J., & Taylor, K. E. (2016). Overview of the Coupled Model Intercomparison Project Phase 6 (CMIP6) experimental design and organization. *Geoscientific Model Development (Online)*, *9*, LLNL-JRNL-736881.
- Fisher, R. A., Muszala, S., Versteinstein, M., Lawrence, P., Xu, C., McDowell, N. G., & Bonan, G. (2015). Taking off the training wheels: The properties of a dynamic vegetation model without climate envelopes, CLM4.5(ED). *Geoscientific Model Development*, *8*(11), 3593–3619. <https://doi.org/10.5194/gmd-8-3593-2015>
- Flanner, M., Liu, X., Zhou, C., Penner, J. E., & Jiao, C. (2012). Enhanced solar energy absorption by internally-mixed black carbon in snow grains. *Atmospheric Chemistry and Physics*, *12*(10), 4699–4721.
- Fleischer, K., Rammig, A., De Kauwe, M. G., Walker, A. P., Domingues, T. F., Fuchslueger, L., et al. (2019). Amazon forest response to CO₂ fertilization dependent on plant phosphorus acquisition. *Nature Geoscience*, *12*(9), 736–741. <https://doi.org/10.1038/s41561-019-0404-9>
- Friedlingstein, P. (2015). Carbon cycle feedbacks and future climate change. *Philosophical Transactions of the Royal Society A: Mathematical, Physical and Engineering Sciences*, *373*(2054), 20140421.
- Friedlingstein, P., Cox, P., Betts, R., Bopp, L., von Bloh, W., & Brovkin, V. (2006). Climate-carbon cycle feedback analysis: Results from the C4MIP model intercomparison. *Journal of Climate*, *19*(14), 3337–3353.
- Friedlingstein, P., Joel, G., Field, C. B., & Fung, I. Y. (1999). Toward an allocation scheme for global terrestrial carbon models. *Global Change Biology*, *5*(7), 755–770. <https://doi.org/10.1046/j.1365-2486.1999.00269.x>
- Friedlingstein, P., Meinshausen, M., Arora, V. K., Jones, C. D., Anav, A., Liddicoat, S. K., & Knutti, R. (2014). Uncertainties in CMIP5 climate projections due to carbon cycle feedbacks. *Journal of Climate*, *27*(2), 511–526.
- Galloway, J. N., Winiwarter, W., Leip, A., Leach, A. M., Bleeker, A., & Erisman, J. W. (2014). Nitrogen footprints: Past, present and future. *Environmental Research Letters*, *9*(11), 115003.
- Gaudio, N., Belyazid, S., Gendre, X., Mansat, A., Nicolas, M., Rizzetto, S., & Probst, A. (2015). Combined effect of atmospheric nitrogen deposition and climate change on temperate forest soil biogeochemistry: A modeling approach. *Ecological Modelling*, *306*, 24–34.
- Gent, P. R., & McWilliams, J. C. (1990). Isopycnal mixing in ocean circulation models. *Journal of Physical Oceanography*, *20*(1), 150–155.
- Gent, P. R., Yeager, S. G., Neale, R. B., Levis, S., & Bailey, D. A. (2010). Improvements in a half degree atmosphere/land version of the CCSM. *Climate Dynamics*, *34*(6), 819–833.
- Girardin, M. P., Bouriaud, O., Hogg, E. H., Kurz, W., Zimmermann, N. E., Metsaranta, J. M., & Bhatti, J. (2016). No growth stimulation of Canada's boreal forest under half-century of combined warming and CO₂ fertilization. *Proceedings of the National Academy of Sciences*, *113*(52), E8406–E8414. <https://doi.org/10.1073/pnas.1610156113>
- Golaz, J. C., Caldwell, P. M., Roedel, L. P. V., Petersen, M. R., Tang, Q., Wolfe, J. D., & Zhu, Q. (2019). The DOE E3SM coupled model version 1: Overview and evaluation at standard resolution. *Journal of Advances in Modeling Earth Systems*, *11*, 2089–2129. <https://doi.org/10.1029/2018MS001603>
- Golaz, J. C., Larson, V. E., & Cotton, W. R. (2002). A PDF-based model for boundary layer clouds. Part I: Method and model description. *Journal of the Atmospheric Sciences*, *59*(24), 3540–3551.
- Goll, D. S., Brovkin, V., Parida, B., Reick, C. H., Kattge, J., Reich, P. B., & Niinemets, Ü. (2012). Nutrient limitation reduces land carbon uptake in simulations with a model of combined carbon, nitrogen and phosphorus cycling. *Biogeosciences*, *9*, 3547–3569.
- Gradinger, R., Iken, K., & Bluhm, B. (2012). BEST ice chlorophyll (chl) 2008. version 1.0. <https://doi.org/10.5065/D6Q23X81>, Accessed Nov 2018.

- Grant, R. F. (2013). Modelling changes in nitrogen cycling to sustain increases in forest productivity under elevated atmospheric CO₂ and contrasting site conditions. *Biogeosciences*, *10*(11), 7703–7721. <https://doi.org/10.5194/bg-10-7703-2013>
- Gregory, J. M., Jones, C., Cadule, P., & Friedlingstein, P. (2009). Quantifying carbon cycle feedbacks. *Journal of Climate*, *22*(19), 5232–5250.
- Gurney, K. R., Law, R. M., Denning, A. S., Rayner, P. J., Baker, D., & Bousquet, P. (2003). TransCom 3 CO₂ inversion intercomparison: 1. Annual mean control results and sensitivity to transport and prior flux information. *Tellus B: Chemical and Physical Meteorology*, *55*(2), 555–579.
- Hales, B. M., & Pronovost, P. J. (2006). The checklist-a tool for error management and performance improvement. *Journal of Critical Care*, *21*(3), 231–235.
- Hawkins, E., & Sutton, R. (2016). Connecting climate model projections of global temperature change with the real world. *Bulletin of the American Meteorological Society*, *97*(6), 963–980.
- Hegglin, M., Kinnison, D., & Lamarque, J. F. (2016). CCM1 nitrogen surface fluxes in support of CMIP6 - version 2.0. Earth System Grid Federation, <https://doi.org/10.22033/ESGF/input4MIPs.1125>
- Hibler III, W. (1979). A dynamic thermodynamic sea ice model. *Journal of Physical Oceanography*, *9*(4), 815–846.
- Hoffman, F. M., Koven, C. D., Keppel-Aleks, G., Lawrence, D. M., Riley, W. J., Randerson, J. T., & Koch, D. (2017). International land model benchmarking (ilamb) 2016 workshop report. DOE/SC-0186, Germantown, Maryland, USA, U.S. Department of Energy, Office of Science, <https://doi.org/10.2172/1330803>
- Hoffman, F., Randerson, J., Arora, V., Bao, Q., Cadule, P., & Ji Obata, A. (2014). Causes and implications of persistent atmospheric carbon dioxide biases in Earth System Models. *Journal of Geophysical Research: Biogeosciences*, *119*, 141–162. <https://doi.org/10.1002/2013JG002381>
- Holm, J. A., Knox, R. G., Zhu, Q., Fisher, R. A., Koven, C. D., Nogueira Lima, A. J., & Chambers, J. Q. (2020). The central amazon biomass sink under current and future atmospheric CO₂: Predictions from big-leaf and demographic vegetation models. *Journal of Geophysical Research: Biogeosciences*, *125*, e2019JG005500. <https://doi.org/10.1029/2019JG005500>
- Holte, J., Talley, L. D., Gilson, J., & Roemmich, D. (2017). An Argo mixed layer climatology and database. *Geophysical Research Letters*, *44*, 5618–5626. <https://doi.org/10.1002/2017GL073426>
- Horner, R. C., & Schrader, G. (1982). Relative contributions of ice algae, phytoplankton, and benthic microalgae to primary production in nearshore regions of the Beaufort Sea. *Arctic*, *35*, 485–503. <https://doi.org/10.14430/arctic2356>
- Houlton, B. Z., Marklein, A. R., & Bai, E. (2015). Representation of nitrogen in climate change forecasts. *Nature Climate Change*, *5*(5), 398–401. <https://doi.org/10.1038/nclimate2538>
- Hsu, J., & Prather, M. J. (2009). Stratospheric variability and tropospheric ozone. *Journal of Geophysical Research*, *114*, D06102. <https://doi.org/10.1029/2008JD010942>
- Huang, Y., Guenet, B., Ciais, P., Janssens, I. A., Soong, J. L., Wang, Y., & Blagodatskaya, E. (2018). ORCHIMIC (v1.0), a microbe-mediated model for soil organic matter decomposition. *Geoscientific Model Development*, *11*, 2111–2138. <https://doi.org/10.5194/gmd-11-2111-2018>
- Hungate, B. A., Dukes, J. S., Shaw, M. R., Luo, Y., & Field, C. B. (2003). Nitrogen and climate change. *Science*, *302*(5650), 1512–1513.
- Hunke, E., Allard, R., Bailey, D. A., Blain, P., Craig, T., Dupont, F., & Winton, M. (2019). CICE-Consortium/Icepack: Icepack1.2.0.
- Hunke, E., & Dukowicz, J. (1997). An elastic–viscous–plastic model for sea ice dynamics. *Journal of Physical Oceanography*, *27*(9), 1849–1867.
- Hunke, E. C., & Dukowicz, J. K. (2002). The elastic–viscous–plastic sea ice dynamics model in general orthogonal curvilinear coordinates on a sphere-Incorporation of metric terms. *Monthly Weather Review*, *130*(7), 1848–1865.
- Hunke, E. C., Lipscomb, W. H., Turner, A. K., Jeffery, N., & Elliott, S. M. (2015). CICE: The Los Alamos sea ice model documentation and software user’s manual 1568 version 5.1: Los Alamos, NM, Los Alamos National Laboratory.
- Hurrell, J. W., Hack, J. J., Shea, D., Caron, J. M., & Rosinski, J. (2008). A new sea surface temperature and sea ice boundary dataset for the community atmosphere model. *Journal of Climate*, *21*(19), 5145–5153. <https://doi.org/10.1175/2008JCLI2292.1>
- Hurrell, J. W., Holland, M. M., Gent, P. R., Ghan, S., Kay, J. E., & Kushner, P. J. (2013). The Community Earth System Model: A framework for collaborative research. *Bulletin of the American Meteorological Society*, *94*(9), 1339–1360.
- Hurttt, G., Chini, L., Sahajpal, R., & Frolking, S. (2017). input4MIPs.UofMD.landState.CMIP.UofMD-landState-2-1-h. <https://doi.org/10.22033/ESGF/input4MIPs.1127>
- Jahnke, R. A. (1992). The phosphorus cycle. *Global Biogeochemical Cycles*, *50*, 301–315.
- Jain, A., Yang, X., Kheshgi, H., McGuire, A. D., Post, W., & Kicklighter, D. (2009). Nitrogen attenuation of terrestrial carbon cycle response to global environmental factors. *Global Biogeochemical Cycles*, *23*, GB4028. <https://doi.org/10.1029/2009GB003519>
- Jeffery, N., & Hunke, E. C. (2014). Modeling the winter-spring transition of first-year ice in the western Weddell Sea. *Journal of Geophysical Research: Oceans*, *119*, 5891–5920. <https://doi.org/10.1002/2013JC009634>
- Jeffery, N., Hunke, E. C., & Elliott, S. M. (2011). Modeling the transport of passive tracers in sea ice. *Journal of Geophysical Research*, *116*, C07020. <https://doi.org/10.1029/2010JC006527>
- Jiang, C., & Ryu, Y. (2016). Multi-scale evaluation of global gross primary productivity and evapotranspiration products derived from Breathing Earth System Simulator (BESS). *Remote Sensing of Environment*, *186*, 528–547.
- Jobbgy, E. G., & Jackson, R. B. (2001). The distribution of soil nutrients with depth: Global patterns and the imprint of plants. *Biogeochemistry*, *53*(1), 51–77.
- Joiner, J., Yoshida, Y., Zhang, Y., Duveiller, G., Jung, M., Lyapustin, A., & Tucker, C. (2018). Estimation of terrestrial global gross primary production (gpp) with satellite data-driven models and eddy covariance flux data. *Remote Sensing*, *10*, 1346.
- Jones, C. D., Arora, V., Friedlingstein, P., Bopp, L., Brovkin, V., Dunne, J., & Zaehle, S. (2016). C4MIP—The Coupled Climate–Carbon Cycle Model Intercomparison Project: Experimental Protocol for CMIP6. *Geoscientific Model Development*, *9*(8), 2853–2880. <https://doi.org/10.5194/gmd-9-2853-2016>
- Jones, A. D., Calvin, K. V., Shi, X., Di Vittorio, A. V., Bond-Lamberty, B., Thornton, P. E., & Collins, W. D. (2018). Quantifying human-mediated carbon cycle feedbacks. *Geophysical Research Letters*, *45*, 11,370–11,379. <https://doi.org/10.1029/2018GL079350>
- Jones, P. D., New, M., Parker, D. E., Martin, S., & Rigor, I. G. (1999). Surface air temperature and its changes over the past 150 years. *Reviews of Geophysics*, *37*(2), 173–199.
- Jordan, R. (1991). A one-dimensional temperature model for a snow cover: Technical documentation for sntherm.89 (*Special Report 91-16*). Hanover, New Hampshire: U.S. Army Cold Regions Research and Engineering Laboratory.
- Jung, M., Reichstein, M., Margolis, H. A., Cescatti, A., Richardson, A. D., & Arain, M. A. (2011). Global patterns of land-atmosphere fluxes of carbon dioxide, latent heat, and sensible heat derived from eddy covariance, satellite, and meteorological observations. *Journal of Geophysical Research*, *116*, G00J07. <https://doi.org/10.1029/2010JG001566>

- Kattge, J., Diaz, S., Lavorel, S., Prentice, C., Leadley, P., Bonisch, G., & Wirth, C. (2011). TRY—A global database of plant traits. *Global Change Biology*, *17*(9), 2905–2935. <https://doi.org/10.5194/gmd-9-2853-2016>
- Keppel-Aleks, G., Wolf, A. S., Mu, M., Doney, S. C., Morton, D. C., Kasibhatla, P. S., & Randerson, J. T. (2014). Separating the influence of temperature, drought, and fire on interannual variability in atmospheric CO₂. *Global Biogeochemical Cycles*, *28*, 1295–1310. <https://doi.org/10.1002/2014GB004890>
- Khatiwal, S., Tanhua, T., Mikaloff Fletcher, S., Gerber, M., Doney, S., & Graven, H. (2013). Global ocean storage of anthropogenic carbon. *Biogeosciences*, *10*(4), 2169–2191.
- Köchy, M., Hiederer, R., & Freibauer, A. (2015). Global distribution of soil organic carbon—Part 1: Masses and frequency distributions of SOC stocks for the tropics, permafrost regions, wetlands, and the world. *Soil*, *1*(1), 351–365.
- Kooperman, G. J., Chen, Y., Hoffman, F. M., Koven, C. D., Lindsay, K., Pritchard, M. S., & Randerson, J. T. (2018). Forest response to rising CO₂ drives zonally asymmetric rainfall change over tropical land. *Nature Climate Change*, *8*, 434–440.
- Koven, C. D., Lawrence, D. M., & Riley, W. J. (2015). Permafrost carbon-climate feedback is sensitive to deep soil carbon decomposability but not deep soil nitrogen dynamics. *Proceedings of the National Academy of Sciences*, *112*(12), 3752–3757.
- Koven, C., Riley, W., Subin, Z., Tang, J., Torn, M., Collins, W., & Swenson, S. (2013). The effect of vertically resolved soil biogeochemistry and alternate soil C and N models on C dynamics of CLM4. *Biogeosciences*, *10*(11), 7109.
- Krishnamurthy, A., Moore, J. K., Mahowald, N., Luo, C., Doney, S. C., Lindsay, K., & Zender, C. S. (2009). Impacts of increasing anthropogenic soluble iron and nitrogen deposition on ocean biogeochemistry. *Global Biogeochemical Cycles*, *23*, GB3016. <https://doi.org/10.1029/2008GB003440>
- Kuzyakov, Y., & Xu, X. (2013). Competition between roots and microorganisms for nitrogen: mechanisms and ecological relevance. *New Phytologist*, *198*(3), 656–669.
- Lamarque, J. F., Bond, T. C., Eyring, V., Granier, C., Heil, A., Klimont, Z., & van Vuuren, D. P. (2010). Historical (1850–2000) gridded anthropogenic and biomass burning emissions of reactive gases and aerosols: Methodology and application. *Atmospheric Chemistry and Physics*, *10*(15), 7017–7039. <https://doi.org/10.5194/acp-10-7017-2010>
- Landschützer, P., Gruber, N., & Bakker, D. C. E. (2017). An observation-based global monthly gridded sea surface pCO₂ product from 1982 onward and its monthly climatology (NCIE Accession 0160558). Silver Spring, MD, <https://doi.org/10.7289/v5z899n6>
- Lannuzel, D., Schoemann, V., Dumont, I., Content, M., de Jong, J., Tison, J. L., & Becquevort, S. (2013). Effect of melting Antarctic sea ice on the fate of microbial communities studied in microcosms. *Polar Biology*, *36*(10), 1483–1497. <https://doi.org/10.1007/s00300-013-1368-7>
- Larson, V. E. (2017). CLUBB-SILHS: A parameterization of subgrid variability in the atmosphere. arXiv preprint arXiv:1711.03675.
- Larson, V. E., & Golaz, J. C. (2005). Using probability density functions to derive consistent closure relationships among higher-order moments. *Monthly Weather Review*, *133*(4), 1023–1042.
- Law, R., Rayner, P., Denning, A., Erickson, D., Fung, I., & Heimann, M. (1996). Variations in modeled atmospheric transport of carbon dioxide and the consequences for CO₂ inversions. *Global Biogeochemical Cycles*, *10*(4), 783–796.
- Law, B. E., Sun, O., Campbell, J., Van Tuyl, S., & Thornton, P. E. (2003). Changes in carbon storage and fluxes in a chronosequence of ponderosa pine. *Global Change Biology*, *9*(4), 510–524.
- Law, B. E., Thornton, P. E., Irvine, J., Anthoni, P. M., & Van Tuyl, S. (2001). Carbon storage and fluxes in ponderosa pine forests at different developmental stages. *Global Change Biology*, *7*(7), 755–777.
- Lawrence, P. J., & Chase, T. N. (2007). Representing a new MODIS consistent land surface in the Community Land Model (CLM 3.0). *Journal of Geophysical Research*, *112*, G01023. <https://doi.org/10.1029/2006JG000168>
- Le Quéré, C., Andrew, R. M., Friedlingstein, P., Sitch, S., Hauck, J., Pongratz, J., & Zheng, B. (2018). Global carbon budget 2018. *Earth System Science Data*, *10*(4), 2141–2194. <https://doi.org/10.5194/essd-10-2141-2018>
- Lee, H. S., Whitley, T., & Kang, S. H. (2008). Spring time production of bottom ice algae in the landfast sea ice zone at Barrow, Alaska. *Journal of Experimental Marine Biology and Ecology*, *367*, 204–212. <https://doi.org/10.1016/j.jembe.2008.09.018>
- Leng, G., Leung, L. R., & Huang, M. (2017). Significant impacts of irrigation water sources and methods on modeling irrigation effects in the ACME Land Model. *Journal of Advances in Modeling Earth Systems*, *9*, 1665–1683. <https://doi.org/10.1002/2016MS000885>
- Levis, S., Bonan, G. B., Kluzek, E., Thornton, P. E., Jones, A., Sacks, W. J., & Kucharik, C. J. (2012). Interactive crop management in the community earth system model (CESM1): Seasonal influences on land-atmosphere fluxes. *Journal of Climate*, *25*(14), 4839–4859. <https://doi.org/10.1175/JCLI-D-11-00446.1>
- Li, W., Ciais, P., Yue, C., Gasser, T., Peng, S., & Bastos, A. (2018). Gross changes in forest area shape the future carbon balance of tropical forests. *Biogeosciences*, *15*(1), 91–103. <https://doi.org/10.5194/bg-15-91-2018>
- Li, H. Y., Leung, L. R., Getirana, A., Huang, M., Wu, H., Xu, Y., & Voisin, N. (2015). Evaluating global streamflow simulations by a physically based routing model coupled with the community land model. *Journal of Hydrometeorology*, *16*(2), 948–971.
- Li, F., Levis, S., & Ward, D. S. (2013). Quantifying the role of fire in the Earth system—Part 1: Improved global fire modeling in the Community Earth System Model (CESM1). *Biogeosciences*, *10*(4), 2293–2314. <https://doi.org/10.5194/bg-10-2293-2013>
- Li, H. Y., Ruby Leung, L., Tesfa, T., Voisin, N., Hejazi, M., Liu, L., & Yang, X. (2015). Modeling stream temperature in the Anthropocene: An Earth system modeling approach. *Journal of Advances in Modeling Earth Systems*, *7*, 1661–1679. <https://doi.org/10.1002/2015MS000471>
- Li, H., Wigmosta, M. S., Wu, H., Huang, M., Ke, Y., Coleman, A. M., & Leung, L. R. (2013). A physically based runoff routing model for land surface and earth system models. *Journal of Hydrometeorology*, *14*(3), 808–828.
- Li, F., Zeng, X., & Levis, S. (2012a). Corrigendum to “A process-based fire parameterization of intermediate complexity in a Dynamic Global Vegetation Model” published in *Biogeosciences*, *9*, 2761–2780, 2012. *Biogeosciences*, *9*(11), 4771–4772.
- Li, F., Zeng, X., & Levis, S. (2012b). A process-based fire parameterization of intermediate complexity in a Dynamic Global Vegetation Model. *Biogeosciences*, *9*(7), 2761–2780.
- Lin, B. L., Sakoda, A., Shibasaki, R., Goto, N., & Suzuki, M. (2000). Modelling a global biogeochemical nitrogen cycle in terrestrial ecosystems. *Ecological Modelling*, *135*(1), 89–110.
- Lindsay, K., Bonan, G. B., Doney, S. C., Hoffman, F. M., Lawrence, D. M., Long, M. C., & Thornton, P. E. (2014). Preindustrial-control and twentieth-century carbon cycle experiments with the Earth System Model CESM1 (BGC). *Journal of Climate*, *27*(24), 8981–9005.
- Lipscomb, W. H., & Hunke, E. C. (2004). Modeling sea ice transport using incremental remapping. *Monthly Weather Review*, *132*(6), 1341–1354.
- Lipscomb, W. H., & Ringler, T. D. (2005). An incremental remapping transport scheme on a spherical geodesic grid. *Monthly Weather Review*, *133*(8), 2335–2350.
- Liu, X., Easter, R. C., Ghan, S. J., Zaveri, R., Rasch, P., Shi, X., & Mitchell, D. (2012). Toward a minimal representation of aerosols in climate models: Description and evaluation in the Community Atmosphere Model CAM5. *Geoscientific Model Development*, *5*(3), 709–739. <https://doi.org/10.5194/gmd-5-709-2012>

- Liu, X., Ma, P.-L., Wang, H., Tilmes, S., Singh, B., Easter, R. C., et al. (2016). Description and evaluation of a new four-mode version of the Modal Aerosol Module (MAM4) within version 5.3 of the Community Atmosphere Model. *Geoscientific Model Development*, 9(2), 505–522. <https://doi.org/10.5194/gmd-9-505-2016>
- Luo, C., Mahowald, N. M., & del Corral, J. (2003). Sensitivity study of meteorological parameters on mineral aerosol mobilization, transport, and distribution. *Journal of Geophysical Research*, 108(D15), 4447. <https://doi.org/10.1029/2003JD003483>
- Luo, Y., Su, B., Currie, W., Dukes, J., Finzi, A., Hartwig, U., & Pataki, D. (2004). Progressive nitrogen limitation of ecosystem responses to rising atmospheric carbon dioxide. *Bioscience*, 54(8), 731–739.
- Ma, S., Tao, Z., Yang, X., Yu, Y., Zhou, X., Ma, W., & Li, Z. (2014). Estimation of marine primary productivity from satellite-derived phytoplankton absorption data. *IEEE Journal of Selected Topics in Applied Earth Observations and Remote Sensing*, 7(7), 3084–3092. <https://doi.org/10.1109/JSTARS.2014.2298863>
- Mahowald, N. M., Muhs, D. R., Levis, S., Rasch, P. J., Yoshioka, M., Zender, C. S., & Luo, C. (2006). Change in atmospheric mineral aerosols in response to climate: Last glacial period, preindustrial, modern, and doubled carbon dioxide climates. *Journal of Geophysical Research*, 111, D10202. <https://doi.org/10.1029/2005JD006653>
- Mao, J., Ricciuto, D. M., Thornton, P. E., Warren, J. M., King, A. W., Shi, X., & Norby, R. J. (2016). Evaluating the Community Land Model in a pine stand with shading manipulations and ¹³CO₂ labeling. *Biogeosciences*, 13(3), 641–657. <https://doi.org/10.5194/bg-13-641-2016>
- Massom, R. A., Stammerjohn, S. E., Smith, R. C., Pook, M. J., Iannuzzi, R. A., Adams, N., & Krouse, H. R. (2006). Extreme anomalous atmospheric circulation in the west antarctic peninsula region in austral spring and summer 2001/02, and its profound impact on sea ice and biota. *Journal of Climate*, 19(15), 3544–3571. <https://doi.org/10.1175/JCLI3805.1>
- Matthews, E. (1997). Global litter production, pools, and turnover times: Estimates from measurement data and regression models. *Journal of Geophysical Research*, 102(D15), 18,771–18,800.
- Mayorga, E., Seitzinger, S. P., Harrison, J. A., Dumont, E., Beusen, A. H., Bouwman, A., & Dreht, G. V. (2010). Global nutrient export from watersheds 2 (NEWS 2): Model development and implementation. *Environmental Modelling & Software*, 25(7), 837–853. <https://doi.org/10.1016/j.envsoft.2010.01.007>
- Medvigy, D., Wang, G., Zhu, Q., Riley, W. J., Trielweiler, A., Waring, B., et al. (2019). Observed variation in soil properties can drive large variation in forest functioning and composition during tropical forest secondary succession. *New Phytologist*, 223, 1820–1833. <https://doi.org/10.1111/nph.15848>
- Meiners, K. (2013). ASPeCt-Bio: Chlorophyll a in Antarctic sea ice from historical ice core dataset Australian Antarctic Data Centre - CAASM Metadata. <https://data.aad.gov.au/metadata/records/ASPeCt-Bio>, updated 2017.
- Melillo, J., Steudler, P., Aber, J., Newkirk, K., Lux, H., Bowles, F., & Morrisseau, S. (2002). Soil warming and carbon-cycle feedbacks to the climate system. *Science*, 298(5601), 2173–2176.
- Metcalfe, D. B., Ricciuto, D., Palmroth, S., Campbell, C., Hurry, V., Mao, J., & Oren, R. (2017). Informing climate models with rapid chamber measurements of forest carbon uptake. *Global Change Biology*, 23(5), 2130–2139. <https://doi.org/10.1111/gcb.13451>
- Moore, J. K., & Braucher, O. (2008). Sedimentary and mineral dust sources of dissolved iron to the world ocean. *Biogeosciences*, 5(3), 631–656.
- Moore, J. K., Doney, S. C., Kleypas, J. A., Glover, D. M., & Fung, I. Y. (2001). An intermediate complexity marine ecosystem model for the global domain. *Deep Sea Research Part II: Topical Studies in Oceanography*, 49(1–3), 403–462.
- Moore, J. K., Doney, S. C., & Lindsay, K. (2004). Upper ocean ecosystem dynamics and iron cycling in a global three-dimensional model. *Global Biogeochemical Cycles*, 18, GB4028. <https://doi.org/10.1029/2004GB002220>
- Moore, J. K., Lindsay, K., Doney, S. C., Long, M. C., & Misumi, K. (2013). Marine ecosystem dynamics and biogeochemical cycling in the Community Earth System Model [CESM1(BGC)]: Comparison of the 1990s with the 2090s under the RCP4.5 and RCP8.5 scenarios. *Journal of Climate*, 26(23), 9291–9312. <https://doi.org/10.1175/JCLI-D-12-00566.1>
- Neale, R. B., Gettelman, A., Park, S., Conley, A. J., Kinnison, D., Marsh, D., & Rasch, P. J. (2012). Description of the NCAR Community Atmosphere Model (CAM5.0) (NCAR/TN-486+STR). Boulder, Colorado: National Center for Atmospheric Research. https://www.cesm.ucar.edu/models/cesm1.0/cam/docs/description/cam5_desc.pdf
- Nevison, C. D., Mahowald, N. M., Doney, S. C., Lima, I. D., Van der Werf, G. R., Randerson, J. T., & McKinley, G. A. (2008). Contribution of ocean, fossil fuel, land biosphere, and biomass burning carbon fluxes to seasonal and interannual variability in atmospheric CO₂. *Journal of Geophysical Research*, 113, G01010. <https://doi.org/10.1029/2007JG000408>
- O'Neill, B. C., Tebaldi, C., van Vuuren, D. P., Eyring, V., Friedlingstein, P., Hurtt, G., & Sanderson, B. M. (2016). The scenario model intercomparison project (scenariomip) for CMIP6. *Geoscientific Model Development*, 9(9), 3461–3482. <https://doi.org/10.5194/gmd-9-3461-2016>
- Oleson, K. W., Lawrence, D. M., Bonan, G. B., Drewniak, B., Huang, M., Koven, C. D., & Yang, Z. L. (2013). Technical description of version 4.5 of the Community Land Model (CLM) (NCAR Technical Note NCAR/TN-503+STR). Boulder, CO: National Center for Atmospheric Research. <https://doi.org/10.5065/D6RR1W7M>
- Oleson, K. W., Lawrence, D. M., Bonan, G. B., Flanner, M. G., Kluzek, E., Lawrence, P. J., & Thornton, P. E. (2010). Technical description of version 4.0 of the Community Land Model (cLM) (NCAR Technical Note NCAR/TN-478+STR). Boulder, CO: National Center for Atmospheric Research. <https://doi.org/10.5065/D6FB50WZ>
- Pan, Y., Birdsey, R. A., Fang, J., Houghton, R., Kauppi, P. E., & Kurz, W. A. (2011). A large and persistent carbon sink in the world's forests. *Science*, 333(6045), 988–993.
- Paterson, N. H., & Laybourn-Parry, J. (2012). Sea ice microbial dynamics over an annual cycle in Prydz Bay, Antarctica. *Polar Biology*, 35, 993–1002. <https://doi.org/10.1007/s00300-011-1146-3>
- Peñuelas, J., Ciais, P., Canadell, J. G., Janssens, I. A., Fernández-Martínez, M., Carnicer, J., & Sardans, J. (2017). Shifting from a fertilization-dominated to a warming-dominated period. *Nature Ecology & Evolution*, 1(10), 1438.
- Petersen, M. R., Jacobsen, D. W., Ringler, T. D., Hecht, M. W., & Maltrud, M. E. (2015). Evaluation of the arbitrary Lagrangian–Eulerian vertical coordinate method in the MPAS-Ocean model. *Ocean Modelling*, 86, 93–113.
- Post, W. M., Pastor, J., Zinke, P. J., & Stangenberger, A. G. (1985). Global patterns of soil nitrogen storage. *Nature*, 317(6038), 613.
- Poulter, B., Heyder, U., & Cramer, W. (2009). Modeling the sensitivity of the seasonal cycle of gpp to dynamic lai and soil depths in tropical rainforests. *Ecosystems*, 12(4), 517–533. <https://doi.org/10.1007/s10021-009-9238-4>
- Pries, C. E. H., Castanha, C., Porras, R., & Torn, M. (2017). The whole-soil carbon flux in response to warming. *Science*, 355(6332), 1420–1423.
- Project, J. M. M. (2010). GHRSSST level 4 MUR global foundation sea surface temperature analysis. <https://doi.org/10.5067/GHGMR-4FJ01>, CA, USA, Ver. 2. PO.DAAC.

- Qian, Y., Wan, H., Yang, B., Golaz, J. C., Harrop, B., & Hou, Z. (2018). Parametric sensitivity and uncertainty quantification in the version 1 of E3SM atmosphere model based on short perturbed parameter ensemble simulations. *Journal of Geophysical Research: Atmospheres*, *123*, 13,046–13,073. <https://doi.org/10.1029/2018JD028927>
- Raczka, B., Duarte, H. F., Koven, C. D., Ricciuto, D., Thornton, P. E., Lin, J. C., & Bowling, D. R. (2016). An observational constraint on stomatal function in forests: Evaluating coupled carbon and water vapor exchange with carbon isotopes in the Community Land Model (CLM4.5). *Biogeosciences*, *13*(18), 5183–5204. <https://doi.org/10.5194/bg-13-5183-2016>
- Rasch, P. J., Xie, S., Ma, P. L., Lin, W., Wang, H., Tang, Q., & Yang, Y. (2019). An overview of the atmospheric component of the Energy Exascale Earth System Model. *Journal of Advances in Modeling Earth Systems*, *11*, 2377–2411. <https://doi.org/10.1029/2019MS001629>
- Reckinger, S. M., Petersen, M. R., & Reckinger, S. J. (2015). A study of overflow simulations using MPAS-Ocean: Vertical grids, resolution, and viscosity. *Ocean Modelling*, *96*, 291–313.
- Ricciuto, D., Sargsyan, K., & Thornton, P. (2018). The impact of parametric uncertainties on biogeochemistry in the E3SM land model. *Journal of Advances in Modeling Earth Systems*, *10*, 297–319. <https://doi.org/10.1002/2017MS000962>
- Rienecker, M. M., Suarez, M. J., Gelaro, R., Todling, R., Bacmeister, J., & Liu, E. (2011). MERRA: NASA's modern-era retrospective analysis for research and applications. *Journal of Climate*, *24*(14), 3624–3648.
- Riley, W., Subin, Z., Lawrence, D., Swenson, S., Torn, M., Meng, L., & Hess, P. (2011). Barriers to predicting changes in global terrestrial methane fluxes: Analyses using CLM4Me, a methane biogeochemistry model integrated in CESM. *Biogeosciences*, *8*(7), 1925–1953.
- Riley, W. J., Zhu, Q., & Tang, J. (2018). Weaker land–climate feedbacks from nutrient uptake during photosynthesis-inactive periods. *Nature Climate Change*, *8*(11), 1002.
- Ringler, T., Petersen, M., Higdon, R. L., Jacobsen, D., Jones, P. W., & Maltrud, M. (2013). A multi-resolution approach to global ocean modeling. *Ocean Modelling*, *69*, 211–232.
- Roberts, A. F., Hunke, E. C., Allard, R., Bailey, D. A., Craig, A. P., Lemieux, J. F., & Turner, M. D. (2018). Quality control for community-based sea-ice model development. *Philosophical Transactions of the Royal Society A: Mathematical, Physical and Engineering Sciences*, *376*(2129), 20170344.
- Sayer, E. J., Powers, J. S., & Tanner, E. V. (2007). Increased litterfall in tropical forests boosts the transfer of soil CO₂ to the atmosphere. *PLoS One*, *2*(12), e1299.
- Schimmel, J. P., Jackson, L. E., & Firestone, M. K. (1989). Spatial and temporal effects on plant microbial competition for inorganic nitrogen in a California annual grassland. *Soil Biology & Biochemistry*, *21*(8), 1059–1066. [https://doi.org/10.1016/0038-0717\(89\)90044-8](https://doi.org/10.1016/0038-0717(89)90044-8)
- Sharpe, P. J. H., & Rykiel, E. J. (1991). Modelling integrated response of plants to multiple stresses. In H. Mooney, W. Winner, E. Pell (Eds.), *Response of Plants to Multiple Stresses* pp. 205–224. San Diego, CA: Academic Press.
- Shrivastava, M., Easter, R. C., Liu, X., Zelenyuk, A., Singh, B., Zhang, K., & Tiitta, P. (2015). Global transformation and fate of SOA: Implications of low-volatility SOA and gas-phase fragmentation reactions. *Journal of Geophysical Research: Atmospheres*, *120*, 4169–4195. <https://doi.org/10.1002/2014JD022563>
- Skamarock, W. C., & Gassmann, A. (2011). Conservative transport schemes for spherical geodesic grids: High-order flux operators for ODE-based time integration. *Monthly Weather Review*, *139*(9), 2962–2975.
- Smil, V. (2000). Phosphorus in the environment: Natural flows and human interferences. *Annual Review of Energy and the Environment*, *25*(1), 53–88.
- Smith, R., Jones, P., Briegleb, B., Bryan, F., Danabasoglu, G., Dennis, J., & Yeager, S. (2010). The parallel ocean program reference manual: Ocean component of the Community Climate System Model (CCSM) and Community Earth System Model (CESM) (LAUR-10-01853). Los Alamos, NM: Los Alamos National Laboratory. Retrieved from www.cesm.ucar.edu/models/cesm1.0/pop2/doc/sci/POPRefManual.pdf
- Sokolov, A. P., Kicklighter, D. W., Melillo, J. M., Felzer, B. S., Schlosser, C. A., & Cronin, T. W. (2008). Consequences of considering carbon–nitrogen interactions on the feedbacks between climate and the terrestrial carbon cycle. *Journal of Climate*, *21*(15), 3776–3796.
- Subin, Z. M., Riley, W. J., & Mironov, D. (2012). An improved lake model for climate simulations: Model structure, evaluation, and sensitivity analyses in CESM1. *Journal of Advances in Modeling Earth Systems*, *4*, M02001. <https://doi.org/10.1029/2011MS000072>
- Sulla-Menashe, D., Woodcock, C. E., & Friedl, M. A. (2018). Canadian boreal forest greening and browning trends: An analysis of biogeographic patterns and the relative roles of disturbance versus climate drivers. *Environmental Research Letters*, *13*(1), 14,007. <https://doi.org/10.1088/1748-9326/aa9b88>
- Swann, A. L., Fung, I. Y., Levis, S., Bonan, G. B., & Doney, S. C. (2010). Changes in Arctic vegetation amplify high-latitude warming through the greenhouse effect. *Proceedings of the National Academy of Sciences*, *107*(4), 1295–1300. <https://doi.org/10.1073/pnas.0913846107>
- Takala, M., Luojus, K., Pulliainen, J., Derksen, C., Lemmetyinen, J., Kärnä, J. P., & Bojkov, B. (2011). Estimating northern hemisphere snow water equivalent for climate research through assimilation of space-borne radiometer data and ground-based measurements. *Remote Sensing of Environment*, *115*(12), 3517–3529.
- Tan, Z., Leung, L. R., Li, H. Y., & Tesfa, T. (2018). Modeling sediment yield in land surface and earth system models: Model comparison, development, and evaluation. *Journal of Advances in Modeling Earth Systems*, *10*, 2192–2213. <https://doi.org/10.1029/2017MS001270>
- Tan, Z., Leung, L. R., Li, H., Tesfa, T., Vanmaercke, M., Poesen, J., & Hartmann, J. (2017). A global data analysis for representing sediment and particulate organic carbon yield in Earth System Models. *Water Resources Research*, *53*, 10,674–10,700. <https://doi.org/10.1002/2017WR020806>
- Tang, J. Y. (2015). On the relationships between the Michaelis-Menten kinetics, reverse Michaelis-Menten kinetics, equilibrium chemistry approximation kinetics, and quadratic kinetics. *Geoscientific Model Development*, *8*(12), 3823–3835. <https://doi.org/10.5194/gmd-8-3823-2015>
- Tang, J. Y., & Riley, W. J. (2013). A total quasi-steady-state formulation of substrate uptake kinetics in complex networks and an example application to microbial litter decomposition. *Biogeosciences*, *10*(12), 8329–8351. <https://doi.org/10.5194/bg-10-8329-2013>
- Tang, J. Y., & Riley, W. J. (2018). Predicted land carbon dynamics are strongly dependent on the numerical coupling of nitrogen mobilizing and immobilizing processes: A demonstration with the e3sm land model. *Earth Interactions*, *22*(11), 1–18. <https://doi.org/10.1175/EI-D-17-0023.1>
- Taylor, K. E., Stouffer, R. J., & Meehl, G. A. (2012). An overview of cmip5 and the experiment design. *Bulletin of the American Meteorological Society*, *93*(4), 485–498. <https://doi.org/10.1175/BAMS-D-11-00094.1>
- Tesfa, T. K., & Leung, L. Y. R. (2017). Exploring new topography-based subgrid spatial structures for improving land surface modeling. *Geoscientific Model Development (Online)*, *10*, PNNL-SA-118783.
- Thornton, P. E., Calvin, K., Jones, A. D., Di Vittorio, A. A. V., Bond-Lamberty, B., Chini, L., & Hurtt, G. (2017). Biospheric feedback effects in a synchronously coupled model of human and Earth systems. *Nature Climate Change*, *7*(7), 496–500. <https://doi.org/10.1038/nclimate3310>

- Thornton, P. E., Doney, S. C., Lindsay, K., Moore, J. K., Mahowald, N., Randerson, J. T., & Lee, Y. H. (2009). Carbon-nitrogen interactions regulate climate-carbon cycle feedbacks: Results from an atmosphere-ocean general circulation model. *Biogeosciences*, *6*(10), 2099–2120.
- Thornton, P. E., Lamarque, J. F., Rosenbloom, N. A., & Mahowald, N. M. (2007). Influence of carbon-nitrogen cycle coupling on land model response to CO₂ fertilization and climate variability. *Global Biogeochemical Cycles*, *21*, GB4018. <https://doi.org/10.1029/2006GB002868>
- Thornton, P. E., Law, B. E., Gholz, H. L., Clark, K. L., Falge, E., & Kallus, D. S. (2002). Modeling and measuring the effects of disturbance history and climate on carbon and water budgets in evergreen needleleaf forests. *Agricultural and Forest Meteorology*, *113*(1–4), 185–222.
- Thornton, P. E., & Rosenbloom, N. A. (2005). Ecosystem model spin-up: Estimating steady state conditions in a coupled terrestrial carbon and nitrogen cycle model. *Ecological Modelling*, *189*(1–2), 25–48.
- Todd-Brown, K., Randerson, J., Post, W., Hoffman, F., Tarnocai, C., Schuur, E., & Allison, S. (2013). Causes of variation in soil carbon simulations from CMIP5 Earth system models and comparison with observations. *Biogeosciences*, *10*, 1717–1736.
- Turner, A. K., & Hunke, E. C. (2015). Impacts of a mushy-layer thermodynamic approach in global sea-ice simulations using the CICE sea-ice model. *Journal of Geophysical Research: Oceans*, *120*, 1253–1275. <https://doi.org/10.1002/2014JC010358>
- Van Roekel, L., Adcroft, A. J., Danabasoglu, G., Griffies, S. M., Kauffman, B., Large, W., & Schmidt, M. (2018). The KPP boundary layer scheme for the ocean: Revisiting its formulation and benchmarking one-dimensional simulations relative to IES. *Journal of Advances in Modeling Earth Systems*, *10*, 2647–2685. <https://doi.org/10.1029/2018MS001336>
- van der Wal, A., de Boer, W., Lubbers, I. M., & van Veen, J. A. (2007). Concentration and vertical distribution of total soil phosphorus in relation to time of abandonment of arable fields. *Nutrient Cycling in Agroecosystems*, *79*(1), 73–79.
- Vaughan, R. E., Needelman, B. A., Kleinman, P. J., & Allen, A. L. (2007). Vertical distribution of phosphorus in agricultural drainage ditch soils. *Journal of Environmental Quality*, *36*(6), 1895–1903.
- Vitousek, P. M., & Howarth, R. W. (1991). Nitrogen limitation on land and in the sea: How can it occur? *Biogeochemistry*, *13*(2), 87–115.
- Vitousek, P. M., Menge, D. N., Reed, S. C., & Cleveland, C. C. (2013). Biological nitrogen fixation: Rates, patterns and ecological controls in terrestrial ecosystems. *Philosophical Transactions of the Royal Society B: Biological Sciences*, *368*(1621), 20130119.
- Voisin, N., Li, H., Ward, D., Huang, M., Wigmosta, M., & Leung, L. (2013). On an improved sub-regional water resources management representation for integration into earth system models. *Hydrology and Earth System Sciences*, *17*(9), 3605–3622.
- Voisin, N., Liu, L., Hejazi, M., Tesfa, T., Li, H., Huang, M., & Leung, L. (2013). One-way coupling of an integrated assessment model and a water resources model: Evaluation and implications of future changes over the US Midwest. *Hydrology and Earth System Sciences*, *17*(11), 4555–4575.
- Wang, Y., Ciais, P., Goll, D., Huang, Y., Luo, Y., Wang, Y. P., & Zechmeister-Boltenstern, S. (2018). GOLUM-CNP v1.0: A data-driven modeling of carbon, nitrogen and phosphorus cycles in major terrestrial biomes. *Geoscientific Model Development*, *11*(9), 3903–3928. <https://doi.org/10.5194/gmd-11-3903-2018>
- Wang, H., Easter, R. C., Rasch, P. J., Wang, M., Liu, X., Ghan, S. J., et al. (2013). Sensitivity of remote aerosol distributions to representation of cloud-aerosol interactions in a global climate model. *Geoscientific Model Development*, *6*(3), 765–782. <https://doi.org/10.5194/gmd-6-765-2013>
- Wang, H., Easter, R. C., Zhang, R., Ma, P.-L., Singh, B., Zhang, K., et al. (2020). Aerosols in the E3SM Version 1: New developments and their impacts on radiative forcing. *Journal of Advances in Modeling Earth Systems*, *12*, e2019MS001851. <https://doi.org/10.1029/2019MS001851>
- Wang, S., Elliott, S., Maltrud, M., & Cameron-Smith, P. (2015). Influence of explicit Phaeocystis parameterizations on the global distribution of marine dimethyl sulfide. *Journal of Geophysical Research: Biogeosciences*, *120*, 2158–2177. <https://doi.org/10.1002/2015JG003017>
- Wang, Y. P., Law, R. M., & Pak, B. (2010a). A global model of carbon, nitrogen and phosphorus cycles for the terrestrial biosphere. *Biogeosciences*, *7*(7), 2261–2282.
- Wang, Y. P., Law, R. M., & Pak, B. (2010b). A global model of carbon, nitrogen and phosphorus cycles for the terrestrial biosphere. *Biogeosciences*, *7*(7), 2261–2282. <https://doi.org/10.5194/bg-7-2261-2010>
- Wang, S., Maltrud, M., Burrows, S., Elliott, S., & Cameron-Smith, P. (2018). Impacts of shifts in phytoplankton community on clouds and climate via the sulfur cycle. *Global Biogeochemical Cycles*, *32*, 1005–1026. <https://doi.org/10.1029/2017GB005862>
- Wang, S., & Moore, J. K. (2011). Incorporating Phaeocystis into a Southern Ocean ecosystem model. *Journal of Geophysical Research*, *116*, C01019. <https://doi.org/10.1029/2009JC005817>
- Welp, L. R., Keeling, R. F., Meijer, H. A., Bollenbacher, A. F., Piper, S. C., Yoshimura, K., & Wahlen, M. (2011). Interannual variability in the oxygen isotopes of atmospheric CO₂ driven by El Niño. *Nature*, *477*(7366), 579.
- Williams, R. G., McDonagh, E., Roussinov, V. M., Torres-Valdes, S., King, B., Sanders, R., & Hansell, D. A. (2011). Nutrient streams in the North Atlantic: Advective pathways of inorganic and dissolved organic nutrients. *Global Biogeochemical Cycles*, *25*, GB4008. <https://doi.org/10.1029/2010GB003853>
- Wuebbles, D. J., Fahey, D. W., & Hibbard, K. A. (2017). *Climate science special report: Fourth National Climate Assessment, volume 1*. Washington, DC, USA: U.S. Global Change Research Program.
- Xie, S., Lin, W., Rasch, P. J., Ma, P. L., Neale, R., & Larson, V. E. (2018). Understanding cloud and convective characteristics in version 1 of the E3SM atmosphere model. *Journal of Advances in Modeling Earth Systems*, *10*, 2618–2644. <https://doi.org/10.1029/2018MS001350>
- Xu-Ri, & Prentice, I. C. (2008). Terrestrial nitrogen cycle simulation with a dynamic global vegetation model. *Global Change Biology*, *14*(8), 1745–1764. <https://doi.org/10.1111/j.1365-2486.2008.01625.x>
- Yang, X., & Post, W. M. (2011). Phosphorus transformations as a function of pedogenesis: A synthesis of soil phosphorus data using Hedley fractionation method. *Biogeosciences*, *8*(10), 2907–2916.
- Yang, X., Post, W. M., Thornton, P. E., & Jain, A. (2013). The distribution of soil phosphorus for global biogeochemical modeling. *Biogeosciences Discussions (Online)*, *9*(4), 2525–2537.
- Yang, X., Thornton, P. E., Ricciuto, D. M., & Hoffman, F. M. (2016). Phosphorus feedbacks may constrain tropical ecosystem responses to changes in atmospheric CO₂ and climate. *Geophysical Research Letters*, *43*, 7205–7214. <https://doi.org/10.1002/2016GL069241>
- Yang, X., Thornton, P. E., Ricciuto, D. M., & Post, W. M. (2014). The role of phosphorus dynamics in tropical forests—A modeling study using CLM-CNP. *Biogeosciences*, *11*(6), 1667–1681. <https://doi.org/10.5194/bg-11-1667-2014>
- Yang, X., Wittig, V., Jain, A. K., & Post, W. (2009). Integration of nitrogen cycle dynamics into the Integrated Science Assessment Model for the study of terrestrial ecosystem responses to global change. *Global Biogeochemical Cycles*, *23*, GB4029. <https://doi.org/10.1029/2009GB003474>
- Zaehle, S., Friend, A., Friedlingstein, P., Dentener, F., Peylin, P., & Schulz, M. (2010). Carbon and nitrogen cycle dynamics in the O-CN land surface model: 2. Role of the nitrogen cycle in the historical terrestrial carbon balance. *Global Biogeochemical Cycles*, *24*, GB1006. <https://doi.org/10.1029/2009GB003522>

- Zaehle, S., Medlyn, B. E., De Kauwe, M. G., Walker, A. P., Dietze, M. C., Hickler, T., & Norby, R. J. (2014). Evaluation of 11 terrestrial carbon-nitrogen cycle models against observations from two temperate Free-Air CO₂ Enrichment studies. *New Phytologist*, *202*(3), 803–822. <https://doi.org/10.1111/nph.12697>
- Zender, C. S., Bian, H., & Newman, D. (2003). Mineral dust entrainment and deposition (DEAD) model: Description and 1990s dust climatology. *Journal of Geophysical Research*, *108*(D14), 4416.
- Zeng, X., & Decker, M. (2009). Improving the numerical solution of soil moisture-based Richards equation for land models with a deep or shallow water table. *Journal of Hydrometeorology*, *10*(1), 308–319.
- Zhang, Y., Goll, D., Bastos, A., Balkanski, Y., Boucher, O., Cescatti, A., & Piao, S. (2019). Increased global land carbon sink due to aerosol-induced cooling. *Global Biogeochemical Cycles*, *33*, 439–457. <https://doi.org/10.1029/2018GB006051>
- Zhang, K., Rasch, P. J., Taylor, M. A., Wan, H., Leung, R., & Ma, P. L. (2018). Impact of numerical choices on water conservation in the E3SM atmosphere model version 1 (EAMv1). *Geoscientific Model Development*, *11*(5), 1971–1988.
- Zhu, Q., Iversen, C. M., Riley, W. J., Slette, I. J., & Vander Stel, H. M. (2016). Root traits explain observed tundra vegetation nitrogen uptake patterns: Implications for trait-based land models. *Journal of Geophysical Research: Biogeosciences*, *121*, 3101–3112. <https://doi.org/10.1002/2016jg003554>
- Zhu, Z., Piao, S., Myneni, R. B., Huang, M., Zeng, Z., & Canadell, J. G. (2016). Greening of the Earth and its drivers. *Nature Climate Change*, *6*(8), 791.
- Zhu, Q., & Riley, W. J. (2015). Improved modelling of soil nitrogen losses. *Nature Climate Change*, *5*(8), 705–706. <https://doi.org/10.1038/nclimate2696>
- Zhu, Q., Riley, W. J., & Tang, J. (2017). A new theory of plant–microbe nutrient competition resolves inconsistencies between observations and model predictions. *Ecological Applications*, *27*(3), 875–886.
- Zhu, Q., Riley, W. J., Tang, J. Y., & Koven, C. D. (2016). Toward an allocation scheme for global terrestrial carbon models. *Biogeosciences*, *13*(1), 341–363. <https://doi.org/10.5194/bg-13-341-2016>
- Zhu, Q., Riley, W. J., Tang, J. Y., Randerson, J. R., Collier, N., Hoffman, F. M., & Bisht, G. (2019). Representing nitrogen, carbon, and phosphorus interactions in the ELMv1-ECA Land Model: Model development and global benchmarking. *Journal of Advances in Modeling Earth Systems*, *11*, 2238–2258. <https://doi.org/10.1029/2018MS001571>
- Zwally, H., Schutz, B., Abdalati, W., Abshire, J., Bentley, C., & Brenner, A. (2002). ICESat's laser measurements of polar ice, atmosphere, ocean, and land. *Journal of Geodynamics*, *34*(3–4), 405–445.